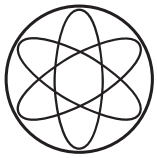

TECHNISCHE UNIVERSITÄT MÜNCHEN
PHYSIK DEPARTMENT
LEHRSTUHL FÜR THEORETISCHE PHYSIK T37

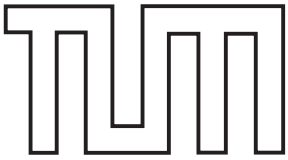

Aqueous Interfaces: Bridging the Gap Between Molecular and Continuum Models

Douwe Jan Bonthuis

Vollständiger Abdruck der von der Fakultät für Physik der Technischen Universität München zur Erlangung des akademischen Grades eines

Doktors der Naturwissenschaften (Dr. *rer. nat.*)

genehmigten Dissertation.

Vorsitzender:		Univ.-Prof. Dr. F. Simmel
Prüfer der Dissertation:	1.	Univ.-Prof. Dr. R. Netz, Freie Universität Berlin
	2.	Univ.-Prof. Dr. W. Zwerger

Die Dissertation wurde am 31.05.2012 bei der Technischen Universität München eingereicht und durch die Fakultät für Physik am 27.06.2012 angenommen.

Contents

Abstract

At aqueous interfaces, the structure of water differs significantly from the structure in bulk fluid. In particular, the water density at the interface exhibits an oscillating profile and the orientation of the water molecules at the interface is strongly anisotropic. The molecular structure of the interfacial water has a decisive effect on the local dielectric function, as well as on the interfacial viscosity. In addition, the non-spherical shape of water molecules affects the fluid dynamics. Despite their importance for the behavior of liquid flowing under strong confinement – as is ubiquitous in biological systems, in colloidal suspensions and in micro- and nanofluidics – these molecular interfacial effects are neglected in standard continuum theories of water dynamics. The work described in this thesis is aimed at incorporating molecular information inferred from molecular dynamics simulations into continuum theory to describe the non-equilibrium dynamics of aqueous solutions at interfaces.

First, we extract the interfacial profile of the full dielectric tensor of pure water from molecular dynamics simulations, and incorporate the results into a mean-field description of the interfacial electrostatics. Comparing the results to literature values, we show that the dielectric profile of pure water is both necessary and sufficient to explain the experimental double-layer capacitance of carbon-based surfaces. Second, we investigate the hydrodynamic properties of the interfacial water layer, and quantify the effect of hydrodynamic slip or enhanced interfacial viscosity on pressure-driven and electrokinetic flow. Third, we formulate a generalized Navier-Stokes equation, including the effect of rotating water dipoles, and calculate the effect of spinning water molecules on electrokinetic flow. We show that whereas a static electric field does not induce flow in a purely dipolar fluid, a rotating electric field can be used to drive an electro-hydraulic pump. Finally, we incorporate the profiles of the dielectric function and the viscosity into a combined mean-field and continuum theory of electrokinetic flow to calculate the electro-osmotic mobility and surface conductivity of charged solutes. Using this framework, we are able to explain both the experimentally observed saturation of electro-osmotic mobility as a function of bare surface charge density and the universally measured excess surface conductivity within a single model.

Zusammenfassung

An wässrigen Grenzflächen unterscheidet sich die Wasserstruktur wesentlich von der Struktur im inneren Volumen des Wassers. Insbesondere weist die Wasserdichte an der Grenzfläche ein oszillierendes Profil auf, und die Orientierung der Wassermoleküle an der Grenzfläche ist stark anisotrop. Diese Molekülstruktur des Wassers hat einen entscheidenden Einfluss auf die lokale dielektrische Funktion, sowie auf die Grenzflächenviskosität. Darüber hinaus beeinflusst die nichtsphärische Form der Wassermoleküle die Flüssigkeitsdynamik. Trotz ihrer großen Bedeutung für das Verhalten der Flüssigkeit unter starken räumlichen Beschränkungen – welche in biologischen Systemen, kolloidalen Suspensionen sowie mikro- und nanofluidischen Anwendungen universell auftreten – werden diese molekularen Grenzflächen-Effekte in Standard-Kontinuums Theorien der Wasserdynamik vernachlässigt. Diese Doktorarbeit zielt auf die Einbeziehung molekularer Informationen, abgeleitet aus Molekulardynamik-Simulationen, in Kontinuumstheorien, um damit die Nichtgleichgewichts-Dynamik von wässrigen Lösungen an Grenzflächen zu beschreiben.

Zuerst extrahieren wir das Grenzflächenprofil des vollständigen dielektrischen Tensors von reinem Wasser aus Molekulardynamik-Simulationen. Diese Ergebnisse werden anschließend in eine molekularfeldtheoretische Beschreibung der Grenzflächen-Elektrostatik aufgenommen. Durch Vergleich mit Literaturwerten zeigen wir, dass das dielektrische Profil von reinem Wasser sowohl notwendig ist, als auch ausreichend, um die experimentelle Oberflächenkapazität von Kohlenstoff-basierten Oberflächen zu erklären. Zweitens untersuchen wir die hydrodynamischen Eigenschaften des Grenzflächenwassers und quantifizieren die Auswirkung des hydrodynamischen Schlupfs bzw. der erhöhten Grenzflächenviskosität auf druckgetriebene und elektrokinetische Strömungen. Drittens formulieren wir eine verallgemeinerte Navier-Stokes Gleichung unter Berücksichtigung rotierender Wasserdipole, und berechnen die Auswirkung dieser molekularen Wasserrotation auf elektrokinetische Strömung. Wir zeigen, dass, obwohl ein statisches elektrisches Feld in einer rein dipolaren Flüssigkeit keine Strömung erzeugt, ein rotierendes elektrisches Feld verwendet werden kann, um eine elektro-hydraulische Pumpe anzutreiben. Schließlich nehmen wir die Profile der dielektrischen Funktion und der Viskosität in einer kombinierten Molekularfeld- und Kontinuumstheorie der elektrokinetischen Strömung auf, und berechnen die elektroosmotische Mobilität und die Oberflächenleitfähigkeit geladener Teilchen. Dieser theoretische Rahmen erlaubt uns, sowohl die experimentell beobachtete Sättigung der elektroosmotischen Mobilität in Abhängigkeit der blanken Oberflächenladungsdichte, als auch die universell gemessene überschüssige Oberflächenleitfähigkeit innerhalb eines einzigen Modells zu erklären.

Chapter 1

Introduction

Water is the primary constituent of biological cells [1], and finds extensive use as a solvent as well as a working fluid in technological applications. In particular the number of applications of micro- and nanofluidic technology has been rising rapidly over the past decades [2]. Inherent to the small size of nanofluidic devices, surface characteristics dominate the bulk flow properties and as device dimensions shrink even further, interfacial effects become ever more important. Moreover, a variety of different strategies actually exploit boundary effects to manipulate fluids, such as acoustic streaming [3] and electrokinetic effects [4]. A limiting case of small-scale fluid flow is found in biological systems, where membrane channels and pumps transport fluids and biological molecules on a single-molecular scale [5, 6]. The ambitious goal of nanofluidics is to reach the single-molecular length scale in man-made devices and to manipulate flows on the scale of biopolymers and single proteins. Apart from microscopic applications, such as micrometer-scale laboratories, arrays of nanofluidic channels can be used in macroscopic pumps, desalination devices and electrokinetic power plants [7–11]. For all applications, ranging from microscopic analysis devices to large-scale power plants, a profound comprehension of the behavior of liquid flowing under strong confinement is required [12]. Likewise, to acquire a better understanding of proteins such as aquaporin and other membrane channels [13, 14], the mechanisms behind single molecular flows need elucidation [15]. Because of the large surface-to-volume ratio, describing the fluidic properties on this scale involves a precise determination of the electrostatic and hydrodynamic characteristics of the aqueous interface.

1.1 The Helmholtz-Smoluchowski Equation

Particles in aqueous solution typically acquire a net charge, which is compensated for by an excess of counterions in the electrolyte. In electrokinetics, this charge separation is used to drive fluid flow along charged surfaces by means of an applied electric field. For the understanding of the dynamics of water, ions and macromolecules in biological cells, which are crowded with highly charged molecules, electrokinetics are of great significance. Equally important, electrokinetics are of interest for technological applications, primarily because they are the preferred method to drive micro- and nanofluidic flows in “lab-on-a-chip” devices. Moreover, electrokinetic experiments provide a sensitive probe of the

electrostatic and hydrodynamic properties of the aqueous interface. The basic model of electrokinetic flow consists of a uniform electric field $\boldsymbol{E}$ applied parallel to a uniformly charged infinite plane in contact with a continuum electrolyte of relative dielectric constant ε and spatially constant viscosity η. At large distances from the interface, the flow velocity $\boldsymbol{u}$ parallel to the charged surface is expressed by the Helmholtz-Smoluchowski equation,

$$\boldsymbol{u} = -\frac{\varepsilon\varepsilon_0\,\zeta}{\eta}\,\boldsymbol{E}, \tag{1.1}$$

named after Hermann Helmholtz [16] and Marian Ritter von Smolan Smoluchowski [17]. In Eq. 1.1, ε_0 is the permittivity of vacuum and ζ is the electrostatic potential at the shear plane. Eq. 1.1 is valid for electrokinetic flow in arbitrary geometry, provided that the typical length scale a of the charged objects exceeds the Debye screening length κ^{-1} of the electrolyte by a large margin, $\kappa a \gg 1$. In the opposite limit, $\kappa a \ll 1$, a factor $^2/_3$ appears on the right-hand-side of Eq. 1.1 [18]. Although the fluid velocity $\boldsymbol{u}$ is measured far away from the interface, its origin lies within the first few nanometers directly adjacent to the surface: the region where the counter-charge accumulates. Within this region, the water density varies appreciably, typically showing a peak close to the interface with subsequent oscillations, reaching bulk value after ~ 1 nm. Moreover, the water orientation is highly anisotropic: water molecules directly at the interface tend to orient with their hydrogen atoms toward the surface, whereas the second layer of water molecules are preferentially oriented in the opposite direction, *etc.*, alternating for several layers. The polar ordering of the water molecules gives rise to a strong electric field in the interfacial region, showing sharp oscillations around zero that decay over a similar length scale as the density fluctuations. Inherent to the varying water structure, the dielectric permittivity ε and the viscosity η are not spatially constant, but depend on the distance to the surface instead. Clearly, these inhomogeneous profiles, and consequently the effects of the interfacial molecular structure, are missing from the continuum expression of Eq. 1.1.

In the following sections, we will discuss the effects of the interfacial molecular structure on the fluid dynamics, focusing on the dielectric permittivity ε, the viscosity η and the effect of molecular rotation.

1.2 Dielectric Permittivity

One of the most salient properties of water is its high molecular polarity. As a result, electrostatic interactions in aqueous environments are drastically modified with profound implications for the behavior of ions, proteins and membranes in solution [19]. Experiments and simulations have shown that the dielectric function of homogeneous water exhibits two singularities for wave vectors at molecular length scales, indicating anomalous screening effects in bulk water [20]. To what extent interfacial water exhibits similar anomalies is less clear [21]. Experimental capacitance studies have led Stern to propose a model for an aqueous interface where the dielectric constant is reduced over a nanoscopic width [22]. Whether this layer reflects ionic or rather intrinsic water properties is not specified in the original Stern model. However, recent terahertz spectroscopy experiments have shown that the dielectric properties of water itself are modified at interfaces within a layer of molecular size [23]. Without considering an explicit interfacial dielectric profile, the relation between the non-local dielectric function and the Stern-layer contribution to the capacitance has been established [24], including non-linear effects [25]. Using approximate

statistical mechanical methods, the decrease of the interfacial capacitance for a dipolar fluid has been related to molecular ordering and orientation [26]. However, a method for extracting dielectric profiles from interfacial water orientational and spatial distributions, as well as detailed knowledge of the profiles themselves have been lacking so far.

A thorough understanding of the interfacial dielectric behavior of water is a prerequisite for correct modeling of ion distributions [27] and double-layer interactions [28], as well as electrokinetic effects. Similarly, the interfacial dielectric function is a key ingredient to solvent-implicit approaches toward protein and macro-molecular modeling [29]. Control over the interfacial dielectric constant is also crucial for a number of industrial applications, including high power and long duration energy storage devices [30]. Finally, dielectric effects are one contribution to the hydration repulsion between polar surfaces [19, 31]. The dielectric properties of interfacial water have been studied using both simulations and analytic approaches. One shortcoming of previous analytic approaches is that the water bulk behavior, including the above-mentioned anomaly, is typically not accounted for [32, 33]. At the same time, previous simulations with explicit water and ions could not be analyzed within the existing theoretical framework. One reason for the complexity is the appearance of higher order multipole moments, which are particularly essential at interfaces [34].

1.3 Viscosity

A growing amount of literature indicates that on small length scales, the hydrodynamic boundary condition deviates from the usual no-slip condition [35, 36]. Experimentally, the viscosity is defined as the proportionality constant between the shear force per unit area and the resulting velocity gradient. Close to a wall, this proportionality constant appears to be different from the bulk value. In the first few molecular layers next to the interface, this is caused by the changing water structure, most notably the dipolar orientation and the oscillating density profile. In addition, at hydrophobic walls there is a density depletion gap between the wall and the fluid [37–39]. Directly at the wall, the velocity gradient can therefore be very different from the bulk velocity gradient in a Couette shearing scenario. On a molecular scale, even "true slip" of the first molecular layer along the wall can be imagined.

On a simple level, the assumption that the surface stress is linearly related to the surface velocity via a friction coefficient, which equates the surface stress to the viscous shear stress, leads to the notion of a slip length [40]. A finite slip length greatly enhances flow rates through small channels. The slip length exhibits a sensitive dependence on the microscopic properties of the surface, increasing as the contact angle grows and the surface becomes more hydrophobic, and scaling proportional to the depletion length to the fourth power [41]. Due to their hydrophobic nature and the large vacuum gap between wall and fluid, carbon nanotubes appear to have very large slip lengths, up to tens of micrometers [42], making them promising candidates for use as channels [43] and pumps [44] in nanofluidic devices.

Alternatively, the effect of the interfacial hydrodynamics can be modeled by a space-dependent viscosity profile $\eta(\boldsymbol{r})$, with $\boldsymbol{r}$ the spatial coordinates. Whether a slip length, a viscosity profile or a combination of the two provides the more accurate model of the hydrodynamic boundary condition depends on surface type and molecular composition.

1.4 Water Rotation

Ever since the first electrophoretic measurements it has been known that nominally uncharged substances in pure water, such as air bubbles and oil droplets, move toward the positive electrode and thus behave as effectively negatively charged [45]. Based on streaming-potential [46], titration [45], and thin-film stability studies [47], this behavior is attributed to the interfacial accumulation of negatively charged ions such as OH^-. For the air-water interface, however, recent second-harmonic generation [48] as well as spectroscopy experiments and simulations [49] suggest that not OH^- but H_3O^+ shows enhanced interfacial adsorption. This discord has stirred fierce discussions [45, 49, 50]. A way out of the dilemma was proposed in recent molecular dynamics (MD) simulations of aqueous interfaces, where pure water without any added ions induced electrophoresis of the same sign and size as observed experimentally for air bubbles or oil droplets [51].

The ability of electric fields to produce hydrodynamic shear at pure-water interfaces opens attractive possibilities in other geometries, such as water-filled carbon nanotubes [52]. For flow through such tiny capillaries, the electrostatic boundary conditions strongly influence the permeability to charged species. The electrostatics of a small channel embedded in a medium of very low dielectric constant leads to a large self-energy barrier for ions to enter the confined region [53, 54]. In many biological channels, transport of ions is facilitated by inclusion of fixed charges in the channel walls [55], coating walls with dipolar surface groups [56, 57] and screening by salt [58]. Fixed charges outside a carbon nanotube are found to affect the pressure-driven passage of water molecules through the nanotube as well [59]. Even more intriguing is the observation that carbon nanotubes filled with pure water exhibit electro-osmotic flow when either an electric field is applied [60] or point charges are fixed outside the channel [61]. Similarly, electro-osmotic flow is found in uncharged channels filled with solutions of the relatively symmetric salts sodium chloride and potassium chloride [62–64].

The mechanism for this water-induced electrophoresis was speculated to be related to the interfacial water structure, involving static properties such as dipolar ordering [65] and density profile [66], as well as dynamic properties such as surface viscosity and slip length [67]. In particular, the appearance of a non-zero ζ-potential in absence of free charges was speculated to be related to the electrostatics in the boundary layer: water molecules tend to orient, leading to a strong dipolar field in the first few molecular layers next to the interface. The coupling of the electric field to this dipole density was thought to induce flow via rotation of individual molecules [51, 60]. Although exciting, these results raise concern as fundamental laws of physics appear to be violated. In particular, the effects seem at odds both with Onsager's reciprocal theorem, since an externally applied pressure drop cannot cause a steady electric current because of the absence of free charges, and with thermodynamics, since the electric field performs no work in the steady state. Despite the great fundamental importance, a theory that combines hydrodynamics and electric-field effects for interfacial water has been missing until now.

1.5 Ion-Surface Interactions

Apart from charging by an external electric source (for conducting surfaces) and charging by ionization of chemical surface groups, surface charge can originate from specific adsorption of ions. The propensity of an ion to adsorb on to a surface depends on its chemical

properties, such as size, charge and polarizability, as well as on the chemical properties of the surface. A third important factor is the molecular structure of the interfacial water. The combined potential due to the aforementioned effects is termed the potential of mean force (PMF), which can be incorporated into the Poisson-Boltzmann equation as a non-electrostatic contribution to the potential. In Ref. [xi], we determine the PMFs of Br^-, I^-, Cl^- and Na^+ at a hydrophobic self-assembled monolayer (SAM) from MD simulations, and calculate the disjoining pressure between two SAMs from the modified Poisson-Boltzmann equation. The results show that specific adsorption of ions contributes significantly to the surface charge density and should be taken into account when fitting experimental data. Splitting the PMF, however, into contributions from the Lennard-Jones potential, the polarizability, the image charge potential and the electrostatics of the ordered water molecules, fails to capture the results from the MD simulations. In this thesis, we qualitatively model the PMF, taking into account the effect of the inhomogeneous dielectric profile and the hydration potential due to the varying density profile. To account for specific ion adsorption in all other calculations, we include heuristic non-electrostatic potentials that are similar to the ones from Ref. [xi] for distances larger than ~ 3 Å.

1.6 Molecular Modeling: Molecular Dynamics Simulations

For direct investigation of interfacial properties, simulation techniques are particularly valuable. For the work described in this thesis, the molecular information is obtained from all-atom classical molecular dynamics (MD) simulations, in which Newton's equations of motion are integrated numerically for a system of non-polarizable molecules [68]. The time-step used is typically $\sim 10^{-15}$ s, allowing total simulation times of the order of nanoseconds to microseconds for systems of $\sim 10^4$ atoms, which are appropriate time and length scales to capture the molecular motion (orientational relaxation time $\sim 10^{-12}$ s [69–71]) and the equilibrium structure of liquid water. In classical MD simulations, the interaction potential between two atoms i and j at distance r_{ij} is modeled by the spherically symmetric potential

$$U_{ij}\left(r_{ij}\right) = U_{ij}^{\mathrm{C}}\left(r_{ij}\right) + U_{ij}^{\mathrm{LJ}}\left(r_{ij}\right), \tag{1.2}$$

with the Coulomb potential being given by

$$U_{ij}^{\mathrm{C}}\left(r_{ij}\right) = \frac{q_i q_j}{4\pi\,\varepsilon\varepsilon_0\, r_{ij}}, \tag{1.3}$$

and the Lennard-Jones potential by

$$U_{ij}^{\mathrm{LJ}}\left(r_{ij}\right) = 4\,\epsilon_{ij}\left[\left(\frac{\sigma_{ij}}{r_{ij}}\right)^{12} - \left(\frac{\sigma_{ij}}{r_{ij}}\right)^{6}\right]. \tag{1.4}$$

The parameters needed for each atom pair ij are the charges q_i and q_j, the Lennard-Jones interaction strength ϵ_{ij} and the interaction radius σ_{ij}. Water molecules are modeled as single Lennard-Jones spheres, having three (SPC/E [72]) or four (TIP4P/2005 [73]) partial point charges at fixed positions within the molecule. These water models satisfactorily reproduce, among other quantities, the water structure factor (measured using X-ray or neutron diffraction and calculated in MD simulations from the radial distribution function), bulk dielectric constant and water density, which warrants sufficient confidence that classical MD simulations can be used to quantify the molecular structure of interfacial water.

1.7 Outline

The work described in this thesis is aimed at the integration of continuum modeling with molecular information provided by MD simulations, in order to describe the static and dynamic properties of water and electrolytes at charged and uncharged surfaces. In Chapter 2, we derive the theoretical framework needed to calculate the dielectric response tensor from molecular dynamics simulations, and determine its components at the interface between a solid surface and pure water using MD simulations. We incorporate the dielectric profile, which includes the effect of molecular interfacial structure, into a mean-field (Poisson-Boltzmann) description of the interfacial electrostatics. Similarly, MD simulations provide detailed insight into the mechanism of surface slip [74], which sets the hydrodynamic boundary conditions used for the Navier-Stokes equations. In Chapter 3, we investigate the effect of interfacial hydrodynamic slip on the energy dissipation in pressure-driven flow and the thermodynamic efficiency of electrokinetic pumping. In Chapter 4, we include the dipolar water ordering at interfaces and the molecular rotation of water molecules into a generalized Navier-Stokes equation and determine the conditions under which the spin field contributes to the fluid flow. Simulations of ions at interfaces renders information on the characteristics and extent of ion adsorption, which is used to complement the Poisson-Boltzmann equation, see Ref. [xi]. Ultimately, this multi-scale modeling scheme allows us to formulate a modified Helmholtz-Smoluchowski equation (Eq. 1.1), including the effects of molecular structure. In Chapter 5, we combine the effects of the viscosity profile, the dielectric profile and the non-electrostatic ion-surface interactions to calculate electrokinetic mobility, as well as the electric surface conductivity at charged surfaces.

Chapter 2

Profile of the Static Permittivity Tensor of Water at Interfaces

In this chapter, we derive the theoretical framework to calculate the dielectric response tensor and determine its components for water adjacent to hydrophilic and hydrophobic surfaces using molecular dynamics simulations. For the non-polarizable water model used, linear response theory is found to be applicable up to an external perpendicular field strength of ~ 2 V/nm, which is well beyond the experimental dielectric breakdown threshold. The dipole contribution dominates the dielectric response parallel to the interface, whereas for the perpendicular component it is essential to keep the quadrupole and octupole terms. Including the space-dependent dielectric function in a mean-field description of the ion distribution at a single charged interface, we reproduce experimental values of the interfacial capacitance. At the same time, the dielectric function decreases the electrostatic part of the disjoining pressure between two charged surfaces, unlike previously thought. The difference in interfacial polarizability between hydrophilic and hydrophobic surfaces can be quantized in terms of the dielectric dividing surface. Using the dielectric dividing surface and the Gibbs dividing surface positions to estimate the free energy of a single ion close to an interface, ion-specific adsorption effects are found to be more pronounced at hydrophobic surfaces than at hydrophilic ones, in agreement with experimental trends. The work described in this chapter has been published in Refs. [iii] and [vi].

2.1 Introduction

Electrostatic interactions between charged objects in aqueous solution, such as lipid membranes, proteins and ions, are profoundly influenced by the surrounding water [19]. Each charge embedded in the dielectric environment of the water couples to the local electric field, which comprises both the displacement field emanating from the charged objects and the polarization field stemming from the dielectric medium. In a macroscopic approach, the effect of the water on electrostatic interactions is quantified by means of the static dielectric tensor ε, which is spatially constant and diagonal in bulk. Close to an interface, however, the effect of the water is more intricate. The water density near an interface strongly deviates from its bulk value and the proximity of a surface restricts the molecular

dynamics [75]. Short-ranged interactions between macroscopic objects in water that go beyond homogeneous continuum electrostatics, such as hydration forces and hydrophobic effects, are often attributed to this local variation of the solvent structure [31, 76]. Because of the extremely polar nature of water molecules, the water structure directly affects the electrostatic environment, making the dielectric tensor inherently space-dependent. The effect of the solvent structure strongly depends on the nature of the interface: hydrophobic and hydrophilic surfaces have a vastly different influence on the adjacent water [77, 78].

Within the framework of linear response theory, the space-dependent dielectric response function can be expressed as a non-local tensor, depending on the positions of the source and the response [24, 25, 79]. In Fourier space, the non-local dielectric tensor of bulk water exhibits two singularities for wave vectors on molecular length scales [20]. Whether similar anomalies appear in the space-dependent static dielectric function of interfacial water has long remained unclear.

The capacitance formed by a charged interface and its counterions serves as a sensitive probe of dielectric interface effects. It has been known for almost a century that the Gouy-Chapman model overestimates the experimental data of interfacial capacitance, which has been ascribed to variations of the dielectric constant at the interface [80, 81]. In the Stern model of the electric double layer, the variation of the dielectric tensor is accounted for by the combination of a length scale and an effective interfacial dielectric constant, reproducing the experimental capacitance [22]. In the limit of low salt concentration, it has been shown how the Stern layer contribution to the capacitance emerges from the introduction of a non-local dielectric function, independent of the exact form of the dielectric profile [24]. Also the relation between the dielectric profile and the length scale appearing in the Stern model has been established [25]. However, an explicit calculation of the interfacial dielectric profile of water has been lacking up to now.

The question of whether the decrease in the dielectric profile reflects ionic or intrinsic water properties is still subject to debate. The decrease in the dielectric constant has been attributed to the high ionic concentration close to charged interfaces [82], or to dielectric saturation due to the corresponding high electric field strength [83]. However, recent terahertz spectroscopy experiments on carbohydrates [84] and lipid membranes [23] have shown that the dielectric response of water itself is modified within an interfacial layer of molecular size. Theoretical attempts to relate the dielectric response to molecular dynamics have been based on analytical as well as simulation studies. Analytical approaches include approximate statistical mechanical methods, which have been used to show that the reduced dielectric constant at the interface is associated with molecular ordering and orientation [26]. In another analytical approach, water polarization has been included explicitly in a mean-field description [32, 33], where molecular effects such as the above-mentioned singularities are not accounted for. Simulations with explicit water and ions did not allow for straightforward interpretation previously, partly because of the appearance of higher-order multipole moments. In fact, the preferred orientation of water molecules near an interface is set by the fundamental asymmetry stemming from the quadrupole and higher-order even multipole moments [34, 85, 86]. This asymmetrical water structure plays a decisive role in the dielectric response of water at an interface, which is ignored in many studies [87]. Recently, we have shown that the electric quadrupole and octupole moments are essential components of the interfacial dielectric function [88].

The dielectric function in thin interfacial layers strongly affects the forces between macromolecules and surfaces as a result of the long range of the electrostatic force. Fur-

thermore, a knowledge of the space-dependent dielectric tensor is indispensable to the interpretation of the ionic surface propensity [89] and solvation free energy [27, 90, 91], as well as the electrophoretic mobility of solutes and the double-layer capacitance [80, 81]. In addition, the dielectric tensor is a vital ingredient for coarse-grained calculations, where the water is taken into account implicitly. Finally, the electrostatics close to a solid interface are crucial from a technological point of view, in particular for the design of novel energy storage media based on the double-layer capacitance.

In this chapter, we thoroughly investigate the consequences of the interfacial dielectric profile for the interfacial capacitance, the hydration interaction between charged plates in water and the ion adsorption energy at hydrophilic and hydrophobic surfaces. First, we present a complete derivation of the expressions used to calculate the components of the dielectric response tensor at planar interfaces from molecular dynamics simulations. Second, we calculate the dielectric tensor of pure water adjacent to both hydrophilic (hydroxyl-terminated) and hydrophobic (hydrogen-terminated) diamond surfaces. We show that the salient differences between the two surface types can be quantified in terms of a single length scale, set by the position of the dielectric dividing surface. Third, we investigate the effect of the higher-order electric moments on the electric potential profile across the interface. Fourth, we incorporate the space dependence of the dielectric tensor in a Poisson-Boltzmann description of a salt solution at a charged interface. Comparing with experimental values, we show that including the dielectric response of pure water suffices to capture the dependence of the double-layer capacitance on the salt concentration. Fifth, we calculate the disjoining pressure between two charged surfaces using the same Poisson-Boltzmann description. On the Poisson-Boltzmann level, the dielectric profile appears to be insufficient to describe the strong, short-ranged repulsive forces commonly measured between both charged and uncharged surfaces in water [92]. Finally, we estimate the free energy of a single ion near a dielectric boundary, and show that the different dielectric characteristics of hydrophilic and hydrophobic surfaces have a pronounced effect on ion adsorption. All equations are given in SI units.

2.2 Theoretical Framework

2.2.1 Linear Response

Most general, the dielectric response function depends on the position $\boldsymbol{r}$ of the displacement field $\boldsymbol{D}(\boldsymbol{r})$, the position $\boldsymbol{r}'$ of the local electric field $\boldsymbol{E}(\boldsymbol{r}')$ and on the field magnitude. In the linear response regime, a change in displacement field is linearly related to a change in electric field,

$$\Delta\boldsymbol{D}(\boldsymbol{r}) = \varepsilon_0 \int \varepsilon_{nl}(\boldsymbol{r},\boldsymbol{r}') \cdot \Delta\boldsymbol{E}(\boldsymbol{r}') \, \mathrm{d}\boldsymbol{r}', \tag{2.1}$$

with ε_0 the permittivity of vacuum and $\varepsilon_{nl}(\boldsymbol{r},\boldsymbol{r}')$ the non-local dielectric tensor. If the electric field is constant in space, $\Delta\boldsymbol{E}(\boldsymbol{r}) = \Delta\boldsymbol{E}$, the response function is automatically local,

$$\Delta\boldsymbol{D}(\boldsymbol{r}) = \varepsilon_0 \varepsilon(\boldsymbol{r}) \cdot \Delta\boldsymbol{E} \quad \text{with} \quad \varepsilon(\boldsymbol{r}) = \int \varepsilon_{nl}(\boldsymbol{r},\boldsymbol{r}') \, \mathrm{d}\boldsymbol{r}', \tag{2.2}$$

making the usual locality assumption $\varepsilon_{nl}(\boldsymbol{r},\boldsymbol{r}') = \varepsilon(\boldsymbol{r})\,\delta(\boldsymbol{r}-\boldsymbol{r}')$ superfluous. Alternatively, the inverse dielectric response function is defined by [24]

$$\Delta\boldsymbol{E}(\boldsymbol{r}) = \varepsilon_0^{-1} \int \varepsilon_{nl}^{-1}(\boldsymbol{r},\boldsymbol{r}') \cdot \Delta\boldsymbol{D}(\boldsymbol{r}') \, \mathrm{d}\boldsymbol{r}', \tag{2.3}$$

with $\varepsilon_{nl}^{-1}(\boldsymbol{r},\boldsymbol{r}')$ the functional inverse of $\varepsilon_{nl}(\boldsymbol{r},\boldsymbol{r}')$, defined by $\int \varepsilon_{nl}(\boldsymbol{r},\boldsymbol{r}')\,\varepsilon_{nl}^{-1}(\boldsymbol{r}',\boldsymbol{r}'')\,\mathrm{d}\boldsymbol{r}' = \delta(\boldsymbol{r}-\boldsymbol{r}'')$. The inverse dielectric response function is automatically local when the displacement field is constant in space, yielding

$$\Delta\boldsymbol{E}(\boldsymbol{r}) = \varepsilon_0^{-1}\varepsilon^{-1}(\boldsymbol{r})\cdot\Delta\boldsymbol{D}, \tag{2.4}$$

with $\varepsilon^{-1}(\boldsymbol{r})$ the inverse dielectric function. Note that the relation $\varepsilon(\boldsymbol{r})\,\varepsilon^{-1}(\boldsymbol{r}) = 1$ does not hold without additional assumptions.

2.2.2 Multipole Expansion

In a classical approximation, the polar molecules are regarded as being composed of atoms, located at positions $\boldsymbol{r}_j^i$, carrying point charges q_j^i. The total charge density $\rho(\boldsymbol{r})$ is given by averaging over the partial charges q_j^i of all atoms $j\,(i)$ and all molecules i,

$$\rho(\boldsymbol{r}) = \sum_i \sum_{j(i)} q_j^i\,\delta\left(\boldsymbol{r}-\boldsymbol{r}_j^i\right). \tag{2.5}$$

We will now expand the electric field in terms of molecular multipole moments, starting from the integral equation for the electric field [93],

$$\varepsilon_0\boldsymbol{E}(\boldsymbol{r}) = \frac{1}{4\pi}\int \rho\left(\boldsymbol{r}'\right)\frac{\boldsymbol{r}-\boldsymbol{r}'}{|\boldsymbol{r}-\boldsymbol{r}'|^3}\,\mathrm{d}\boldsymbol{r}'. \tag{2.6}$$

After inserting Eq. 2.5, the integration variable is shifted from $\boldsymbol{r}'$ to $\boldsymbol{r}'+\boldsymbol{r}_j^i-\boldsymbol{r}_i$, leading to

$$\varepsilon_0\boldsymbol{E}(\boldsymbol{r}) = \frac{1}{4\pi}\int \sum_i\sum_{j(i)} q_j^i\delta\left(\boldsymbol{r}'-\boldsymbol{r}_i\right)\frac{(\boldsymbol{r}-\boldsymbol{r}')-(\boldsymbol{r}_j^i-\boldsymbol{r}_i)}{|\,(\boldsymbol{r}-\boldsymbol{r}')-(\boldsymbol{r}_j^i-\boldsymbol{r}_i)|^3}\,\mathrm{d}\boldsymbol{r}', \tag{2.7}$$

where $\boldsymbol{r}_i$ is some arbitrary reference position in the molecule. The fraction in Eq. 2.7 is then expanded for the case where the intramolecular distance $\boldsymbol{r}_j^i-\boldsymbol{r}_i$ is much smaller than the distance between charge and field points $\boldsymbol{r}-\boldsymbol{r}'$,

$$\begin{aligned}\varepsilon_0\boldsymbol{E}(\boldsymbol{r}) = \frac{1}{4\pi}\int \sum_i\sum_{j(i)} q_j^i\delta\left(\boldsymbol{r}'-\boldsymbol{r}_i\right)\\ \times\left[\frac{\boldsymbol{r}-\boldsymbol{r}'}{|\boldsymbol{r}-\boldsymbol{r}'|^3}+\left(\boldsymbol{r}_j^i-\boldsymbol{r}_i\right)\cdot\nabla'\frac{\boldsymbol{r}-\boldsymbol{r}'}{|\boldsymbol{r}-\boldsymbol{r}'|^3}\right.\\ \left.+\frac{1}{2}\left(\boldsymbol{r}_j^i-\boldsymbol{r}_i\right)\left(\boldsymbol{r}_j^i-\boldsymbol{r}_i\right):\nabla'\nabla'\frac{\boldsymbol{r}-\boldsymbol{r}'}{|\boldsymbol{r}-\boldsymbol{r}'|^3}+\ldots\right]\mathrm{d}\boldsymbol{r}',\end{aligned} \tag{2.8}$$

where the minus sign of $-(\boldsymbol{r}_j^i-\boldsymbol{r}_i)$ cancels the minus sign of $\nabla'(\boldsymbol{r}-\boldsymbol{r}') = -\nabla(\boldsymbol{r}-\boldsymbol{r}')$. Next, all gradient terms are integrated by parts,

$$\begin{aligned}\varepsilon_0\boldsymbol{E}(\boldsymbol{r}) = \frac{1}{4\pi}\int \frac{\boldsymbol{r}-\boldsymbol{r}'}{|\boldsymbol{r}-\boldsymbol{r}'|^3}\Bigg[\sum_i\sum_{j(i)} q_j^i\delta\left(\boldsymbol{r}'-\boldsymbol{r}_i\right)\\ -\nabla'\cdot\sum_i\sum_{j(i)} q_j^i\delta\left(\boldsymbol{r}'-\boldsymbol{r}_i\right)\left(\boldsymbol{r}_j^i-\boldsymbol{r}_i\right)\\ +\frac{1}{2}\nabla'\nabla':\sum_i\sum_{j(i)} q_j^i\delta\left(\boldsymbol{r}'-\boldsymbol{r}_i\right)\left(\boldsymbol{r}_j^i-\boldsymbol{r}_i\right)\left(\boldsymbol{r}_j^i-\boldsymbol{r}_i\right)-\ldots\Bigg]\mathrm{d}\boldsymbol{r}'.\end{aligned} \tag{2.9}$$

The separate components appearing in Eq. 2.9 can be expressed in terms of the molecular multipole moments of order $l \in \{0, 1, 2, \dots\}$, which are defined as

$$\mathsf{p}_{li} = \frac{1}{l!} \sum_{j(i)} q_j^i \left(\boldsymbol{r}_j^i - \boldsymbol{r}_i \right)^l , \tag{2.10}$$

with j running over all partial charges q_j^i of molecule i. The power inside the summation is understood as a serial direct vector multiplication, making p_{li} a tensor of rank l. The density of each multipole moment is defined as

$$\mathsf{P}_l \left(\boldsymbol{r} \right) = \sum_i \mathsf{p}_{li} \, \delta \left(\boldsymbol{r} - \boldsymbol{r}_i \right) , \tag{2.11}$$

where the summation is carried out over all molecules [94]. Using Eqs. 2.10 and 2.11, Eq. 2.9 becomes

$$\varepsilon_0 \boldsymbol{E} \left(\boldsymbol{r} \right) = \frac{1}{4\pi} \int \frac{\boldsymbol{r} - \boldsymbol{r}'}{|\boldsymbol{r} - \boldsymbol{r}'|^3} \Big[P_0 \left(\boldsymbol{r}' \right) - \nabla' \cdot \boldsymbol{P}_1 \left(\boldsymbol{r}' \right) + \nabla' \nabla' : \mathsf{P}_2 \left(\boldsymbol{r}' \right) - \dots \Big] \mathrm{d}\boldsymbol{r}' . \tag{2.12}$$

We use the identity

$$\nabla \cdot \frac{\boldsymbol{r} - \boldsymbol{r}'}{|\boldsymbol{r} - \boldsymbol{r}'|^3} = 4\pi \delta \left(\boldsymbol{r} - \boldsymbol{r}' \right) \tag{2.13}$$

to perform the integrals in Eq. 2.12, except for the P_0 term, to which we will come back later. The divergence of Eq. 2.12 equals

$$\begin{aligned} \nabla \cdot \varepsilon_0 \boldsymbol{E} \left(\boldsymbol{r} \right) = \nabla \cdot \frac{1}{4\pi} \int P_0 \left(\boldsymbol{r}' \right) \frac{\boldsymbol{r} - \boldsymbol{r}'}{|\boldsymbol{r} - \boldsymbol{r}'|^3} \, \mathrm{d}\boldsymbol{r}' \\ + \Big[- \nabla \cdot \boldsymbol{P}_1 \left(\boldsymbol{r} \right) + \nabla \nabla : \mathsf{P}_2 \left(\boldsymbol{r} \right) - \dots \Big] , \end{aligned} \tag{2.14}$$

from which the electric field $\boldsymbol{E} \left(\boldsymbol{r} \right)$ follows as

$$\varepsilon_0 \boldsymbol{E} \left(\boldsymbol{r} \right) = \boldsymbol{D} \left(\boldsymbol{r} \right) - \boldsymbol{m} \left(\boldsymbol{r} \right) . \tag{2.15}$$

The first term in the expansion on the right-hand side of Eq. 2.15 is the monopole term,

$$\boldsymbol{D} \left(\boldsymbol{r} \right) = \frac{1}{4\pi} \int P_0 \left(\boldsymbol{r}' \right) \frac{\boldsymbol{r} - \boldsymbol{r}'}{|\boldsymbol{r} - \boldsymbol{r}'|^3} \, \mathrm{d}\boldsymbol{r}' , \tag{2.16}$$

corresponding to the field from the free charges. The second term is the total polarization density $\boldsymbol{m} \left(\boldsymbol{r} \right)$,

$$\boldsymbol{m} \left(\boldsymbol{r} \right) = \boldsymbol{P}_1 \left(\boldsymbol{r} \right) - \nabla \cdot \mathsf{P}_2 \left(\boldsymbol{r} \right) + \nabla \nabla : \mathsf{P}_3 \left(\boldsymbol{r} \right) - \dots , \tag{2.17}$$

which comprises contributions from the dipole moment per unit volume $\boldsymbol{P}_1$, quadrupole moment P_2, octupole moment P_3 and all higher-order moments. When calculating the polarization in basic electrostatics, all multipole terms of order higher than the dipole are often neglected [93], which is exact for a Stockmayer fluid, for example, where each molecule carries an ideal dipole. For water however, the higher-order terms are of major importance. Note that we could also calculate the multipole moments from all individual atoms instead of averaging an expansion in molecular multipole moments. Although both descriptions of the electrostatics are equivalent, clustering the atoms first to calculate molecular multipole moments has the advantage of a vanishing monopole moment in the case of neutral molecules.

2.2.3 Fluctuation-Dissipation Theorem

To estimate the dielectric function from the polarization fluctuations, we write a statistical mechanical expression for the ensemble-average excess polarization. The total interaction energy of a water-filled volume $\mathcal{V}$ in absence of an external electric field is denoted $U(X)$, with X all relevant coordinates. The energy change ΔU upon application of an external electric field is given by the coupling of the polarization to the field $\boldsymbol{F}$ inside the dielectric,

$$\Delta U = \int_{\mathcal{V}} \psi(\boldsymbol{r})\, \rho(\boldsymbol{r})\, \mathrm{d}\boldsymbol{r}, \tag{2.18}$$

with ψ the excess potential caused by the field, $\nabla\psi(\boldsymbol{r}) = -\boldsymbol{F}$, and $\rho(\boldsymbol{r}) = \varepsilon_0 \nabla \cdot \boldsymbol{E}(\boldsymbol{r})$ the total charge density. The field $\boldsymbol{F}$ to which the fluid responds is constant in space. Therefore, $\boldsymbol{F}$ is associated with either $\boldsymbol{E}$ or $\boldsymbol{D}/\varepsilon_0$ depending on the boundary conditions. After one partial integration, the excess energy is given by

$$\Delta U = -\int_{\mathcal{V}} \nabla\psi(\boldsymbol{r}) \cdot \varepsilon_0 \boldsymbol{E}(\boldsymbol{r})\, \mathrm{d}\boldsymbol{r} = -\int_{\mathcal{V}} \boldsymbol{F} \cdot \boldsymbol{m}(\boldsymbol{r})\, \mathrm{d}\boldsymbol{r}, \tag{2.19}$$

where we used that $\varepsilon_0 \boldsymbol{E}(\boldsymbol{r}) = -\boldsymbol{m}(\boldsymbol{r})$ in absence of free charges. Defining the total polarization by

$$\boldsymbol{M} = \int_{\mathcal{V}} \boldsymbol{m}(\boldsymbol{r})\, \mathrm{d}\boldsymbol{r}, \tag{2.20}$$

the excess polarization density upon application of the external field $\boldsymbol{F}$ is given by [95–97]

$$\begin{aligned} \Delta\boldsymbol{m} &= \langle \boldsymbol{m} \rangle_{\boldsymbol{F}} - \langle \boldsymbol{m} \rangle_0 \\ &= \frac{\int (\boldsymbol{m} - \langle \boldsymbol{m} \rangle_0) \exp\left[-\beta\left(U - \boldsymbol{M}\cdot\boldsymbol{F}\right)\right] \mathrm{d}X}{\int \exp\left[-\beta\left(U - \boldsymbol{M}\cdot\boldsymbol{F}\right)\right] \mathrm{d}X}, \end{aligned} \tag{2.21}$$

where $\langle \ldots \rangle_{\boldsymbol{F}}$ and $\langle \ldots \rangle_0$ denote the ensemble average with and without applied electric field respectively. For molecules without atomic polarizability, the phase space over which the integration in Eq. 2.21 is performed consists of the positions $\boldsymbol{r}_i$ and orientations Ω_i of the permanent multipole moments, $\mathrm{d}X = \prod_i \mathrm{d}\boldsymbol{r}_i \mathrm{d}\Omega_i$, with i the molecular index. For small field $\boldsymbol{F}$, Eq. 2.21 can be linearized to yield

$$\Delta\boldsymbol{m} \approx \frac{\int (\boldsymbol{m} - \langle \boldsymbol{m} \rangle_0)\left(1 + \beta \boldsymbol{M}\cdot\boldsymbol{F}\right) \exp\left[-\beta U\right] \mathrm{d}X}{\int \exp\left[-\beta U\right] \mathrm{d}X}. \tag{2.22}$$

Using short-hand notation for the ensemble averages, we obtain the excess polarization vector as

$$\Delta\boldsymbol{m}(\boldsymbol{r}) \approx \beta\left[\langle \boldsymbol{m}(\boldsymbol{r})\, \boldsymbol{M} \rangle_0 - \langle \boldsymbol{m}(\boldsymbol{r}) \rangle_0 \langle \boldsymbol{M} \rangle_0\right] \cdot \boldsymbol{F}. \tag{2.23}$$

The term in brackets in Eq. 2.23 includes all nine components of the fluctuation tensor.

Boundary conditions. In a planar system with translational invariance in the x and y directions and a dielectric discontinuity in z direction, the dielectric tensor is diagonal with only two unique components: one parallel and one perpendicular to the surface. Additionally, the electric field and the polarization density only depend on the z direction. Maxwell's equation $\nabla \times \boldsymbol{E}(z) = 0$ implies

$$\nabla_z E_x(z) = \nabla_z E_y(z) = 0, \tag{2.24}$$

so that $E_\parallel$, corresponding to E_x or E_y, is independent of z everywhere. Using Eq. 2.2, Eq. 2.15 and the symmetry condition $\Delta E_\parallel = E_\parallel$ gives

$$\varepsilon_\parallel(z) = 1 + \frac{\Delta m_\parallel(z)}{\varepsilon_0 E_\parallel}. \tag{2.25}$$

The constant field $F_\parallel$ in Eq. 2.23 must correspond to the constant field $E_\parallel$. Therefore, combining Eqs. 2.23 and 2.25 leads to

$$\varepsilon_\parallel(z) \approx 1 + \varepsilon_0^{-1}\beta\left[\langle m_\parallel(z) M_\parallel\rangle_0 - \langle m_\parallel(z)\rangle_0\langle M_\parallel\rangle_0\right]. \tag{2.26}$$

Now we turn to the perpendicular component $\varepsilon_\perp(z)$. Maxwell's equation for the displacement field, $\nabla\cdot\boldsymbol{D}(z) = P_0(z)$, shows that the displacement field is constant in space when $P_0(z) = 0$. Using the boundary condition $\Delta D_\perp(z) = D_\perp$, the inverse dielectric function given in Eq. 2.4 becomes

$$\varepsilon_\perp^{-1}(z) = 1 - \frac{\Delta m_\perp(z)}{D_\perp}. \tag{2.27}$$

In the perpendicular case, the spatially constant field $F_\perp$ must be associated with the constant displacement field $D_\perp/\varepsilon_0$. Consequently, combining Eqs. 2.15, 2.23 and 2.27, we arrive at the fluctuation equation for the inverse perpendicular permittivity,

$$\varepsilon_\perp^{-1}(z) \approx 1 - \varepsilon_0^{-1}\beta\left[\langle m_\perp(z) M_\perp\rangle_0 - \langle m_\perp(z)\rangle_0\langle M_\perp\rangle_0\right]. \tag{2.28}$$

Applying an external electric field, the dielectric tensor can be determined directly using Eqs. 2.25 and 2.27. Eqs. 2.26 and 2.28 can be used when looking at the fluctuations in absence of an external electric field instead.

2.2.4 Calculation of the Polarization Density

The perpendicular electric field is calculated from an integral over all charges,

$$E_\perp(z) = E_\perp(0) + \int_0^z \frac{\rho(z')}{\varepsilon_0}\,\mathrm{d}z'. \tag{2.29}$$

In Eq. 2.29, $E_\perp(0)$ is the external electric field. Using $\boldsymbol{m}(0) = 0$ and Eq. 2.15 with the fact that $D_\perp$ is constant, we find the equation for the perpendicular polarization density

$$m_\perp(z) = -\int_0^z \rho(z')\,\mathrm{d}z'. \tag{2.30}$$

To derive an expression for the parallel polarization, we virtually cut out a volume from the simulation box. In the following text, we adopt two different but equivalent viewpoints. First, we consider all partial charges on the atoms of each molecule explicitly. By cutting the volume, some water molecules are split, forming a non-zero monopole density $P_0(\boldsymbol{r})$ on either side of the virtual cut. In the second viewpoint, idealized multipole moments are located at a single point within each molecule, and the multipole moments are not affected by cutting.

According to the first viewpoint, the net charge inside the volume that has been carved out comprises only $P_0(\boldsymbol{r})$, stemming from the water molecules that have been split by cutting the volume, because the intact water molecules carry no net charge. Because the

split water molecules are all located near the surface of the volume, the integrated charge takes the form of a surface charge,

$$\int_{\mathcal{V}} \rho\left(\boldsymbol{r}\right)\,\mathrm{d}\boldsymbol{r} = \oint_{\partial\mathcal{V}} \sigma\left(\boldsymbol{r}\right)\,\mathrm{d}\boldsymbol{r}, \tag{2.31}$$

with $\sigma\left(\boldsymbol{r}\right)$ the surface charge density arising from $P_0\left(\boldsymbol{r}\right)$.

Adopting the second viewpoint, the total charge inside the volume is calculated from the polarization,

$$\int_{\mathcal{V}} \rho\left(\boldsymbol{r}\right)\,\mathrm{d}\boldsymbol{r} = -\int_{\mathcal{V}} \nabla\cdot\boldsymbol{m}\left(\boldsymbol{r}\right)\,\mathrm{d}\boldsymbol{r}, \tag{2.32}$$

which can be transformed into a surface integral,

$$\int_{\mathcal{V}} \rho\left(\boldsymbol{r}\right)\,\mathrm{d}\boldsymbol{r} = -\oint_{\partial\mathcal{V}} \boldsymbol{m}\left(\boldsymbol{r}\right)\cdot\hat{\boldsymbol{n}}\,\mathrm{d}\boldsymbol{r}. \tag{2.33}$$

Realizing that Eqs. 2.31 and 2.33 hold for any volume $\mathcal{V}$, we find $\sigma\left(\boldsymbol{r}\right) = -\boldsymbol{m}\left(\boldsymbol{r}\right)\cdot\hat{\boldsymbol{n}}$. To calculate the polarization in x direction, we introduce a virtual cut perpendicular to the x axis. We only cut the water molecules at the position of the virtual cut, closing the volume without cutting any other molecules. The surface charge density resulting from the split water molecules equals

$$\sigma\left(z\right) = \int P_0\left(x,z\right)\,\mathrm{d}x, \tag{2.34}$$

where the x dependence of $P_0\left(x,z\right)$ has the form of a Dirac delta function at the position of the cut. Along the surface of the cut, $\boldsymbol{m}\left(z\right)\cdot\hat{\boldsymbol{n}} = \pm m_{\parallel}\left(z\right)$, and thus

$$m_{\parallel}\left(z\right) = \mp\int P_0\left(x,z\right)\,\mathrm{d}x, \tag{2.35}$$

where the different signs apply to closing the volume and integrating $P_0\left(x,z\right)$ on the different sides of the cut. To calculate $m_{\parallel}\left(z\right)$, Eq. 2.35 is averaged over many different cut positions along the x axis.

The polarization density components from Eqs. 2.30 and 2.35 are used to calculate the components of the dielectric response tensor directly. Alternatively, the polarization density is estimated from the expansion of Eq. 2.17, where the multipole densities are calculated explicitly according to Eqs. 2.10 and 2.11. For this alternative method, we calculate the contributions up to the octupole term. Higher order terms cannot be calculated from the simulations with sufficient accuracy. The molecular multipole moments of Eq. 2.10 are calculated with respect to the position of the oxygen atom.

2.3 Simulations & Results

2.3.1 Simulation Setup

We perform molecular dynamics simulations of pure SPC/E water in contact with a diamond slab consisting of a double FCC lattice of carbon atoms using the GROMACS molecular dynamics simulation package [98]. The primary cell contains 928 water molecules and we employ periodic boundary conditions in all directions. The carbon-water interaction is

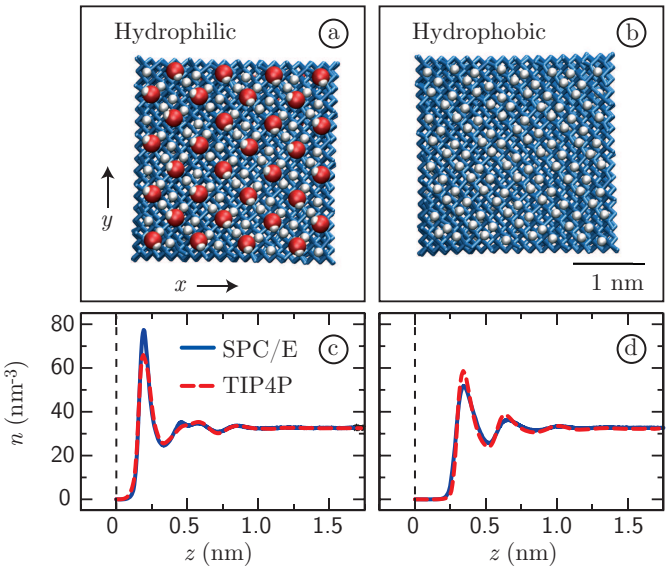

Figure 2.1: *Top view of the two diamond surfaces:* (a) *hydrophilic (hydroxyl-terminated) and* (b) *hydrophobic (hydrogen-terminated). The oxygen atoms are shown in red, the hydrogen in white and the carbon in blue.* (c – d) *Corresponding molecular density profiles* $n(z)$ *of two different water models:* SPC/E *(blue solid lines) and* TIP4P/2005 *(red dashed lines), in absence of an external field.*

determined by the Lennard-Jones parameters $\sigma_{\mathrm{CW}} = 0.3367$ nm and $\epsilon_{\mathrm{CW}} = 0.4247$ kJ/mol (GROMOS 96). We study two surface types: one terminated with hydroxyl groups, giving a hydrophilic surface, and one terminated with hydrogen atoms, giving a hydrophobic surface. On the hydrophilic surface, one in four terminal atoms of the diamond has a hydroxyl group attached, corresponding to a surface coverage of $x_{\mathrm{OH}} = 1/4$ in the notation of Ref. [74]. The hydroxyl groups are free to rotate. The hydrogen atoms terminating the hydrophobic diamond have neither Lennard-Jones coefficients nor charge. The hydrogen atoms of the hydroxyl-terminated carbon atoms on the hydrophilic surface carry a partial charge of 0.408 e, the oxygen atoms carry -0.674 e and the connecting carbon atoms carry 0.266 e. The Lennard-Jones parameters of the oxide-water interaction are $\sigma_{\mathrm{OW}} = 0.3017$ nm and $\epsilon_{\mathrm{OW}} = 0.8070$ kJ/mol, and the hydrogen atoms have no Lennard-Jones interaction. Images of the two surface types are shown in Fig. 2.1 (a – b). For the hydrophilic surface, the position $z = 0$ is defined as the position of the oxygen atoms of the hydroxyl groups, whereas for the hydrophobic surfaces it corresponds to the position of the outermost carbon atoms. We simulate both surface types at vanishing external electric field for a total time of 80 ns, and at field strengths of $E_{\parallel} = 0.05$ V/nm in parallel direction and $D_{\perp}/\varepsilon_0 = 0.5$, 1.0, 2.0, 4.0 and 8.0 V/nm in perpendicular direction for a total time of $35-60$ ns. Simulations at the hydrophilic interface of up to 1.0 V/nm and at the hydrophobic interface at 0.5 V/nm are run at constant pressure, using a semi-isotropic Berendsen barostat. Simulations at higher field strength are run at constant volume. The Lennard-Jones interaction is truncated at 1.0 nm using a shifted cutoff scheme. The Coulomb force is treated using a real-space cutoff at 1.2 nm and pseudo-two-dimensional particle mesh Ewald summation for the long-ranged interaction. To extract the excess fields $\Delta\boldsymbol{E}(z)$ and $\Delta\boldsymbol{D}(z)$, the corresponding fields at vanishing external field are subtracted. SPC/E is a non-polarizable water model; therefore electronic polarization is not

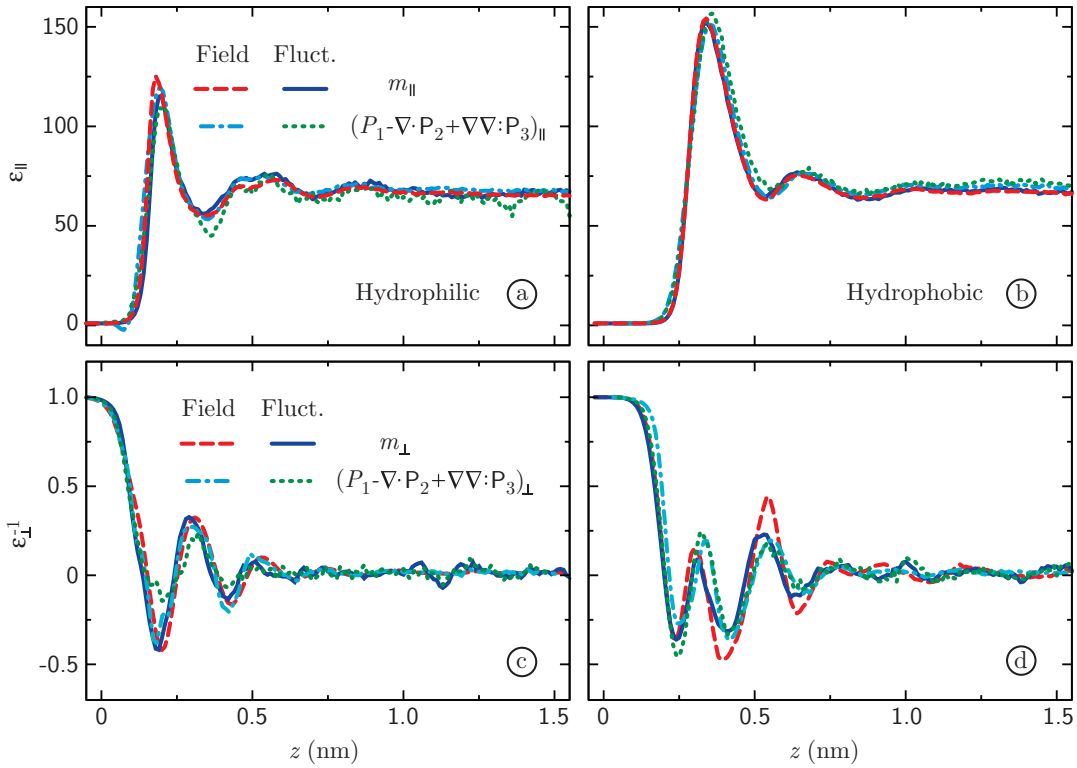

Figure 2.2: *Top: Parallel dielectric function $\varepsilon_\parallel(z)$ next to* (a) *the hydrophilic and* (b) *the hydrophobic diamond, calculated from the total polarization $m_\parallel(z)$ (Eq. 2.35) and from an explicit expansion of the polarization up to the octupole term (Eq. 2.17). The response is calculated in two different ways: from the excess polarization $\Delta m_\parallel(z)$ resulting from an applied external electric field in parallel direction of $E_\parallel = 0.05$ V/nm (Eq. 2.25) and from polarization fluctuations (Eq. 2.26). Bottom: Inverse perpendicular dielectric function $\varepsilon_\perp^{-1}(z)$ next to* (c) *the hydrophilic and* (d) *the hydrophobic diamond, calculated from the total polarization $m_\perp(z)$ (Eq. 2.30) and from an explicit expansion of the polarization up to the octupole term (Eq. 2.17). The response is calculated in two different ways: from the excess polarization $\Delta m_\perp(z)$ resulting from an applied external displacement field in perpendicular direction (Eq. 2.27) and from polarization fluctuations (Eq. 2.28). For the curves corresponding to the total polarization, the applied field is $D_\perp/\varepsilon_0 = 0.5$ V/nm. The curves corresponding to the explicit expansion (dashed-dotted lines) have been averaged over external field strengths of $D_\perp/\varepsilon_0 = 2.0$, 4.0 and 8.0 V/nm.*

explicitly included in the model. However, electronic polarizability effects on molecular interactions are implicitly included via the parametrization of the Lennard-Jones term of the water model. The number density profiles at the two surface types are shown as solid lines in Fig. 2.1 (c – d). At the hydrophilic surface, the water molecules gather very close to the surface, whereas they form a depleted layer at the hydrophobic surface, conforming to previous results [74]. Most notably, the first peak of the water density at the hydrophilic surface is significantly higher than at the hydrophobic surface.

To examine the sensitivity of the results with respect to the water model used, we run two short simulations (5 ns) of the same surfaces in contact with TIP4P/2005 water [73], which has been shown to reproduce the experimental structure factor of water very well [99]. The density profiles of TIP4P/2005 are shown as dashed lines in Fig. 2.1 (c – d). Apart from a small discrepancy in the height of the first peak, the results are very similar

to the results for SPC/E water. In particular, the minima and maxima of the density profiles coincide exactly. Although the quadrupole moment of TIP4P/2005 is $\sim 20\%$ larger than that of SPC/E (in the isotropic phase, the xx, yy and zz components of $\bar{\mathsf{P}}_2$ equal 1.65 and $1.41 \times 10^{-3}\ e\,\mathrm{nm}^2$ for TIP4P/2005 and SPC/E respectively, calculated with respect to the oxygen atom, the bar denotes averaging over all orientations), the dipole moments are almost identical (0.048 e nm for TIP4P/2005 and 0.049 e nm for SPC/E). Therefore, we expect the dielectric response of the two water models to be similar.

2.3.2 Dielectric Response

For the parallel orientation, either of the Cartesian direction x or y can be used. In the hydrophobic case, the diamond is perfectly isotropic, and the simulations give identical results in the x and y directions. In the hydrophilic case, however, there is a non-zero parallel polarization also in absence of an electric field. This kind of ferro-electric behavior is due to the anisotropy of the OH-lattice on the surface. Since proportionality is assumed only for the excess quantities $\Delta\boldsymbol{E}$ and $\Delta\boldsymbol{D}$, the polarization at zero external field does not constitute a fundamental problem when using an applied external field. Nevertheless, problems may arise when using the fluctuation equation, because the fluctuation tensor may not be diagonal. Therefore, we diagonalize the fluctuation matrix, aligning the non-zero polarization at vanishing field in one direction. The diagonal fluctuation tensor contains the eigenvalues of the fluctuation tensor for each value of z. The largest eigenvalue corresponds to the direction tangential to the surface in which $\langle\boldsymbol{M}\rangle_0 \neq 0$, the second-biggest to the surface tangential direction in which $\langle\boldsymbol{M}\rangle_0 = 0$ and the smallest eigenvalue corresponds to the direction normal to the surface. In our analysis, we use only the second-largest eigenvalue of the fluctuation tensor, which to a good approximation is not affected by the non-zero polarization at vanishing field.

The resulting profiles of the parallel dielectric function are plotted in Fig. 2.2 for (a) the hydrophilic surface and (b) the hydrophobic surface, calculated using four different methods. For the first two methods, the polarization density $m_\parallel(z)$ is calculated from Eq. 2.35. The dashed lines result from an applied electric field of $E_\parallel = 0.05$ V/nm using Eq. 2.25 and the solid lines from the fluctuations at vanishing electric field using Eq. 2.26. For both surface types, the profiles resulting from the fluctuation and applied field equations coincide excellently. For the second two methods, the polarization is estimated from the explicit expansion of Eq. 2.17 using terms up to the octupole moment. The multipole moments are calculated from Eqs. 2.10 & 2.11, where $\boldsymbol{r}_i$ is chosen to be the position of the oxygen atom. Again, the response is calculated from both an applied electric field using Eq. 2.25 (shown as dashed-dotted lines) and from the polarization fluctuations using Eq. 2.26 (shown as dotted lines). The curves of the explicit expansion follow the curves of the full polarization, confirming the equivalence of the methods for calculating the polarization. The dielectric profile is roughly proportional to the number density, as would only be expected for non-interacting dilute polar particles. Surprisingly however, the first peak in the dielectric function at the hydrophobic surface is higher than at the hydrophilic surface, in opposite order of the peak heights of the density profiles in Fig. 2.1. This disparity indicates that, although there are more polarizable molecules available in the first density peak at the hydrophilic surface, their response to an electric field is more restricted than at the hydrophobic surface. Qualitatively, this result corresponds well to our notion that water is more strongly bound at hydrophilic surfaces. At the same time, it clearly shows that the simple picture of non-interacting dilute polar molecules is

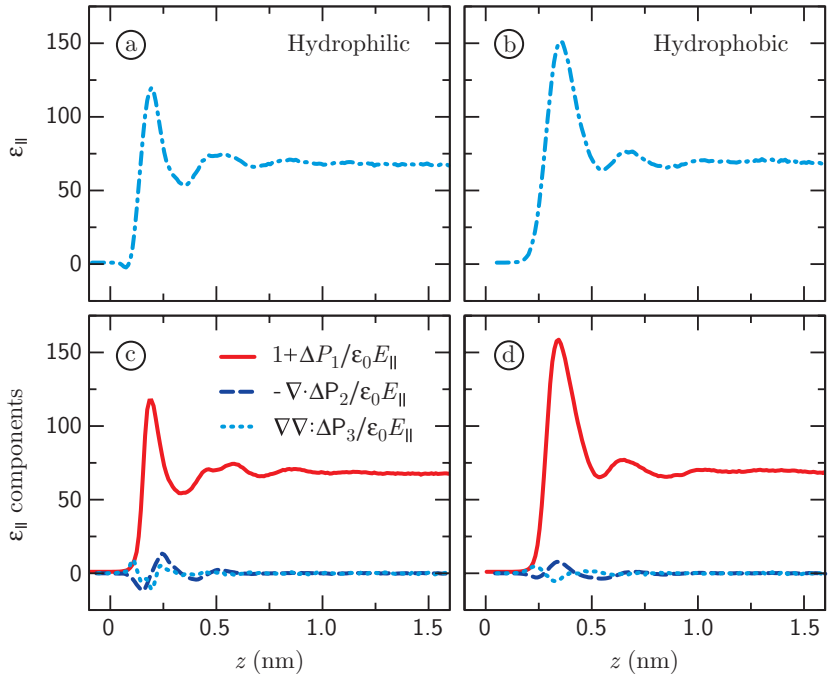

Figure 2.3: (a – b) *Parallel dielectric response calculated from the explicit multipole expansion up to the octupole using Eq. 2.10 with Eqs. 2.11 & 2.17. The monopole and dipole (solid lines), quadrupole (dashed lines) and octupole (dotted lines) contributions are shown separately at* (c) *the hydrophilic and* (d) *the hydrophobic surface. All curves are calculated from the response to an applied electric field of* $E_{\parallel} = 0.05$ *V/nm using Eq. 2.25.*

not sufficient to describe the dielectric profile of liquid water.

In Fig. 2.2 we show the inverse perpendicular dielectric function at (c) the hydrophilic surface and (d) the hydrophobic surface. Using the polarization $m_{\perp}(z)$ from Eq. 2.30, the response is calculated for an applied electric field of $D_{\perp}/\varepsilon_0 = 0.5$ V/nm (Eq. 2.27, dashed lines) and from the fluctuations (Eq. 2.28, solid lines). As for the parallel response, the curves coincide, confirming our formalism and the validity of linear response theory for the applied field strength. Strikingly, $\varepsilon_{\perp}^{-1}(z)$ passes through zero several times, which means that $\varepsilon_{\perp}(z)$ has several singularities, and that there are spatial regions where the response is negative. This overscreening behavior is reminiscent of the non-local bulk dielectric function [20], which evidently dominates the perpendicular response. The excess electric field reaches zero where $\varepsilon_{\perp}^{-1}(z) = 0$ and reverses sign in the regions where $\varepsilon_{\perp}^{-1}(z) < 0$, giving rise to several local minima in the resulting electrostatic potential, as we will discuss in more detail in subsequent sections. In bulk, the inverse dielectric response corresponds to a bulk dielectric constant of $\varepsilon_{bulk} = 75$, which is close to the literature value for SPC/E water of 71 [100]. Also shown in Fig. 2.2 (c – d) are the curves calculated from the explicit expansion of Eq. 2.17 up to the octupole moment, showing a satisfactory agreement with the response of the full polarization, as in the parallel case.

Multipole components. As the similarity of the curves in Fig. 2.2 distinctly show, the first three terms of the multipole expansion of Eq. 2.17 suffice to describe the dielectric tensor. To compare the contributions of the individual multipole moments, we show the

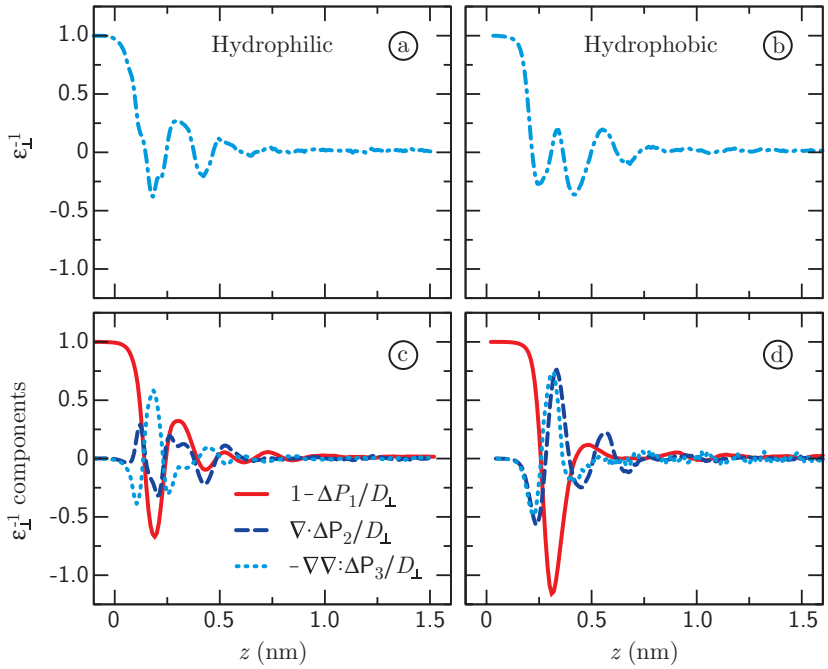

Figure 2.4: (a – b) *Inverse perpendicular dielectric response calculated from the explicit multipole expansion up to the octupole using Eq. 2.10 with Eqs. 2.11 & 2.17. The monopole and dipole (solid lines), quadrupole (dashed lines) and octupole (dotted lines) contributions are shown separately at* (c) *the hydrophilic and* (d) *the hydrophobic surface. All curves are calculated from the average response to applied electric fields of* $D_\perp/\varepsilon_0 = 2.0$, 4.0 *and* 8.0 *V/nm using Eq. 2.27.*

first three terms separately. First, the sum of the first three terms of the parallel response is shown in Fig. 2.3 at (a) the hydrophilic surface and (b) the hydrophobic surface. Second, we show the corresponding components separately in Fig. 2.3 (c – d). Quadrupole and octupole contributions show similar profiles at the two surface types, but the dipole contribution clearly dominates the parallel response. In Fig. 2.4 (a – b), we show the sum of the first three contributions to the perpendicular response, and the separate terms in (c – d). Contrary to the parallel case, the higher-order terms are non-negligible. In fact, the effect of the dipole is largely compensated for by the higher-order terms at both surface types. This clearly illustrates the importance of the higher-order electric multipoles for the perpendicular dielectric response.

Polarizability. For a dilute system of non-interacting particles, the dielectric function can be written as $1 + \alpha n(\boldsymbol{r})/\varepsilon_0$, with $n(\boldsymbol{r})$ the number density of dielectric molecules and α a microscopic polarizability attributed to each individual water molecule [96]. To describe the dielectric constant in condensed media, corrections to the polarizability appear, as in the famous Clausius-Mosotti expression. To quantify the deviation from the predicted response of a dilute system of non-interacting polar particles, we calculate the space-dependent polarizability, defined according to linear theory as

$$\frac{\alpha_\parallel(z)}{\varepsilon_0} = \frac{\varepsilon_\parallel(z) - 1}{n(z)} \quad \text{and} \quad \frac{\alpha_\perp(z)}{\varepsilon_0} = \frac{1 - \varepsilon_\perp^{-1}(z)}{n(z)}. \tag{2.36}$$

Clearly, because the dielectric profile is calculated using a non-polarizable water model,

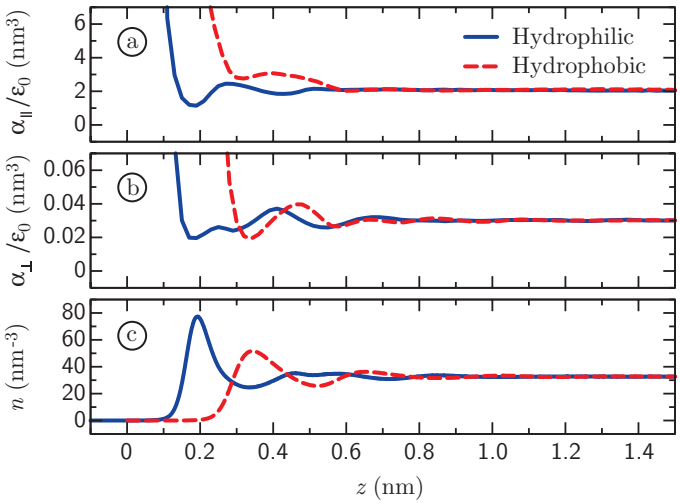

Figure 2.5: *Polarizability as a function of z calculated from Eq. 2.36 in* (a) *parallel direction and* (b) *perpendicular direction. Because of the non-polarizable water model used, the polarizability only includes multipole orientational effects. The number density is plotted in panel* (c) *for comparison.*

the polarizability $\alpha(\boldsymbol{r})$ does not explicitly include electronic, but only orientational polarization. The main question is whether the polarizability exhibits any simple relationship with the particle density. Both polarizabilities are plotted in Fig. 2.5 (a – b) as a function of z, together with the number density (c). In both the parallel and perpendicular directions and at both surface types, the polarizability exhibits a dip at the position of the highest density. Another prominent feature is that the parallel polarizability at the hydrophobic surface is always higher than in bulk, whereas the parallel polarizability decreases at the hydrophilic surface. Overall, the curves show that the relationship between the different components of the polarizability and the particle density is intricate, and depends on surface type.

Beyond linear response. In Fig. 2.6, the perpendicular component of the inverse dielectric constant (Eq. 2.27) is plotted as a function of z for different values of the external electric field strength $D_\perp/\varepsilon_0$. Apart from a slight difference between the curves taken at constant pressure (up to 1 V/nm) and constant volume, the response at the hydrophilic interface is largely independent of the applied field strength. At the hydrophobic interface, on the other hand, the dielectric response is clearly non-linear at external field strengths of 4.0 V/nm and above, as can be seen from the different responses to the different field directions. At a positive electric field of 8.0 V/nm, the overscreening seems to be slightly suppressed, as is commonly found in ionic liquids at high electric field strength [101, 102]. Thus, the linear response regime extends to higher field strengths at the hydrophilic interface. It should be noted that the curves in Fig. 2.6 are calculated using a non-polarizable water model, and therefore do not include electronic polarization or ionization effects. Experimental results indicate that on timescales of 0.01–10 μs, dielectric breakdown of water occurs at a field strength of the order of $\sim$ 0.1 V/nm [103]. That means that the non-linear response due to multipole orientational effects shown in Fig. 2.6 is not expected to play a role in the non-linear response of real water to external electric fields (note that internal fields in charged double layers can be comparable to the values used in Fig. 2.6).

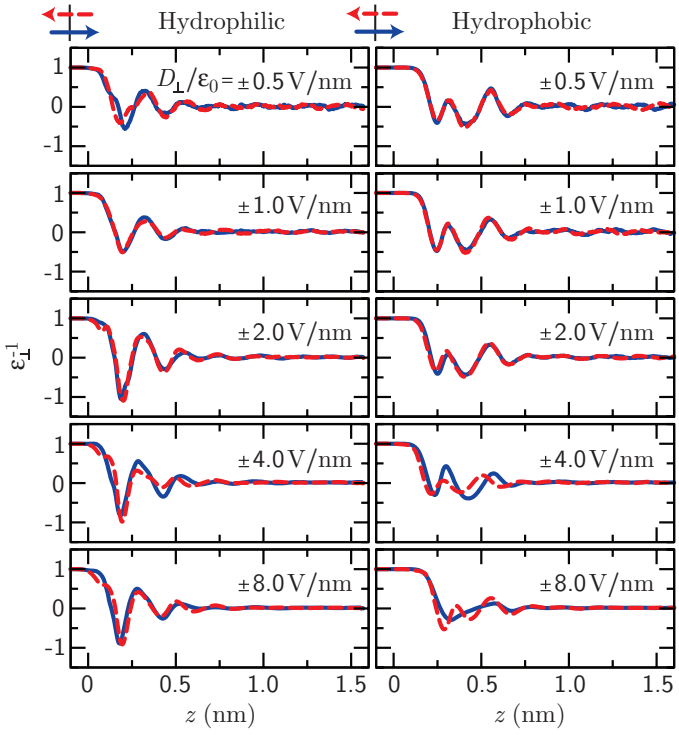

Figure 2.6: *Inverse perpendicular dielectric response function $\varepsilon_\perp^{-1}(z)$ calculated from Eq. 2.27 at different values of the external field strength $D_\perp/\varepsilon_0$. The position $z = 0$ corresponds to the oxygen layer at the hydrophilic surface and the outermost carbon layer at the hydrophobic surface.*

We plot the corresponding density profiles in Fig. 2.7. Similar to the dielectric profile, the density profile at the hydrophilic interface is independent of the external field strength, whereas the density at the hydrophobic interface gradually changes with increasing electric field strength. The non-linear response at high electric field strength has a minor, but distinct influence on the effective dielectric properties of the interface, as we will discuss in the context of the effective dielectric interface position in the section on coarse-grained modeling approaches.

2.3.3 Higher-Order Multipole Moments in Interfacial Electrostatics

The strong effect of the higher-order electric multipole moments on the interfacial water structure manifests itself not only in the dielectric response, but also in the electric field in the interfacial region in absence of an applied external electric field, and consequently in the potential difference across an aqueous interface. For instance, this surface potential difference is important for the calculation of single ion solvation free energies.

The perpendicular displacement field. In the absence of free charges, the displacement field perpendicular to the interface is constant in space. When the expansion of the displacement field is truncated after the dipole term, however, the resulting sum is certainly not constant. An illustration is provided in Fig. 2.8, where we plot the perpendicular components of the terms of Eqs. 2.15 and 2.17, summing to increasing order for the case of vanishing displacement field. As can be seen in Fig. 2.8 (b), the sum $\boldsymbol{E} + \boldsymbol{P}_1/\varepsilon_0$

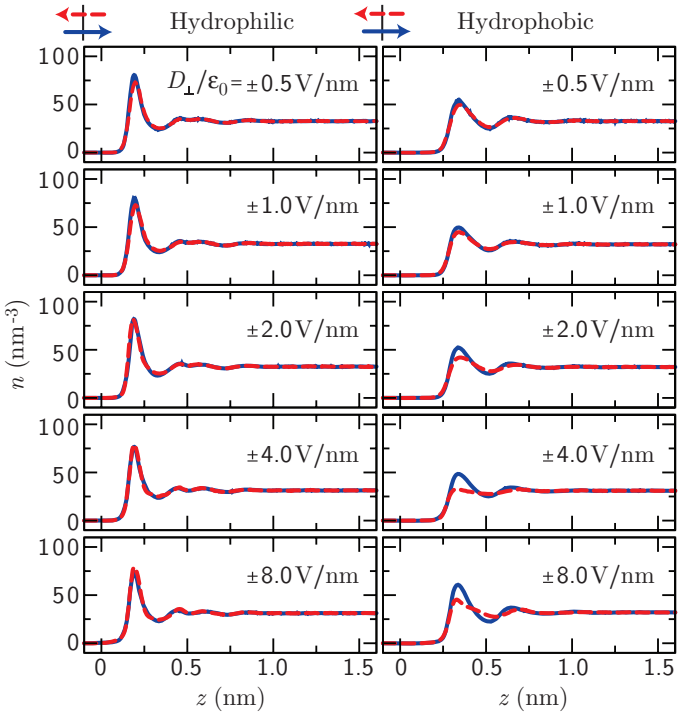

Figure 2.7: *Molecular water number density $n(z)$ at different values of the perpendicular external field strength $D_\perp/\varepsilon_0$.*

varies appreciably across the interface, but the variation is largely compensated for by the quadrupole term $-\nabla \cdot \mathsf{P}_2/\varepsilon_0$. The remaining oscillations are again almost fully compensated for by the octupole term $\nabla\nabla : \mathsf{P}_3/\varepsilon_0$ shown in Fig. 2.8 (c). The oscillations of the hexadecapole term drop below the noise level, see Fig. 2.8 (d). Evidently, the higher-order multipole moments, at least up to the octupole term, are critical to describing the electrostatics at the interface properly.

Surface potential of aqueous interfaces. The value of the electrostatic potential difference across an air-water interface has been a source of confusion for decades, with people not even agreeing on its sign. See Ref. [104] for a review. Experimental evidence indicates that the water molecules are preferentially oriented with the dipole moment pointing roughly along the surface plane at air-water interfaces [105] and at quartz-water interfaces [106, 107], leaving the question of the sign of the dipole contribution open. It is well known however, that the quadrupole contribution to the interface potential cannot be ignored [34, 108, 109]. We calculate the interface potential of the water-diamond surface, split into the dipole and quadrupole contributions. The potential profile across the interfacial layer is given by

$$\psi(z) - \psi(z_s) = -\int_{z_s}^{z} E_\perp(z')\,\mathrm{d}z'. \tag{2.37}$$

with z_s a reference position in the solid phase. In the following, we choose $\psi(z_s) = 0$. In case of a charge-free interface without external electric field, inserting Eqs. 2.15 and 2.17

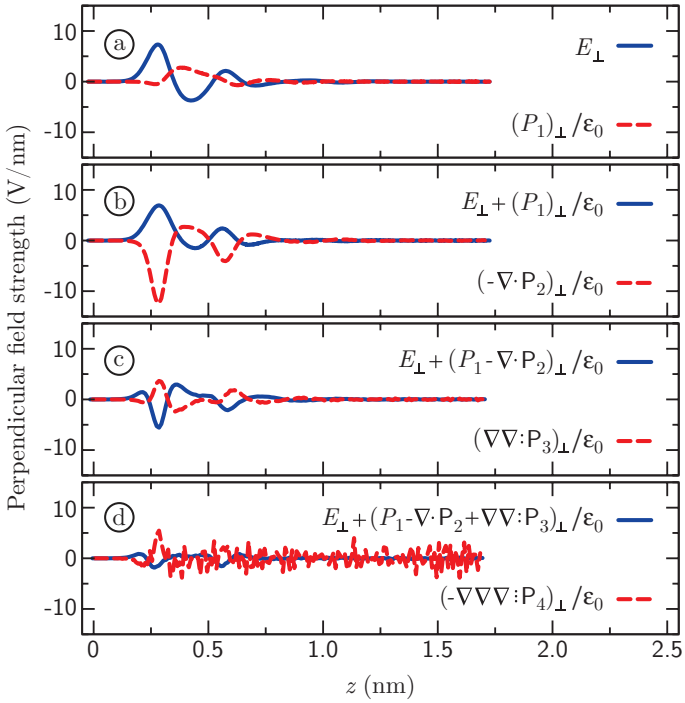

Figure 2.8: *The perpendicular components of the terms of the multipole expansion given in Eqs. 2.15 and 2.17, summing the terms to increasing order. The profiles correspond to the hydrophobic diamond surface without external displacement field. The electric field $E_\perp(z)$ is calculated from Eq. 2.29 and higher-order terms are calculated from Eqs. 2.10 & 2.11. The molecular multipole moments are calculated with respect to the oxygen atom.*

produces

$$\psi(z) = \int_{z_s}^{z} \frac{\boldsymbol{P}_1^z(z')}{\varepsilon_0}\,\mathrm{d}z' - \int_{z_s}^{z} \frac{\mathrm{d}\mathsf{P}_2^{zz}(z')}{\mathrm{d}z'\varepsilon_0}\,\mathrm{d}z', \tag{2.38}$$

where $\boldsymbol{P}_1^z(z)$ denotes the z component of the dipole density and $\mathsf{P}_2^{zz}(z)$ denotes the zz component of the quadrupole density. Higher order moments do not contribute, because integrals over the corresponding fields yield the boundary values of derivatives of the multipole densities, which vanish because of the constant value of any multipole density in both the charge-free solid and in bulk. When integrated across the entire interfacial layer, the second term of Eq. 2.38 yields the negative difference between the quadrupole density in the bulk liquid and the solid phase,

$$-\int_{z_s}^{z_l} \frac{\mathrm{d}\mathsf{P}_2^{zz}(z')}{\mathrm{d}z'\varepsilon_0}\,\mathrm{d}z' = \frac{\mathsf{P}_2^{zz}(z_s) - \mathsf{P}_2^{zz}(z_l)}{\varepsilon_0} = -\frac{\bar{\mathsf{P}}_2^{zz}}{\varepsilon_0}, \tag{2.39}$$

with z_l a position in the bulk liquid phase. The bar denotes the value in the isotropic phase. The quadrupole moment of an SPC/E water molecule in the isotropic phase is calculated by isotropic angular averaging, giving $\bar{\mathsf{p}}_2 = 1.41 \times 10^{-3}\ e\,\mathrm{nm}^2$ (xx, yy and zz components). To obtain the quadrupole density $\bar{\mathsf{P}}_2$, the molecular quadrupole moment is multiplied by the bulk water number density $n_{bulk} = 33\ \mathrm{nm}^{-3}$ and divided by ε_0, yielding

$$\frac{\bar{\mathsf{P}}_2}{\varepsilon_0} = \begin{bmatrix} 0.8428 & 0 & 0 \\ 0 & 0.8428 & 0 \\ 0 & 0 & 0.8428 \end{bmatrix} \mathrm{V}. \tag{2.40}$$

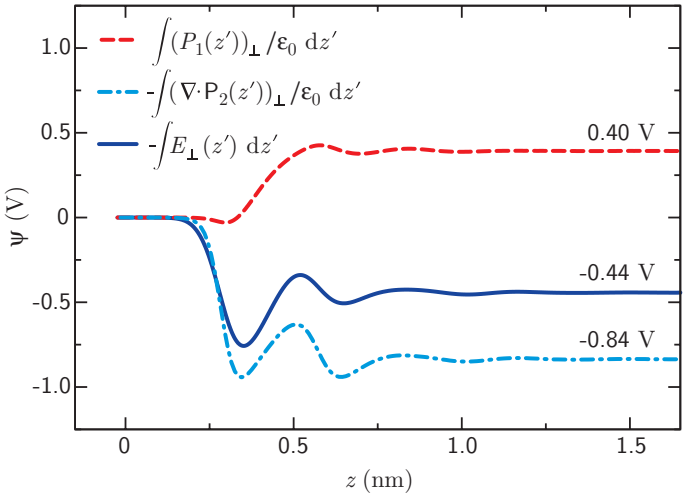

Figure 2.9: *Electrostatic potential profile across a charge-free hydrophobic diamond-water interface calculated from the electric field (Eq. 2.37, solid line) and split into the two components of Eq. 2.38: the dipole contribution (dashed line) and the quadrupole contribution (dashed-dotted line). The potential is calculated with respect to the reference electrostatic potential in the solid phase.*

In Fig. 2.9, the potential profile across the interface, calculated from simulations of the hydrophobic diamond in water, is plotted as a function of the perpendicular coordinate z. The solid dark-blue line indicates the profile as calculated from Eq. 2.37, giving a potential difference of -0.44 V between bulk liquid and solid. Taking only the dipole contribution into account yields 0.40 V (red dashed line in Fig. 2.9), which has the opposite sign. The voltage drop is restored to the correct value upon addition of the quadrupole contribution (dashed-dotted light-blue line), which equals the value calculated from averaging the quadrupole moment of the SPC/E water model over all orientations (Eq. 2.40). Although the molecular dipole moment does not depend on the choice of origin, both the dipole and quadrupole density depend on the reference point chosen for the expansion. For water there is no choice of origin for which either one vanishes. Therefore, both contributions are important for the total interface potential, but the relative values of the dipolar and quadrupolar contributions vary depending on the choice of origin.

2.4 Coarse-Grained Modeling Approaches

2.4.1 Dielectric Dividing Surface

Instead of using the profile of the inverse dielectric response function, the dielectric profile at an interface can be modeled by a sharp discontinuity, but shifted with respect to the Gibbs dividing surface. The Gibbs dividing surface, which is the thermodynamically defined interface position, is calculated as usual,

$$z^{\mathrm{GDS}} = z_s + \int_{z_s}^{z_l} \frac{n(z_l) - n(z)}{n(z_l) - n(z_s)} \, \mathrm{d}z, \tag{2.41}$$

Table 2.1: *Dielectric and Gibbs dividing surfaces of the two different surface types measured with respect to the position of the outermost heavy atoms, i.e. the oxygen atoms of the hydroxyl group at the hydrophilic surface and the carbon atoms at the hydrophobic surface.*

Surface type	z^{GDS} (nm)	$z_{\parallel}^{\mathrm{DDS}}$ (nm)	$z_{\perp}^{\mathrm{DDS}}$ (nm)
Hydrophilic	0.07	0.09	0.10
Hydrophobic	0.22	0.08	0.12

with $n(z)$ the water density and z_l and z_s positions in the bulk liquid and solid phase respectively. Equivalent to Eq. 2.41, we introduce the dielectric dividing surface,

$$z^{\mathrm{DDS}} = z_s + \int_{z_s}^{z_l} \frac{f(z_l) - f(z)}{f(z_l) - f(z_s)} \, \mathrm{d}z. \tag{2.42}$$

For the parallel dielectric dividing surface we take $f(z) = \varepsilon_{\parallel}(z)$, and for the perpendicular dielectric dividing surface we take $f(z) = \varepsilon_{\perp}^{-1}(z)$. The values of z^{GDS}, $z_{\parallel}^{\mathrm{DDS}}$ and $z_{\perp}^{\mathrm{DDS}}$ at vanishing external field are summarized in Tab. 2.1. The Gibbs dividing surface position clearly shows that water at the hydrophilic surface moves close to the interface, whereas water retreats from the hydrophobic surface. However, this difference in depletion layer hardly manifests itself in the position of the dielectric dividing surface, which is similar for both surface types. To quantify the difference between the two surface types, we look at the dielectric interface shift $\delta = z^{\mathrm{DDS}} - z^{\mathrm{GDS}}$. From Tab. 2.1 it follows $\delta_{\perp}^{\mathrm{phob}} = -0.10$ nm and $\delta_{\parallel}^{\mathrm{phob}} = -0.14$ nm at the hydrophobic surface and $\delta_{\perp}^{\mathrm{phil}} = 0.03$ nm and $\delta_{\parallel}^{\mathrm{phil}} = 0.02$ nm at the hydrophilic surface. Interestingly, the difference in parallel and perpendicular dielectric interface shift is relatively small, whereas the different surface types actually give rise to shifts of opposite sign. This remarkable difference in the dielectric interface shift signifies that water at the hydrophobic surface is a "better dielectric" than at the hydrophilic surface. For the perpendicular profile, the width of the dielectric variation has been defined earlier in a similar way [24, 25]. The difference between the two definitions is that $z_{\perp}^{\mathrm{DDS}}$ as defined in Eq. 2.42 guarantees that the electrostatic potential far away from the interface is correctly reproduced. This can be seen by realizing that $z_{\perp}^{\mathrm{DDS}}$ corresponds to the position where the extrapolated linear fits to the solid and bulk liquid potential profile cross each other, see Fig. 2.10 (a). Using $\nabla\psi(z) = -E_{\perp}(z)$ and Eqs. 2.4 and 2.42, the electrostatic potential difference between the liquid and the solid is given by

$$\begin{aligned} \varepsilon_0 \left(\psi(z_l) - \psi(z_s)\right) &= -D_{\perp} \int_{z_s}^{z_l} \varepsilon_{\perp}^{-1}(z) \, \mathrm{d}z \\ &= -D_{\perp} \left(\int_{z_s}^{z_{\perp}^{\mathrm{DDS}}} \mathrm{d}z + \int_{z_{\perp}^{\mathrm{DDS}}}^{z_l} \frac{\mathrm{d}z}{\varepsilon_{bulk}} \right), \end{aligned} \tag{2.43}$$

for a constant displacement field $D_{\perp}$. Therefore, using a sharp-kink approximation of the dielectric profile,

$$\varepsilon_{\perp}(z) = \begin{cases} 1 & \text{if } z < z_{\perp}^{\mathrm{DDS}} \\ \varepsilon_{bulk} & \text{otherwise,} \end{cases} \tag{2.44}$$

ensures the correct asymptotic voltage profile far away from the interface. To compare the dielectric interface position with the Gibbs dividing surface, the density profile and

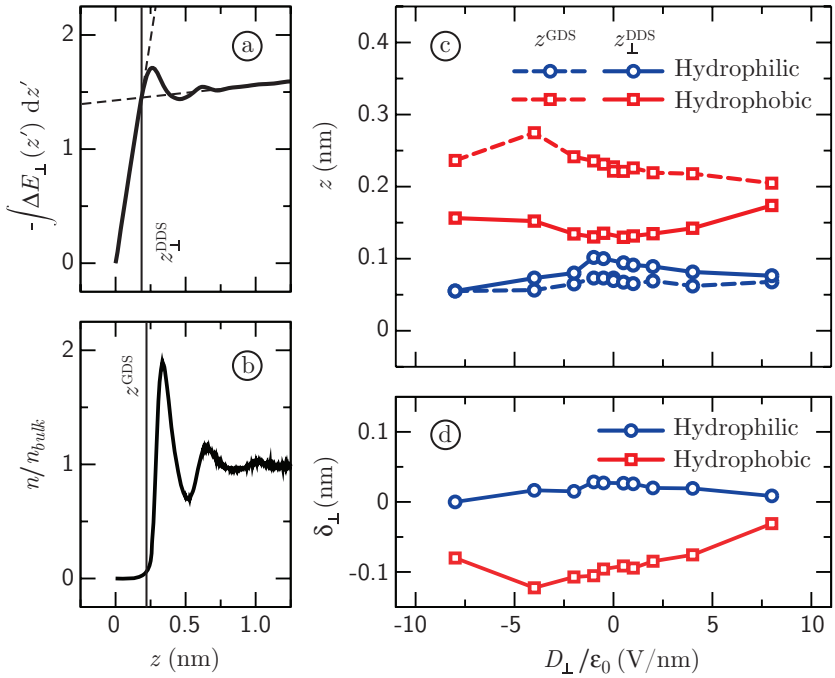

Figure 2.10: (a) *Graphical representation of the construction of the perpendicular dielectric dividing surface* $z_\perp^{DDS}$ *by extrapolation of the bulk potential profile (Eq. 2.42, where* $\Delta E_\perp$ *is calculated from Eq. 2.29 in separate simulations with and without external displacement field). The curve shown corresponds to an external displacement field of* $D_\perp/\varepsilon_0 = 8.0$ *V/nm.* (b) *Corresponding Gibbs dividing surface* z^{GDS}. (c) *Positions of the perpendicular dielectric dividing surface* $z_\perp^{DDS}$ *and the Gibbs dividing surface* z^{GDS} *as a function of the applied perpendicular electric field.* (d) *Perpendicular dielectric interface shift* $\delta_\perp = z_\perp^{DDS} - z^{GDS}$ *as a function of the applied perpendicular electric field.*

the Gibbs dividing surface z^{GDS} are shown in Fig. 2.10 (b). In Fig. 2.10 (c), we show the positions of z^{GDS} and $z_\perp^{DDS}$, showing a mild dependence on the external displacement field strength. For all values of the external displacement field, the dielectric dividing surface is located close to the Gibbs dividing surface at the hydrophilic surface, displaced slightly into the fluid, whereas at the hydrophobic surface, the dielectric interface is shifted toward the solid surface. The perpendicular dielectric interface shift, defined as $\delta_\perp = z_\perp^{DDS} - z^{GDS}$, is shown in Fig. 2.10 (d). At the hydrophilic surface, the dielectric interface shift slightly declines at high external field strength, which means that the water becomes a slightly better dielectric. At the hydrophobic surface, on the other hand, the dielectric interface shift not only depends on the applied field strength, but also on the field direction, in line with our results for the dielectric profiles. The trend as a function of field strength, however, is to increase $\delta_\perp^{phob}$, which means that the dielectric becomes slightly worse.

2.4.2 Modified Poisson-Boltzmann Equation

We consider a charged planar surface with monovalent counterions, where the charge density is laterally averaged and depends only on the z direction. For a charged surface with counterions in solution neither $\boldsymbol{E}(z)$ nor $\boldsymbol{D}(z)$ is constant, so the integral of Eq. 2.3 does not yield a local dielectric function automatically. Therefore, inspired by Eq. 2.4, we

assume

$$\varepsilon_0 E_\perp(z) = \varepsilon_\perp^{-1}(z)\, D_\perp(z), \tag{2.45}$$

which is a good approximation when $D_\perp(z)$ varies slowly, *i.e.* at low salt concentration and at low surface charge density. Taking the divergence of Eq. 2.45 and using $\nabla\psi(z) = -E_\perp(z)$ leads to

$$\varepsilon_0 \frac{\mathrm{d}^2\psi}{\mathrm{d}z^2} = -D_\perp(z)\frac{\mathrm{d}\varepsilon_\perp^{-1}}{\mathrm{d}z} - \varepsilon_\perp^{-1}(z)\frac{\mathrm{d}D_\perp}{\mathrm{d}z}. \tag{2.46}$$

Inserting the Boltzmann expression for the ion density,

$$\frac{\mathrm{d}D_\perp}{\mathrm{d}z} = P_0(z) = -2ec_0 \sinh\left[-\beta e\psi(z)\right]\exp\left[-\mu(z)\right], \tag{2.47}$$

with c_0 the ionic concentration in bulk, we arrive at the modified Poisson-Boltzmann equation,

$$\varepsilon_0 \frac{\mathrm{d}^2\psi}{\mathrm{d}z^2} = -D_\perp(z)\frac{\mathrm{d}\varepsilon_\perp^{-1}}{\mathrm{d}z} + 2ec_0 \sinh\left[-\beta e\psi(z)\right]\exp\left[-\mu(z)\right]\varepsilon_\perp^{-1}(z). \tag{2.48}$$

The potential $\mu(z)$ contains all non-electrostatic contributions from the interface, such as steric and solvophobic effects. The displacement field in the first term of Eq. 2.48 is calculated as

$$D_\perp(z) = \int_0^z P_0\left(z'\right)\mathrm{d}z', \tag{2.49}$$

making Eq. 2.48 a second order integro-differential equation. Eqs. 2.47–2.49 are solved numerically, imposing a fixed surface charge density σ_0 as a boundary condition at $z = 0$. The position $z = 0$ corresponds to the oxygen atoms at the hydrophilic surface and to the outermost carbon atom at the hydrophobic surface.

Electrostatic potential. We calculate the electrostatic potential close to a surface carrying a minute surface charge density $\sigma_0 = -0.006\ e/\mathrm{nm}^2$ ($-1\ \mathrm{mC/m}^2$) at a salt concentration of 100 mM (0.1 mol/l). The effect that the finite salt concentration may have on the dielectric profile $\varepsilon_\perp(z)$ can be expressed in terms of the ionic excess polarizabilities $\Delta\alpha_\pm$,

$$\varepsilon_\perp(z) = \varepsilon_\perp^{\mathrm{H_2O}}(z) + \frac{c_+(z)\,\Delta\alpha_+}{\varepsilon_0} + \frac{c_-(z)\,\Delta\alpha_-}{\varepsilon_0}, \tag{2.50}$$

with $\varepsilon_\perp^{\mathrm{H_2O}}(z)$ the pure water profile that we have calculated. In the following we set $\Delta\alpha_\pm = 0$, which means that any effect that the finite salt concentration may have on the profile $\varepsilon_\perp^{-1}(z)$ is ignored. The electrostatic potential is shown in Fig. 2.11 (a – c) for two different choices of $\mu(z)$: without a non-electrostatic interaction, $\mu(z) = 0$, and including a generic soft-wall repulsion, modeled by

$$\mu(z) = \gamma\exp\left[1 - z/\lambda\right], \tag{2.51}$$

with λ the size of a typical ionic radius, $\lambda = 0.15$ nm and $\gamma = 1$. Strikingly, the electrostatic potential at the hydrophobic interface changes sign between 0.2 and 0.4 nm from the wall, locally enhancing the concentration of co-ions. This means that locally, the charge on the surface is overscreened by the sum of polarization and ionic charges, a phenomenon that is well known to occur in ionic liquids as well [102]. In Fig. 2.11 (d – f) we plot the corresponding perpendicular electric field $E_\perp(z)$ and the perpendicular displacement

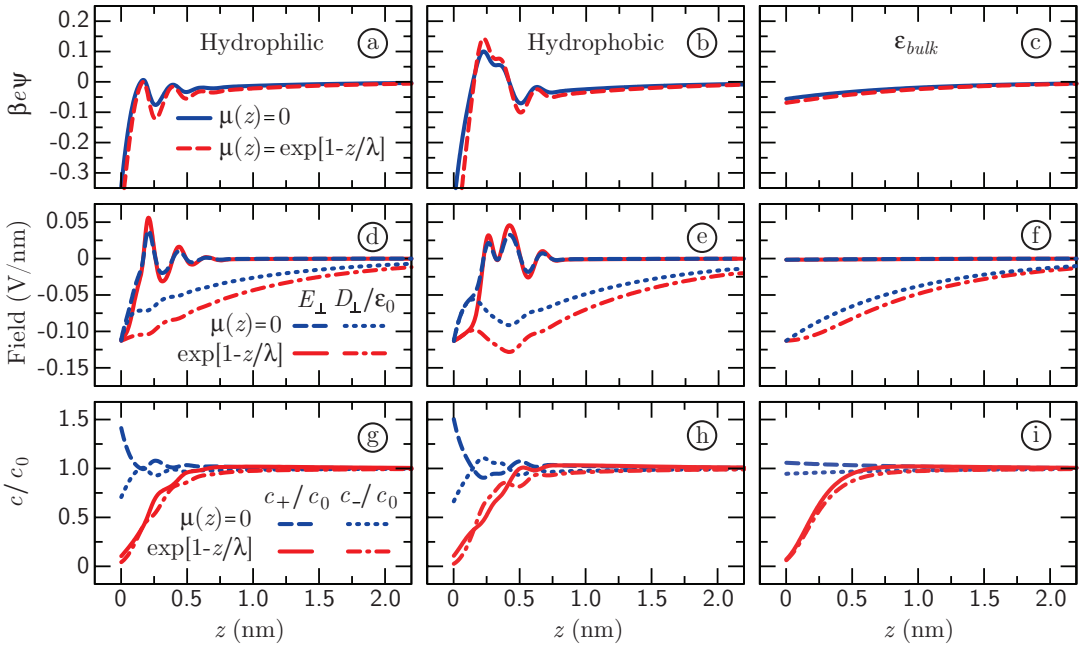

Figure 2.11: (a – c) *Electrostatic potential next to a charged surface ($\sigma_0 = -0.006\ e/nm^2$), calculated from the Poisson-Boltzmann equation (Eq. 2.48) and different models of the dielectric function $\varepsilon_\perp^{-1}(z)$. Curves are shown for the hydrophilic profile (left), the hydrophobic profile (middle), and $\varepsilon_\perp^{-1}(z) = \varepsilon_{bulk}^{-1}$ (right). The bulk salt concentration is $c_0 = 100\ mM$.* (d – f) *Perpendicular electric field $E_\perp(z)$ and the perpendicular displacement field $D_\perp(z)/\varepsilon_0$.* (g – i) *Corresponding ionic density profiles c_+ (positive ions, solid lines) and c_- (negative ions, dashed lines), normalized on the bulk density c_0. We have used either no non-electrostatic potential ($\mu(z) = 0$) or the repulsive potential of Eq. 2.51 ($\mu(z) = \exp[1 - z/\lambda]$ with $\lambda = 0.15\ nm$).*

field $D_\perp(z)/\varepsilon_0$. Importantly, the displacement field $D_\perp(z)$ varies more slowly than the electric field $E_\perp(z)$, which justifies the use of the local approximation of Eq. 2.45. The ionic densities $c_\pm(z) = c_0 \exp[\mp\beta e\psi(z) - \mu(z)]$ are plotted in Fig. 2.11 (g – i), clearly showing the effect of overscreening at the hydrophobic surface. Remarkably, when the dielectric profile is used instead of ε_{bulk}, the ions accumulate closer to the surface. The soft-wall repulsion, on the other hand, pushes the ions away from the surface, although its effect on the electrostatic potential profile is minor. That means that in cases where the non-electrostatic repulsion is less pronounced, we expect the counterions to be strongly bound to the surface because of dielectric effects.

2.4.3 Capacitance of the Double Layer

The double-layer structure of the charged interface and its counterion cloud gives rise to a capacitance. The vast amount of experimental data on interfacial capacitances provides a direct test of the model for the dielectric profile. Because the point of vanishing surface potential $\psi_0 = \psi(0)$ is hard to determine and because the capacitance may depend on the surface potential, the differential capacitance is generally reported,

$$C = \frac{\mathrm{d}\sigma_0}{\mathrm{d}\psi_0}. \tag{2.52}$$

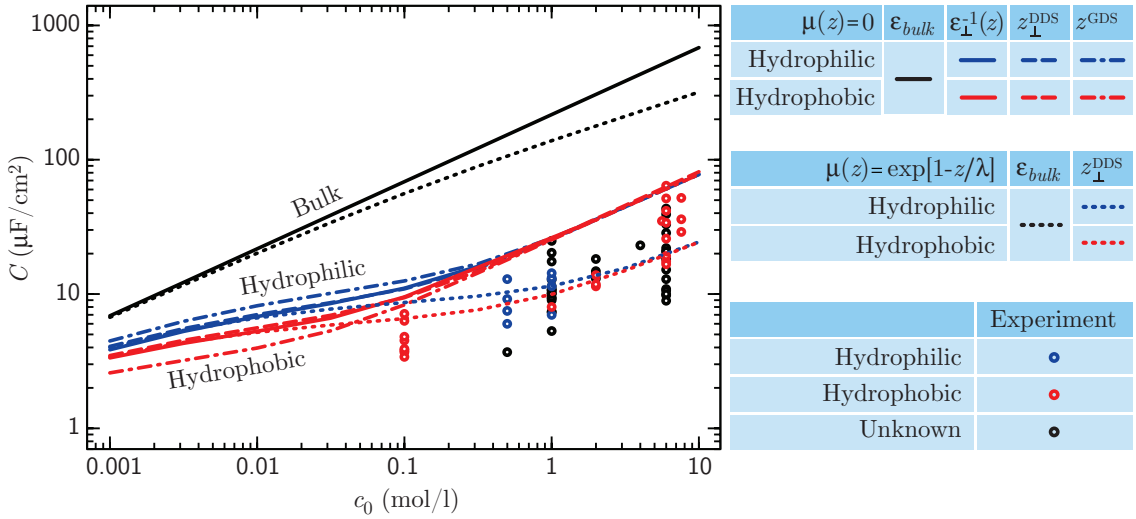

Figure 2.12: *Capacitance of the double layer, from Eq. 2.52 and the solution to the Debye-Hückel equation (Eq. 2.53). The black lines are calculated assuming bulk permittivity in the entire fluid and* $\mu(z) = 0$ *(solid line) or* $\mu(z) = \exp[1 - z/\lambda]$ *(dotted line). The blue lines (hydrophilic) and red lines (hydrophobic) are calculated using different approximations for the dielectric properties: the full profile* $\varepsilon_\perp^{-1}(z)$ *or the sharp-kink approximation of Eq. 2.44 at either the dielectric dividing surface* $z_\perp^{\mathrm{DDS}}$ *or the Gibbs dividing surface* z^{GDS}*.*

We calculate the differential capacitance of a Poisson-Boltzmann distribution of ions next to a charged surface, comparing the models for the dielectric profile discussed above. Using the non-linear Poisson-Boltzmann equation, the differential capacitance depends on the surface charge density, but using the Debye-Hückel approximation, the differential capacitance is constant and equal to the capacitance from the non-linear Poisson-Boltzmann equation in the limit $\sigma_0 \to 0$. The Debye-Hückel limit is obtained by approximating Eq. 2.48 for small $\psi(z)$,

$$\varepsilon_0 \frac{\mathrm{d}^2\psi}{\mathrm{d}z^2} = -D_\perp(z) \frac{\mathrm{d}\varepsilon_\perp^{-1}}{\mathrm{d}z} - 2ec_0\beta e\,\psi(z)\,\exp\left[-\mu(z)\right]\varepsilon_\perp^{-1}(z)\,, \tag{2.53}$$

which has to be solved together with Eq. 2.49. In Fig. 2.12, we show the double-layer capacitance using the different models for the interfacial dielectric properties discussed above, comparing the results to experimental data. The blue circles in Fig. 2.12 denote experimental data on surfaces that are known to be hydrophilic (contact angle below 90°), the red circles denote data on hydrophobic surfaces, and the black circles denote data on surfaces of which the contact angle is unknown. The electrolytes used in the experiments are sulfuric acid (H_2SO_4) and potassium hydroxide (KOH). See Appendix A for further details and references. As a first model, we show the differential capacitance of Eq. 2.52 as a function of salt concentration c_0 using a dielectric constant equal to ε_{bulk} and $\mu(z) = 0$ (black solid line), which overestimates the experimental data by at least an order of magnitude. This discrepancy led Stern to propose a model where a thin layer at the interface has a lower dielectric constant than the bulk fluid [22]. Second, we include the generic soft-wall repulsion given in Eq. 2.51, with $\lambda = 0.15$ nm and $\gamma = 1$. The capacitance, shown as a black dotted line, captures neither the trend nor the magnitude of the experimental data much better. Third, we use our calculated full dielectric profile

$\varepsilon_\perp^{-1}(z)$, shown in Fig. 2.2 (c – d), with $\mu(z) = 0$ (solid colored lines), agreeing much better with experiments. The hydrophilic profile (blue) yields a slightly higher capacitance than the hydrophobic profile (red) at low salt concentration, which is generally expected because of the better wetting characteristics [30]. The difference is minor however, because the dielectric interface shift $\delta_\perp$ largely compensates for the depletion gap at hydrophobic surfaces. Fourth, we use the sharp-kink approximation of Eq. 2.44 with $\mu(z) = 0$ (dashed colored lines). The results are almost indistinguishable from the curves calculated using the full profiles $\varepsilon_\perp^{-1}(z)$, as expected from the fact that the dielectric dividing surface is designed to reproduce the electrostatic potential far away from the interface. Nevertheless, the calculated capacitance is still relatively high compared to the experimental data, which has to do with the fact that in the Poisson-Boltzmann approach the point-charge ions are allowed to get arbitrarily close to the surface. Therefore, as a fifth model, we use the sharp-kink approximation of Eq. 2.44 together with $\mu(z)$ from Eq. 2.51, shown as dotted colored lines. Clearly, this model follows the experimental data very well. Values of the calculated capacitance can be adjusted by fine-tuning the parameters γ and λ, which are expected to depend on the surface and ion type. Finally, we show the capacitance using a sharp-kink approximation for $\varepsilon_\perp^{-1}(z)$ located at z^{GDS} (dashed-dotted lines), which does not perform as well as the sharp-kink approximation located at $z_\perp^{\mathrm{DDS}}$. In fact, when using the Gibbs dividing surface, the difference between hydrophilic and hydrophobic surfaces is quite large at low salt concentration, which does not seem to be reflected in the experimental data. Turning this argument around, the approximate equality of experimental data for the double-layer capacitance on hydrophilic and hydrophobic surfaces displayed in Fig. 2.12 can be viewed as a confirmation of one of the main results of the present work, namely that the effect of the depletion layer at hydrophobic surfaces is largely compensated for by the dielectric properties of the first few interfacial water layers, effectively yielding dielectric properties similar to those at hydrophilic surfaces.

Effective Stern layer permittivity. Within the original Stern model of a charge-free interfacial region of width d with dielectric constant ε_{int}, the capacitance turns out to be $C_{Stern} = \sigma_0/\psi_0 = \varepsilon_{int}\,\varepsilon_0/d$. The same model yields $C_{bulk} = \varepsilon_{bulk}\,\varepsilon_0/d$ when the bulk value $\varepsilon = \varepsilon_{bulk}$ is assumed for the interfacial dielectric constant. Therefore the capacitance ratio reflects the ratio of interfacial dielectric constants,

$$\frac{C_{Stern}}{C_{bulk}} = \frac{\varepsilon_{int}}{\varepsilon_{bulk}}. \tag{2.54}$$

Imposing Eq. 2.54, and dividing the capacitance which follows from the solution of the Poisson-Boltzmann equation including the dielectric profile $\varepsilon_\perp^{-1}(z)$ by the capacitance using the bulk assumption $\varepsilon_\perp^{-1}(z) = \varepsilon_{bulk}^{-1}$, we find that the estimate for ε_{int} varies between 10 and 30, depending on salt concentration, which corresponds well to earlier estimates based on experimental data [80, 81]. Our results present a microscopic picture of the electrostatic properties of the interfacial layer, allowing for the analysis of not only the double-layer capacitance, but also other properties, such as the electrostatic pressure between two plates as a function of separation, as will be detailed next.

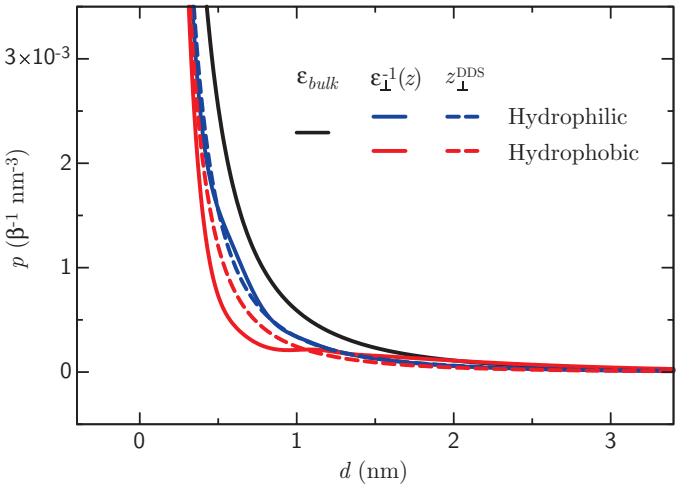

Figure 2.13: *Pressure between two like-charged hydrophilic and hydrophobic plates as a function of the distance d between the plates, calculated from Eqs. 2.55 and 2.56 using different models for the dielectric profiles* $\varepsilon_\perp^{-1}(z)$*. The surface charge density is* $\sigma_0 = -0.006\ e\ nm^{-2}$*.*

2.4.4 Disjoining Pressure between Charged Plates

We determine the disjoining pressure between two plates from the free energy $\mathcal{F}$ calculated using the Poisson-Boltzmann equation [80, 110–112],

$$\beta\mathcal{F} = \beta\sigma_0\psi_0 + \int \frac{\beta\psi(z)}{2} P_0(z) + \sum_{\pm} c_\pm(z) \left[\mu(z) + \ln\frac{c_\pm(z)}{c_0} - 1\right] \mathrm{d}z, \tag{2.55}$$

with σ_0 the surface charge density, $\psi_0 = \psi(0)$ the potential at the wall and $c_\pm(z) = c_0 \exp\left[\mp\beta e\psi(z) - \mu(z)\right]$ the ionic densities. The potential $\psi(z)$ is calculated from the non-linear Poisson-Boltzmann equation given in Eq. 2.48. The first term in Eq. 2.55 comes from the surface integral over the electrostatic energy of the surface charge density. The pressure $p(d)$ between two plates at separation d is given by

$$\beta p(d) = -\frac{\mathrm{d}\beta\mathcal{F}}{\mathrm{d}d} - 2c_0. \tag{2.56}$$

For the dielectric profile between the two plates, we join the $\varepsilon_\perp^{-1}(z)$ profiles from both surfaces piecewise. The resulting pressure is shown in Fig. 2.13 for a 100 mM monovalent salt solution and a surface charge of $\sigma_0 = -0.006\ e\ \mathrm{nm}^{-2}$ ($-1\ \mathrm{mC/m^2}$), with $\mu(z) = 0$. Compared to a spatially constant bulk dielectric function (solid black line), the pressure is lower when the full dielectric profile $\varepsilon_\perp^{-1}(z)$ (solid colored lines) or the sharp-kink approximation of Eq. 2.44 (colored dashed lines) is used. Therefore, modifications of the pressure between charged surfaces due to dielectric surface effects cannot explain, and probably are also not related to, the exponentially decaying short-ranged hydration repulsion, which is found experimentally and theoretically between all kinds of polar surfaces [92, 113]. Based on a mean-field type interpretation (without taking the dielectric profile into account) of pressures obtained within atomistic simulations of charged surfaces, the hydration repulsion has been associated with dielectric effects [114]. This differs from our findings, according to which dielectric effects decrease the pressure between charged surfaces and therefore the hydration repulsion must come from solvation effects not directly

connected to dielectric properties. Interestingly, the repulsion at short distances in Fig. 2.13 is found to be smaller between hydrophobic surfaces than between hydrophilic ones. It is important to note that the pressures derived from the modified Poisson-Boltzmann equation shown in Fig. 2.13 do not include hydration or solvophobic effects and consequently vanish for zero surface charge density. Therefore, the message is that the dielectric profile cannot explain the hydration repulsion (which also acts between neutral surfaces) but nevertheless influences the electrostatic part of the double-layer pressure and in fact makes the pressure between similarly charged surfaces less repulsive.

2.4.5 Ion-Surface Interactions

Correlated electrostatic effects such as the image charge repulsion at a dielectric boundary cannot be treated on the mean-field level. However, for a single, finite-sized ion crossing a dielectric boundary, the image charge repulsion has been calculated in Refs. [115, 116], involving the effective dielectric radius of the ion. Tentatively, free energies calculated this way may be included as a correction to the mean-field potential similar to the heuristic potential $\mu(z)$. The image charge repulsion depends on the ionic radius, but ionic radii inferred from crystal structures are too small and consistently overestimate hydration free energies. To reproduce the Born solvation free energy, the distance between the ion and the first water dipole has to be added to the crystal radius, see Refs. [117, 118] and references therein. Motivated by our results for the planar interface, which show that density and dielectric properties give rise to two distinct and largely independent length scales, we propose a model for the ionic interaction with surfaces that distinguishes between dielectric and non-electrostatic solvation-induced ion-surface interactions. Similar to the Gibbs and dielectric dividing surfaces at planar interfaces, we introduce the ionic cavity radius λ_c and the dielectric radius λ_d, see Fig. 2.14 (a – c). The expression for the image potential is taken directly from Ref. [116]. We define the distance of the ion center to the dielectric dividing surface position $z_\perp^{\mathrm{DDS}}$ as $z' = z - z_\perp^{\mathrm{DDS}}$. For $z' > \lambda_d$, the image potential of a monovalent ion is given by

$$\begin{aligned} U_i(z') = \frac{\beta e^2}{32\pi\,\lambda_d\,\varepsilon_0\varepsilon_1} \Bigg[& 4 + \frac{(\varepsilon_1-\varepsilon_2)}{(\varepsilon_1+\varepsilon_2)} \frac{2\lambda_d}{z'} \\ & + \frac{(\varepsilon_1-\varepsilon_2)^2}{(\varepsilon_1+\varepsilon_2)^2} \left(\frac{2\lambda_d^2}{\lambda_d^2 - (2z')^2} + \frac{\lambda_d}{2z'} \ln \frac{2z'+\lambda_d}{2z'-\lambda_d} \right) \Bigg], \end{aligned} \tag{2.57}$$

and for $0 < z' < \lambda_d$ by

$$\begin{aligned} U_i(z') = \frac{\beta e^2}{32\pi\,\lambda_d\,\varepsilon_0\varepsilon_1} \Bigg[& 2 + \frac{2z'}{\lambda_d} + \frac{\varepsilon_1-\varepsilon_2}{\varepsilon_1+\varepsilon_2} \left(4 - \frac{2z'}{\lambda_d} \right) \\ & + \frac{(\varepsilon_1-\varepsilon_2)^2}{(\varepsilon_1+\varepsilon_2)^2} \left[\frac{(\lambda_d+z')(\lambda_d-2z')}{\lambda_d^2+2z'\lambda_d} + \frac{\lambda_d}{2z'} \ln \frac{2z'+\lambda_d}{\lambda_d} \right] \Bigg] \\ & + \frac{\beta e^2}{16\pi\,\lambda_d\,\varepsilon_0\varepsilon_2} \left(\frac{2\varepsilon_2}{\varepsilon_1+\varepsilon_2} \right)^2 \left(1 - \frac{z'}{\lambda_d} \right). \end{aligned} \tag{2.58}$$

The permittivities $\varepsilon_1 = \varepsilon_{bulk}$ and $\varepsilon_2 = 1$ for $z' > 0$. For $z' < 0$, the same expressions can be used with $\varepsilon_1 = 1$ and $\varepsilon_2 = \varepsilon_{bulk}$. Because we calculate the energy with respect to a position in the bulk water, we subtract the Born energy $U_b = e^2/8\pi\lambda_d\varepsilon_0\varepsilon_{bulk}$ from U_i. In

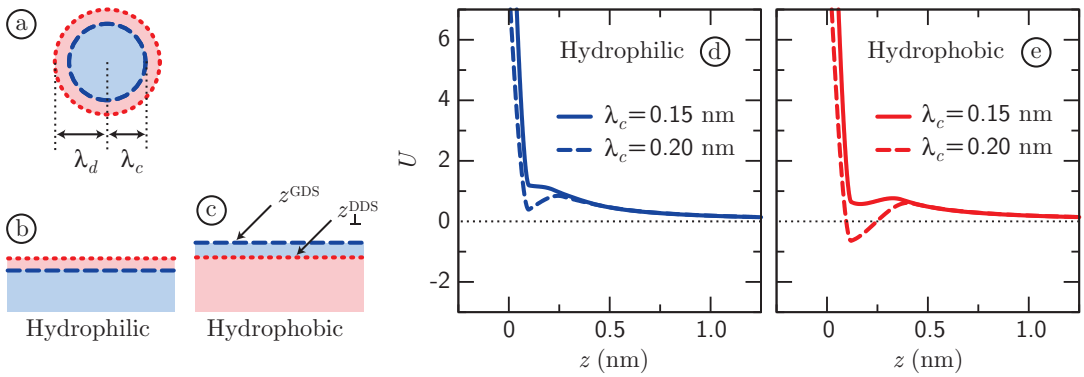

Figure 2.14: (a) *Sketch of an ion with cavity radius* λ_c *(blue dashed line) and dielectric radius* λ_d *(red dotted line). Also shown are sketches of* (b) *a hydrophilic and* (c) *a hydrophobic surface with their respective Gibbs (blue dashed lines) and dielectric dividing surfaces (red dotted lines).* (c – d) *Ionic free energy* $U(z) = U_h(z) + U_i(z) - U_b$ *at* (d) *a hydrophilic surface and* (e) *a hydrophobic surface, calculated from Eqs. 2.57-2.59. At the hydrophilic surface* $z_\perp^{DDS} = 0.10$ *nm and* $z^{GDS} = 0.07$ *nm, at the hydrophobic surface* $z_\perp^{DDS} = 0.12$ *nm and* $z^{GDS} = 0.22$ *nm. The ions have a cavity radius of* $\lambda_c = 0.15$ *nm and* $\lambda_c = 0.2$ *nm and the dielectric radii* λ_d *are* 0.1 *nm larger.*

addition to the image potential, the ions are subject to a hydration potential, scaling with the hydrated volume of the ion [67, 119–121]. To calculate the ionic volume, we use the cavity radius λ_c. Whereas the image potential acts with respect to the dielectric dividing surface, the hydration potential acts with respect to the Gibbs dividing surface. These surface positions appear in different order at hydrophilic and hydrophobic surfaces. The hydration energy is calculated from

$$U_h(z'') = \begin{cases} -\frac{4\pi}{3}\lambda_c^3 \beta C & \text{if } z'' < -\lambda_c \\ 0 & \text{if } z'' > \lambda_c \\ -\frac{\pi}{3}(\lambda_c - z'')^2 (z'' + 2\lambda_c)\,\beta C & \text{otherwise,} \end{cases} \tag{2.59}$$

with $z'' = z - z^{GDS}$ and $C = 2.8 \times 10^{-19}$ J/nm^3 [67]. We calculate the interaction potential of a single ion next to a dielectric boundary as the sum of the hydration energy and the image potential, $U(z) = U_h(z) + U_i(z) - U_b$.

In Fig. 2.14 we plot the calculated energy as a function of z for (d) a hydrophilic surface and (e) a hydrophobic surface, for a small and a large ion. For the small ion, the cavity radius $\lambda_c = 0.15$ nm and the dielectric radius $\lambda_d = 0.25$ nm, and for the large ion $\lambda_c = 0.2$ nm and $\lambda_d = 0.3$ nm. We choose the dielectric radii larger than the cavity radii, reflecting the fact that radii inferred from the solvation free energy via the Born energy U_b are larger than cavity radii measured with diffraction methods [118]. It also conforms to our result that the dielectric dividing surface is displaced toward the water phase compared to the Gibbs dividing surface at hydrophilic surfaces. The curves clearly reflect the well-known positive correlation between ion size and adsorption onto the surface, meaning that larger ions show a larger surface propensity compared to smaller ions. Interestingly, this simple model already shows a striking difference between hydrophilic and hydrophobic surfaces, which has recently been found in simulations as well [122]. Because $z^{GDS} > z_\perp^{DDS}$ at the hydrophobic surface, the influence of the attractive hydration potential is much more pronounced than at the hydrophilic surface. For ions of $\lambda_c = 0.2$ nm, the hydration potential at the hydrophobic surface even dominates the

interaction for $0.09 < z < 0.26$ nm, which means that large ions adsorb onto hydrophobic surfaces, but not onto hydrophilic surfaces. For distances larger than ~ 0.3 nm from the interface all potentials resemble the exponential function used previously for $\mu(z)$.

2.5 Summary & Conclusions

We have established the theoretical framework for calculating the dielectric response tensor of water at an interface from molecular fluctuations and from an applied external field. Whereas the parallel response can be calculated from the dipole moment only and roughly follows the density profile, the perpendicular response exhibits several singularities that can be captured properly only when higher-order multipole moments are taken into account. For the perpendicular dielectric response, the linear response regime extends to an external field strength of at least $D_\perp/\varepsilon_0 \simeq 2$ V/nm, after which the response at the hydrophobic interface becomes non-linear. Because on timescales larger than ~ 10 ns, dielectric breakdown in real water occurs at external field strengths one order of magnitude lower, the non-linear response of the non-polarizable, non-ionizable water model that we use in our simulations is not expected to play a role in the dielectric response of real water. Including the dielectric profile in a mean-field description of ion distributions at a charged interface, we find that the experimental double-layer capacitance can be well reproduced. In particular, this shows that the Stern layer is predominantly caused by the dielectric interfacial features of water itself. Additionally accounting for the repulsive ion-substrate interaction – corresponding to steric exclusion of ions from the direct proximity of the wall – further improves the agreement with experimental data, but these direct ion-surface interactions are not decisive for the features seen in the experimental capacitance data. We quantify the difference between the dielectric response at hydrophilic and hydrophobic surfaces in terms of a single length scale that we call the dielectric dividing surface. Using this length scale, the similarity that is found experimentally between the double-layer capacitance at both surface types can be rationalized very simply: although a pronounced depletion layer exists at the hydrophobic interface, and therefore less water is available than at the hydrophilic interface, the dielectric dividing surface position is very similar at both surface types, measured with respect to the top layer of heavy substrate atoms. In other words, water at the hydrophobic surface is a "better dielectric" than at the hydrophilic surface. From the same mean-field description, we find that the effect of the dielectric profile is to decrease the disjoining pressure between two charged plates. Dielectric interface effects therefore cannot explain the universally observed hydration repulsion between polar surfaces directly. Finally, a simple model for the adsorption of spherical ions at interfaces that distinguishes between dielectric and depletion effects, both at the planar interfaces and around the ions, reveals the characteristic difference between adsorption at hydrophilic and hydrophobic surfaces. In particular, it predicts the adsorption of large ions onto hydrophobic surfaces, but not onto hydrophilic surfaces. In future research, the effect of ions and finite surface separation on the dielectric profile and the consequences of the full dielectric profile on the ionic free energy need to be addressed in order to understand the interaction of charged and neutral surfaces in full detail.

Chapter 3

Hydrodynamic Slip and its Effect on Electrokinetic Flow

In this chapter, we explore the effect of the hydrodynamic boundary condition on fluid flow through small channels. In particular, we study water flow through carbon nanotubes and rectangular silica nanochannels using continuum theory, including hydrodynamic slip through the Navier boundary condition. We also study the effect of the hydrodynamic boundary condition on the electro-osmotic motion of air bubbles and the effect of compressibility and density variation on the flow profile perpendicular to a solid surface. The material in this chapter has been published in Refs. [v] and [vii].

3.1 Introduction

For large-scale fluid flow along a solid boundary, it is well-established that the velocity profile can be calculated using the so-called no-slip boundary condition, *i.e.* the condition that the fluid velocity relative to the boundary vanishes at the boundary. At small length scales, however, the hydrodynamic boundary condition for tangential flow along solid surfaces typically differs from the no-slip boundary condition, which is important for fluid flow through small channels [123]. The microscopic origin of the slipping behavior is still unclear. The extent of slippage depends on charge density [124] and roughness [74] of the solid surface, as well as pressure, impurities and dissolved gas in the liquid phase [123]. At smooth, uncharged hydrophobic surfaces, water slippage increases strongly as a function of the solid-liquid contact angle, indicating that hydrophobic surfaces exhibit more slip than hydrophilic surfaces [74, 123]. In addition, the liquid viscosity at the interface is not spatially constant. The viscosity variation is mainly caused by the varying water density and the changing hydrogen bond structure at the interface.

The most common way to describe tangential slip at a solid surface is by imposing proportionality between the rate of strain and the tangential velocity $\boldsymbol{u}_{\parallel}$ at the surface,

$$-b\,\hat{\boldsymbol{n}}\cdot\left(\nabla\boldsymbol{u}+(\nabla\boldsymbol{u})^{T}\right)=\boldsymbol{u}_{\parallel}, \tag{3.1}$$

with b being the slip length, $\boldsymbol{u}$ being the velocity and $\hat{\boldsymbol{n}}$ being the unit vector normal to the interface, pointing into the solid. Eq. 3.1, which is referred to as the Navier boundary

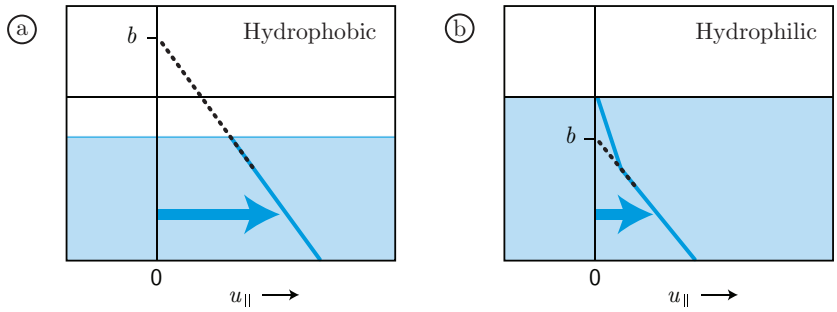

Figure 3.1: *Sketch of the tangential velocity profile $u_{\parallel}$ (blue lines) as a function of the coordinate perpendicular to the surface in a Couette shearing experiment. The slip length b corresponds to the distance where the linear extrapolation of the bulk velocity profile reaches zero. Two surface types are shown:* (a) *a hydrophobic surface, with depletion layer and positive slip length b and* (b) *a hydrophilic surface, with enhanced interfacial viscosity and negative b.*

condition, describes the combined effects of the varying viscosity profile and molecular slip of the first few layers of water molecules along the wall within a continuum model. The equation does not hold for the components of the fluid velocity perpendicular to the solid surface, to which we will come back below.

Two fundamentally different scenarios occur in nature. At hydrophobic surfaces, the solid and the fluid are separated by a depletion gap, which decreases friction and gives rise to a positive slip length [37–39], see Fig. 3.1 (a). The slip length depends on the width of the depletion gap to the fourth power [74]. For water in carbon nanotubes, the depletion gap is particularly large, and slip lengths of ~ 50 μm are reported [42]. Their large slip length indicates that water moves almost frictionless through carbon nanotubes, making them particularly suited to be used as channels in nanofluidic applications. The water viscosity appears to be constant up to the depletion gap [74]. At hydrophilic surfaces, on the other hand, no depletion gap exists and the viscosity in the first few water layers at the wall is higher than in bulk [74, 125]. The flow profile far away from the interface can be modeled using Eq. 3.1 with a negative slip length b, corresponding to the width of a stagnant layer of fluid sticking to the surface in a Couette shear flow experiment, see Fig. 3.1 (b). The position at the boundary between the effectively stagnant layer and the mobile fluid is generally referred as the shear plane. A stagnant layer hinders flow through small capillaries, whereas a positive slip length greatly enhances flow rates. In both pressure-driven and electrokinetic flows, these different hydrodynamic boundary conditions drastically affect the energy conversion efficiency. In Sec. 3.2, we calculate the energy dissipation in pressure-driven flow and the energy conversion efficiency in electrokinetic flow as a function of the slip length. We show that the energy conversion efficiency in hydrophilic silica channels is significantly reduced because of the stagnant layer, which is estimated to be ~ 3Å wide. In carbon nanotubes, on the other hand, the electrokinetic energy conversion efficiency is predicted to reach over 90%.

At the air-water interface, the viscosity on the gas side of the shear plane practically vanishes. When no heavy molecules are located in the gas phase, no momentum can be transferred across the shear plane and the rate of strain tensor vanishes, corresponding to the limit $b \to \infty$. Depending on the viscosity profile across the interface, however, the water density on the gas side of the shear plane may be non-zero, leaving the possibility

of a finite slip length open. In Sec. 3.4, we calculate the electrophoretic mobility of an air bubble as a function of the position of the shear plane for different values of the slip length, using a charge density profile that originates from charge transfer across the hydrogen bonds between water molecules [126].

Contrary to the fluid velocity tangential to the surface, the fluid velocity perpendicular to the surface strictly meets the no-slip boundary condition at impermeable surfaces, which means that the perpendicular fluid velocity at an immobilized surface equals zero,

$$\boldsymbol{u} \cdot \hat{\boldsymbol{n}} = 0. \tag{3.2}$$

In this case, the vanishing flow velocity is enforced by the condition that the water mass cannot penetrate the solid surface. In contrast, a published molecular dynamics study of water flow in carbon nanotubes suggests that the flow perpendicular to the surface can be non-zero, which is speculated to be related to the interfacial structure and the microscopic compressibility of water [62]. In Sec. 3.5, we refute these suggestions and show that the no-slip boundary condition holds rigidly for the perpendicular component of the fluid velocity, also for compressible fluids of spatially varying density.

3.2 Pumping & Energy Conversion

3.2.1 Dissipation in Pressure-Driven Flows

Conservation of momentum for a fluid flowing with space-dependent and time-dependent velocity $\boldsymbol{u}(\boldsymbol{x}, t)$ is expressed by the Navier-Stokes equation, which reads

$$\varrho \frac{\mathrm{d}\boldsymbol{u}}{\mathrm{d}t} = \nabla \cdot \mathsf{P} + \boldsymbol{F} \quad \text{with} \quad \frac{\mathrm{d}}{\mathrm{d}t} = \frac{\partial}{\partial t} + \boldsymbol{u} \cdot \nabla, \tag{3.3}$$

with $\boldsymbol{F}$ being an external force. We assume the fluid to be incompressible, leaving the mass density ϱ constant. For fluids of spherically symmetric constituents, the stress tensor P in Eq. 3.3 is given by

$$\mathsf{P} = -p\mathsf{U} + \Pi \quad \text{with} \quad \Pi_{ij} = \eta \left(\nabla_j u_i + \nabla_i u_j \right). \tag{3.4}$$

The hydrostatic pressure is denoted p, U is the unit tensor and η is the viscosity. The balance equation for the kinetic energy contained in a flowing liquid follows from a scalar product of the Navier-Stokes equation with the velocity, which in absence of external forces gives [127]

$$\varrho \frac{\mathrm{d}}{\mathrm{d}t} \frac{\boldsymbol{u}^2}{2} = \nabla \cdot (\mathsf{P} \cdot \boldsymbol{u}) - \mathsf{P} : (\nabla \boldsymbol{u}). \tag{3.5}$$

In steady state $\partial \boldsymbol{u}/\partial t = 0$ and Eq. 3.5 reduces to

$$0 = \nabla \cdot \left(-{}^1\!/_2 \, \varrho \boldsymbol{u}^2 \boldsymbol{u} + \mathsf{P} \cdot \boldsymbol{u} \right) - \mathsf{P} : (\nabla \boldsymbol{u}), \tag{3.6}$$

where the first term on the right-hand side represents the convective energy flow, equal to ${}^1\!/_2 \, \varrho \left(\boldsymbol{u} \cdot \nabla \right) \boldsymbol{u}^2 = {}^1\!/_2 \, \varrho \nabla \cdot \left(\boldsymbol{u}^2 \boldsymbol{u} \right)$, which needs not be zero in steady state. Integration over a volume $\mathcal{V}$ and application of Gauss's theorem yields

$$0 = \int_{\partial \mathcal{V}} \hat{\boldsymbol{n}} \cdot \left(-\frac{\varrho \boldsymbol{u}^2 \boldsymbol{u}}{2} + \mathsf{P} \cdot \boldsymbol{u} \right) \mathrm{d}\mathcal{A} - \int_{\mathcal{V}} \mathsf{P} : (\nabla \boldsymbol{u}) \, \mathrm{d}\mathcal{V}. \tag{3.7}$$

Using Einstein's summation convention, we write the integral component-wise and insert Eq. 3.4,

$$\begin{aligned} 0 = &\int_{\partial\mathcal{V}} \hat{n}_j \left[-\frac{\varrho u_i^2 u_j}{2} - p u_j + \eta \left(\nabla_j u_i + \nabla_i u_j \right) u_i \right] \mathrm{d}\mathcal{A} \\ &- \int_{\mathcal{V}} \eta \left(\nabla_j u_i + \nabla_i u_j \right) \nabla_j u_i \, \mathrm{d}\mathcal{V}, \end{aligned} \tag{3.8}$$

where we used $\mathsf{P} \cdot \boldsymbol{u} = -p\delta_{ij}u_i + \eta \left(\nabla_j u_i + \nabla_i u_j \right) u_i$ and $\mathsf{P} : (\nabla \boldsymbol{u}) = \mathsf{P}_{ij} \nabla_j u_i$ and the incompressibility of the fluid, $\nabla_i u_i = 0$. The surface of the volume $\partial\mathcal{V}$ consists of three parts: an inlet, an outlet and a wall. At impenetrable walls $\hat{n}_j u_j = 0$. For flow through a translationally invariant channel also the integrals over the inlet and outlet of the first term in the surface integral vanish. The second term in the surface integral represents the input power $Q\Delta p$, with the volume flux

$$Q = \int_{\Omega} \hat{n}_j u_j \, \mathrm{d}\mathcal{A}, \tag{3.9}$$

where Ω is the cross section of the channel and Δp is the static pressure difference between the inlet and outlet. The remaining term in the surface integral in Eq. 3.8 represents the power dissipated by friction at the walls and depends on the extent of slip. The volume integral represents the power dissipated within the fluid because of velocity gradients. In our continuum description, we take the viscosity as a constant and introduce a slip length b as a boundary condition,

$$-\hat{n}_j b \nabla_j u_i|_{\pm d/2} = u_i|_{\pm d/2}, \tag{3.10}$$

with d the height of the channel. For single-directional fluid flow, as appropriate for an incompressible fluid flowing through a translationally invariant channel, the balance equation becomes

$$Q\Delta p = -\eta \int_{\partial\mathcal{V}} \frac{u_i^2}{b} \, \mathrm{d}\mathcal{A} - \eta \int_{\mathcal{V}} \left(\nabla_j u_i \right)^2 \mathrm{d}\mathcal{V}, \tag{3.11}$$

where the right-hand side equates to the dissipated power $P_{diss.}$.

We now calculate the dissipation as a function of the slip length b for a given volume flux Q. Ignoring edge effects, a pressure-driven fluid flow in a slit-like rectangular channel forms a Poiseuille flow profile (calculated from Eq. 3.3 with Eq. 3.10),

$$u_i = -\frac{\nabla_i p}{8\eta} \left[d^2 + 4bd - 4x_j^2 \right], \tag{3.12}$$

with u_i the fluid velocity lengthways, x_j the spatial coordinate along the height of the channel and $\nabla_i p = \Delta p / l$ the pressure gradient along the length of the channel l. For a given volume flux Q, the dissipation from Eq. 3.11 in a channel of width w becomes

$$P_{diss.} = \frac{12\, Q^2 \eta l}{w \left(d^3 + 6d^2 b \right)}, \tag{3.13}$$

from which it can be seen that increasing the slip length greatly reduces the power required to achieve a flux Q when b becomes of the order of d.

A pressure difference across a cylindrical channel, such as a carbon nanotube, produces a Hagen-Poiseuille flow profile. At the wall of the tube of diameter d we use the boundary

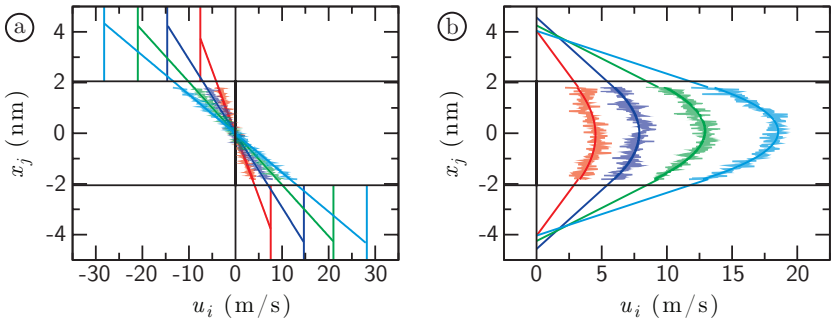

Figure 3.2: *Tangential flow profile u_i as a function of the coordinate perpendicular to the surface x_j in* (a) *a Couette shearing simulation and* (b) *a Poiseuille flow simulation. The Couette flow is driven by the forces on the diamond, leading to fixed surface velocities of: $u_0 = 6$ (red), $u_0 = 17$ (blue), $u_0 = 22$ (green) and $u_0 = 28$ (cyan) m/s. The Poiseuille flow is driven by a pressure gradient of $\nabla_i p = 0.5$ (red), $\nabla_i p = 1.0$ (blue), $\nabla_i p = 1.5$ (green) and $\nabla_i p = 2.0 \times 10^{15}$ Pa/m. The curves have been fitted by* (a) *a linear profile and* (b) *a quadratic profile.*

condition given in Eq. 3.10 restricted to the wall at $+d/2$. Inside a tube of diameter $d \ll l$ the flow profile is given by

$$u_i = -\frac{\nabla_i p}{16\eta}\left[d^2 + 4bd - 4x_j^2\right]. \tag{3.14}$$

The dissipation for fixed Q equals

$$P_{diss.} = \frac{128\, Q^2 \eta l}{\pi\left(d^4 + 8bd^3\right)}. \tag{3.15}$$

In carbon nanotubes, the slip length b can be two orders of magnitude larger than in other hydrophobic channels and much larger than the diameter d [42], making the energy dissipation scale inversely linear with the slip length. The resulting massive reduction of the energy dissipation is a major advantage when using large arrays of parallel nanotubes for filtering or desalination.

Molecular dynamics simulations. We perform non-equilibrium molecular dynamics simulations of a rectangular water slab confined between two diamond surfaces, consisting of a double-FCC lattice of carbon atoms (GROMOS 96 force field: $\epsilon = 0.277$ kJ mol^{-1} and $\sigma = 0.358$ nm). The diamond has a contact angle of $\sim 111°$, as calculated from the virial tensor following Ref. [128]. We simulate a Couette shear flow by applying equal but opposite forces F_i to the two diamonds along the direction of the channel, which is denoted x_i. The flow profiles resulting from applied forces of $F_i = 23$ pN, $F_i = 47$ pN, $F_i = 70$ pN and $F_i = 93$ pN are shown in Fig. 3.2 (a). We simulate a Poiseuille flow by keeping the diamond fixed and applying a constant force to the water molecules. In Fig. 3.2 (b), we show the Poiseuille flow profiles resulting from force densities of $\nabla_i p = 0.5$ pN/nm^3, $\nabla_i p = 1.0$ pN/nm^3, $\nabla_i p = 1.5$ pN/nm^3 and $\nabla_i p = 2.0$ pN/nm^3. Lines have been fitted to the Couette flow profiles and quadratic functions to the Poiseuille flows, yielding viscosity and slip length for each curve. The slip length following from the Couette flow equals $b = 2.1 \pm 0.2$ nm and the slip length following from the Poiseuille flow equals $b = 1.9 \pm 0.2$ nm, showing no significant difference. There is also no significant difference between the results of the simulations at different driving forces. In conclusion, the

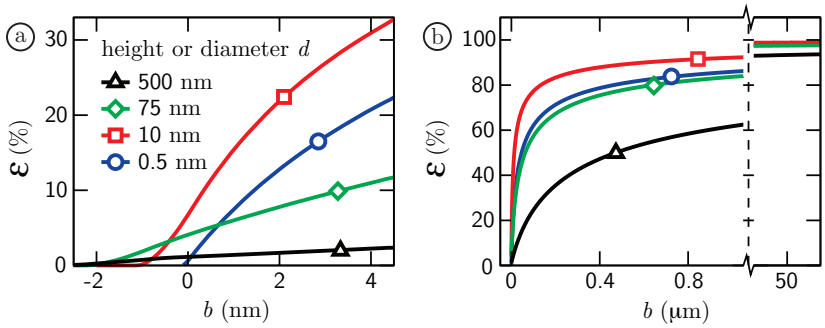

Figure 3.3: *Efficiency $\mathcal{E}$ of electrokinetic energy conversion as a function of slip length b in* (a) *a rectangular channel and* (b) *a cylindrical channel, calculated from Eq. 3.21. The electrolyte used is 0.1 mM monovalent ions with the electrophoretic mobilities of* K^+ *and* Cl^-*. For both geometries, the surface potential is fixed at −240 mV. The corresponding surface charge density equals $\sigma = -13\ mC/m^2$ in the $d = 0.5$ nm cylindrical channel, $\sigma = -24\ mC/m^2$ in the $d = 0.5$ nm rectangular channel and $\sigma \simeq -60\ mC/m^2$ for all other channels.*

slip length gives a consistent and reproducible measure of the hydrodynamic boundary condition at hydrophobic surfaces.

3.2.2 Electrokinetic Energy Conversion Efficiency

The calculation in Sec. 3.2.1 shows that a large slip length reduces the energy dissipation in pressure-driven flows. However, a hydrostatic pressure difference is sometimes difficult to generate on small scales. Therefore, electro-osmosis is the preferred mechanism to drive nano-scale pumps [4]. We consider an electro-osmotic pump consisting of a slit-like or cylindrical channel with a fixed surface charge density or surface potential operated with a solution of monovalent ions. Under the influence of an electric field, the ions move along the surface and drag the fluid along, driving a hydrostatic load impedance. The load impedance connected to the channel is the hydrostatic equivalent of an electrical load resistance connected to an electrical power source. Whereas efficiency is not crucial for microscopic applications, it becomes important when nanofluidic devices are used in parallel arrays that are designed to reach macroscopic sizes. In this section we calculate the efficiency of the energy conversion from electrical power to a hydrostatic pressure difference as a function of the slip length. Because of the inhomogeneity of the volume and current flow densities, the standard flow densities and Onsager coefficients are integrated over the cross section Ω of the channel [127].

Apart from the pressure gradient ∇p discussed in Sec. 3.2.1, the electrolyte is subject to a voltage gradient $\nabla\psi$, leading to an electro-osmotic flow. The electro-osmotic flow velocity $u_i^{(\psi)}$ is calculated from the Navier-Stokes equation (Eq. 3.3) with the external forces

$$F_i = \varepsilon\varepsilon_0 \nabla_j^2 \psi \nabla_i \psi \quad \text{and} \quad F_i = \varepsilon\varepsilon_0 \frac{1}{x_j} \nabla_j x_j \nabla_j \psi \nabla_i \psi, \tag{3.16}$$

in rectangular and cylindrical coordinates respectively. For the electrostatics, we impose a constant surface charge density σ as a boundary condition, which gives

$$\hat{n}_j\, \varepsilon\varepsilon_0 \nabla_j \psi = \sigma. \tag{3.17}$$

Solving Eq. 3.3 with the forces of Eq. 3.16 and the boundary conditions Eqs. 3.10 and 3.17 gives

$$u_i^{(\psi)}(x_j) = \frac{\nabla_i \psi}{\eta} \left(\varepsilon\varepsilon_0 \left[\psi(d/2) - \psi(x_j)\right] + b\sigma\right), \tag{3.18}$$

for both the rectangular and the cylindrical geometry.

Linear response theory. In the linear response regime, the electrical current I and fluid volume flux Q are related to the pressure gradient ∇p and the voltage gradient $\nabla\psi$ via

$$\begin{bmatrix} Q \\ I \end{bmatrix} = \begin{bmatrix} \Lambda_{11} & \Lambda_{12} \\ \Lambda_{21} & \Lambda_{22} \end{bmatrix} \begin{bmatrix} -\nabla p \\ -\nabla\psi \end{bmatrix}. \tag{3.19}$$

The hydrostatic output power per unit length of the channel equals $P_{out} = -Q \cdot \nabla p$, and the electrical input power equals $P_{in} = -I \cdot \nabla\psi$. For electrokinetic power generation by pressure-driven flow, input and output power are defined the other way around, but the efficiency is calculated in the same way. The electrokinetic energy conversion efficiency is given by the ratio $\mathcal{E} = P_{out}/P_{in}$, which can be expressed in terms of the electrokinetic response functions via Eq. 3.19. In the channel, the fluid velocity and electrostatic potential (apart from the constant voltage gradient driving the pump) depend only on the coordinate perpendicular to the channel wall, throughout the following calculation denoted x_j. The velocity, the electric current and the pressure gradient are only non-zero in the direction along the channel wall, denoted x_i. The Onsager coefficients can be expressed as

$$\begin{aligned}
\Lambda_{11} &= -\int_\Omega \frac{u_i^{(p)}}{\nabla_i p}\,\mathrm{d}\mathcal{A} \\
\Lambda_{21} &= -e\int_\Omega \left[n_+(x_j) - n_-(x_j)\right]\frac{u_i^{(p)}}{\nabla_i p}\,\mathrm{d}\mathcal{A} \\
\Lambda_{12} &= -\int_\Omega \frac{u_i^{(\psi)}}{\nabla_i \psi}\,\mathrm{d}\mathcal{A} \\
\Lambda_{22} &= e\int_\Omega \left[\nu_+ n_+(x_j) + \nu_- n_-(x_j)\right] - \left[n_+(x_j) - n_-(x_j)\right]\frac{u_i^{(\psi)}}{\nabla_i \psi}\,\mathrm{d}\mathcal{A},
\end{aligned} \tag{3.20}$$

where the monovalent ions have electrophoretic mobilities $\nu_\pm$ and number densities $n_\pm = n_0 \exp(\mp e\psi/k_\mathrm{B}T)$ with n_0 the bulk density and $k_\mathrm{B}T$ the thermal energy. The electrostatic potential $\psi(x_j)$ is calculated numerically from the Poisson-Boltzmann equation, which holds sufficiently well on small scales [124]. The pressure-driven flow velocity $u_i^{(p)}(x_j)$ is given in Eqs. 3.12 and 3.14 for the rectangular and cylindrical geometries respectively, and the electro-osmotic flow velocity $u_i^{(\psi)}(x_j)$ is given in Eq. 3.18. The surface of a carbon nanotube is uncharged, but a finite surface potential can be achieved for nanotubes by application of an external potential. Surface potentials also arise naturally due to unequal surface adsorption of cations and anions. Note that in an experimental setup the driving electric field will be at least partially screened by electron transport through the nanotube, which will reduce the electric fields strength inside the nanotube. The pressure gradient generated is linearly related to the volume flux via the hydrostatic load impedance Z_L, $Q = \nabla_i p/Z_\mathrm{L}$. The efficiency is maximized for a specific value of $Z_\mathrm{L}\Lambda_{11}$, which is the hydrostatic load impedance divided by the hydrostatic channel impedance

Λ_{11}^{-1}. The value of the maximum efficiency $\mathcal{E}$ has a very simple form in terms of the variable $\alpha = \Lambda_{12}^2/\Lambda_{11}\Lambda_{22}$ [129]:

$$\mathcal{E} = \frac{\alpha}{2 + 2\sqrt{1-\alpha} - \alpha}. \tag{3.21}$$

Using the no-slip boundary condition, the predicted maximum efficiency is only 7%, whereas the measured efficiency in a silicon oxide channel of $d = 75$ nm reaches no more than 3% [130]. To investigate the effect of slip, we use the hydrodynamic boundary condition of Eq. 3.10. The efficiency from Eq. 3.21 is shown in Fig. 3.3 as a function of slip length for different channel dimensions. We use the ion mobilities of K^+ and Cl^- and a bulk concentration of 0.1 mM, giving a Debye screening length of 30 nm. Clearly, the efficiency increases drastically with increasing slip length. The variation of the efficiency with respect to the channel diameter d is non-monotonic and different for different values of the slip length. For a slip length of ~ 2 nm, which is a reasonable number for hydrophobic surfaces [74], the efficiency in the 10 nm high rectangular channel reaches $\sim 20\%$. In extension to the work of Ref. [131] we plot the efficiency for negative slip lengths. The measured efficiency of 3% in a 75 nm high channel and 1% in a 490 nm high channel [130] with a surface charge density of -60 mC/m^2, which is the measured surface charge density of silicon oxide [132], is consistent with a slip length of $b = -0.3$ nm, corresponding to one static molecular layer, in good agreement with predictions by Ref. [74] for an OH-covered surface.

In Fig. 3.3 (b), the efficiency is calculated for a cylindrical channel. The increase in efficiency is similar to the planar case, but in carbon nanotubes the slip length can be as much as ~ 50 μm [42]. In all nanotubes considered, the efficiency for slip lengths of that order is over 90%.

3.3 Onsager Reciprocal Relation

The electrokinetic phenomena described in Eq. 3.19 are an example of coupled irreversible processes for which the Onsager reciprocal relations between the thermodynamic fluxes and forces should hold [127, 133, 134]. The Onsager relation connects the electro-osmotic fluid flow in response to an electric field directly to the electric current in response to a pressure gradient, $\Lambda_{12} = \Lambda_{21}$, first proven by Saxén using the no-slip boundary condition [135]. Using the expressions of Eq. 3.20, we will proof this identity explicitly using the boundary condition of Eq. 3.10.

Rectangular geometry. Using the Poisson equation, the streaming conductance Λ_{21} is expressed as

$$\Lambda_{21} = \varepsilon\varepsilon_0 \int_\Omega \nabla_j^2 \psi \frac{u_i^{(p)}}{\nabla_i p}\, \mathrm{d}\mathcal{A}. \tag{3.22}$$

A double partial integration of Eq. 3.22 yields

$$\Lambda_{21} = \varepsilon\varepsilon_0 \int_{\partial\Omega} \nabla_j \psi \frac{u_i^{(p)}}{\nabla_i p}\, \hat{n}_j \mathrm{d}\Gamma - \varepsilon\varepsilon_0 \int_{\partial\Omega} \psi \frac{\nabla_j u_i^{(p)}}{\nabla_i p}\, \hat{n}_j \mathrm{d}\Gamma + \varepsilon\varepsilon_0 \int_\Omega \psi \frac{\nabla_j^2 u_i^{(p)}}{\nabla_i p}\, \mathrm{d}\mathcal{A}, \tag{3.23}$$

with Γ the path along the edge of the channel cross-section $\partial\Omega$, located at $x_j = \pm d/2$. Inserting the pressure-driven velocity of Eq. 3.12 and the electrostatic boundary condition

of Eq. 3.17 and integrating the first two terms of Eq. 3.23 gives the expression

$$\Lambda_{21} = -w\sigma \frac{bd}{\eta} - \varepsilon\varepsilon_0 w\psi\left(d/2\right)\frac{d}{\eta} + \varepsilon\varepsilon_0 \int_\Omega \frac{\psi}{\eta}\,\mathrm{d}\mathcal{A}, \tag{3.24}$$

with w the width of the channel. To prove the Onsager relation, we insert the electro-osmotic velocity of Eq. 3.18 into the expression for the electro-osmotic coefficient Λ_{12} given in Eq. 3.20, yielding

$$\Lambda_{12} = -\frac{1}{\eta}\int_\Omega \varepsilon\varepsilon_0\left[\psi\left(d/2\right) - \psi\left(x_j\right)\right] + b\sigma\,\mathrm{d}\mathcal{A}. \tag{3.25}$$

Integration of Eq. 3.25 immediately shows $\Lambda_{12} = \Lambda_{21}$.

Cylindrical geometry. The streaming conductance in cylindrical coordinates is given by

$$\Lambda_{21} = \varepsilon\varepsilon_0 \int_0^{d/2} \frac{1}{x_j}\nabla_j x_j \nabla_j \psi \frac{u_i^{(p)}}{\nabla_i p}\, 2\pi x_j\,\mathrm{d}x_j, \tag{3.26}$$

where we perform the integral in one dimension. Double integration by parts yields

$$\begin{aligned}\Lambda_{21} = {} & 2\pi\varepsilon\varepsilon_0\left[x_j\nabla_j\psi\,\frac{u_i^{(p)}}{\nabla_i p}\right]_0^{d/2} - 2\pi\varepsilon\varepsilon_0\left[\psi x_j \nabla_j \frac{u_i^{(p)}}{\nabla_i p}\right]_0^{d/2} \\ & + 2\pi\varepsilon\varepsilon_0\int_0^{d/2}\psi\nabla_j x_j\nabla_j\frac{u_i^{(p)}}{\nabla_i p}\,\mathrm{d}x_j.\end{aligned} \tag{3.27}$$

Using the electrostatic boundary condition of Eq. 3.17 and the pressure-driven flow velocity of Eq. 3.14 we arrive at

$$\Lambda_{21} = -\frac{\pi\sigma b d^2}{4\eta} - \varepsilon\varepsilon_0\psi\left(d/2\right)\frac{\pi d^2}{4\eta} + \varepsilon\varepsilon_0\int_0^{d/2}\psi\,\frac{2\pi x_j}{\eta}\,\mathrm{d}x_j. \tag{3.28}$$

The electro-osmotic coefficient Λ_{12} is found by integration of the electro-osmotic flow velocity in cylindrical coordinates

$$\Lambda_{12} = -\frac{1}{\eta}\int_0^{d/2}\left(\varepsilon\varepsilon_0\left[\psi\left(d/2\right) - \psi\left(x_j\right)\right] + b\sigma\right)\,2\pi x_j\,\mathrm{d}x_j. \tag{3.29}$$

Clearly, integration of Eq. 3.29 yields an expression identical to the one in Eq. 3.28.

Practically, the Onsager relation $\Lambda_{12} = \Lambda_{21}$ means that when a system has a non-zero electro-osmotic coefficient, *i.e.* it moves in response to an electric field, it must also have a non-zero streaming conductance, *i.e.* it generates an electric current in response to an applied pressure gradient. Because no steady-state electric current can be generated by applying a pressure gradient, a system without mobile charges should not exhibit electro-osmotic flow. Note, however, that rotational motion of dipolar molecules is not taken into account in the current analysis.

3.4 The ζ-Potential of Air Bubbles

Across the air-water interface, the viscosity drops from the water bulk value to the value in air, which is close to zero. Calculating the ζ-potential of an air bubble requires knowledge of the viscosity profile across its interface. The viscosity in the interfacial region is, in general, different from the bulk water viscosity. We consider a planar air-water interface with x_j the coordinate perpendicular to the surface, which yields a valid description of the electro-osmotic mobility when the radius of the bubble greatly exceeds the typical length scale of the charge density profile. When we approximate the viscosity profile by a step profile $\eta(x_j) = \eta_w(1 - \theta(x_j - x_j^0))$, which was found to be accurate for water at a hydrophobic surface [74], the charges in the (effective) vapor phase cannot transfer any momentum to the air bubble. Therefore, we take the coupling to the charges in the vapor phase into account by a surface friction coefficient, quantified by the slip length, b, equal to the viscosity divided by the friction coefficient. The Stokes equation reads

$$\nabla_j \eta(x_j) \nabla_j u_i(x_j) = -E_i \rho(x_j), \tag{3.30}$$

with x_i being the coordinate parallel to the surface, $\eta(x_j)$ being the viscosity, $u_i(x_j)$ being the velocity parallel to the surface in response to an applied electric field E_i and $\rho(x_j)$ the density of free charges. Integrating once with respect to x_j and using the boundary condition that $\nabla u_i(x_j)$ and the integral over all charges vanish in the bulk fluid leads to

$$\eta(x_j) \nabla_j u_i(x_j) = -E_i F_j(x_j), \tag{3.31}$$

with $\nabla \cdot \boldsymbol{F}(x_j) = \rho(x_j)$. Integrating Eq. 3.31 from a position x_j^w in the bulk water to x_j^0, where the viscosity vanishes, gives

$$u_i\left(x_j^0\right) - u_i\left(x_j^w\right) = \frac{E_i}{\eta_w} \int_{x_j^w}^{x_j^0} \rho(x_j) \left(x_j - x_j^0\right) \mathrm{d}x_j. \tag{3.32}$$

Now we apply the Navier boundary condition at $x_j = x_j^0$,

$$u_i\left(x_j^0\right) = -b \nabla_j u_i(x_j)\,|_{x_j^0}, \tag{3.33}$$

leading to

$$-u_i\left(x_j^w\right) = \frac{E_i}{\eta_w} \int_{x_j^w}^{x_j^0} \rho(x_j) \left(x_j - x_j^0 - b\right) \mathrm{d}x_j. \tag{3.34}$$

The ζ-potential is defined as

$$\zeta = -\frac{\eta_w u_i(x_j^w)}{\varepsilon_0 \varepsilon E_i}, \tag{3.35}$$

with ε_0 the permittivity of vacuum and ε the relative permittivity of water, for which we take $\varepsilon = 80$. Combining Eqs. 3.34 and 3.35 gives [67]

$$\zeta = \frac{1}{\varepsilon_0 \varepsilon} \int_{x_j^w}^{x_j^0} \rho(x_j) \left(x_j - x_j^0 - b\right) \mathrm{d}x_j. \tag{3.36}$$

Eq. 3.36 shows that the ζ-potential essentially equals the first moment of the charge distribution.

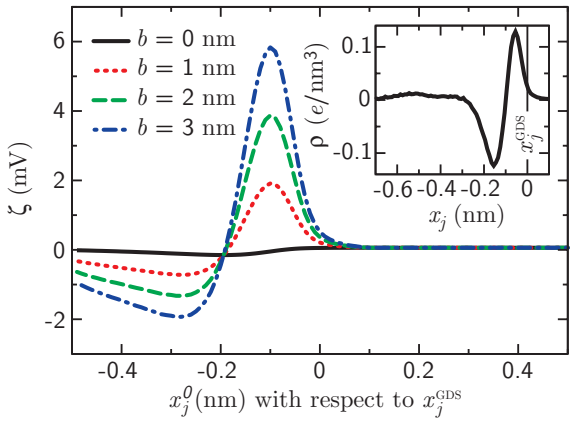

Figure 3.4: *ζ-potential calculated from Eq. 3.36 as a function of the shear surface position x_j^0, using the instantaneous charge density profile. The position x_j^0 is defined with respect to the Gibbs dividing surface x_j^{GDS}. In the inset, we show the instantaneous charge density profile caused by the charge transfer.*

Usually, the charge density $\rho(x_j)$ originates from a non-zero ion concentration. Nevertheless, at a pure air-water interface there may be a contribution to the free charge density stemming from the hydrogen bond network. Due to the ordering and orientation of water molecules at aqueous interfaces, the hydrogen bond network is anisotropic [136]. The top water layer has a small excess of hydrogen bond acceptors, whereas the second layer has an excess of hydrogen bond donors. If a small charge transfer is associated with each hydrogen bond, the asymmetry at the surface leads to a non-zero free charge distribution. In Ref. [126], the charge density resulting from charge transfer is estimated using a combination of classical and *ab initio* molecular dynamics simulations. In the following, we use this charge density profile to calculate the electro-osmotic mobility of air bubbles in pure water.

In Fig. 3.4, we plot the ζ-potential of an air bubble calculated from Eq. 3.36 for different values of the effective slip length b, using the charge density profile $\rho(x_j)$ which is shown in the inset. The charge density profile is calculated with respect to the Gibbs dividing surface x_j^{GDS}, where x_j^{GDS} is determined separately at each time and lateral position (x_i, x_k) to avoid smoothing by lateral and temporal surface fluctuations [137]. The position x_j^0 of the effective shear surface is varied between a position in vacuum, corresponding to an interfacial region with bulk viscosity, and a position up to several atomic layers inside the fluid, where all water properties are expected to reach bulk values [136]. Simultaneously varying the slip length b, we cover all different interfacial viscous properties that may be expected based on simulations of water at hydrophobic surfaces [74]. Clearly, the ζ-potential depends strongly on the value of b. If the transfer charge density is non-zero at the position of the effective shear surface x_j^0, then the bubble surface will not be stress-free because of the hydrogen bonds spanning across x_j^0. In addition, every air bubble has a non-zero slip length due to its curvature [124]. The effective slip length b is given by

$$\frac{1}{b} = \frac{1}{b_0} + \frac{1}{a}, \tag{3.37}$$

where b_0 is the "intrinsic" slip length that is controlled by hydrogen bonds across the dividing surface as well as friction due to interacting water molecules and charges in the

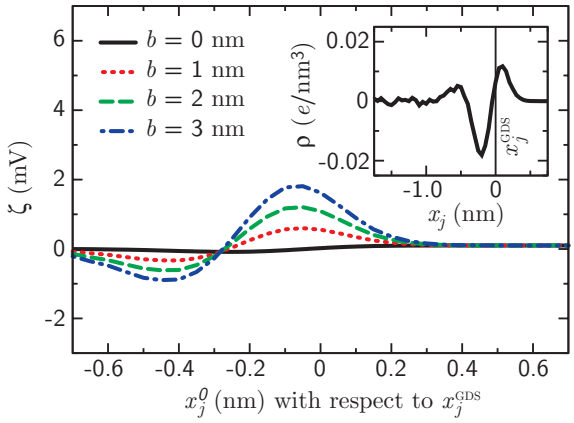

Figure 3.5: *ζ-potential calculated from Eq. 3.36 as a function of the shear surface position x_j^0. The position x_j^0 is defined with respect to the Gibbs dividing surface. In the inset, we show the laterally averaged charge density profile caused by the charge transfer.*

vapor and liquid phases, and a is the curvature of the bubble surface. Because of the large number of hydrogen bonds across the effective plane of shear, we expect b_0 to be small for $x_j^0 < 0.1$ nm. For $x_j^0 > 0.1$ nm, the water density is very small, and b_0 is expected to be large. For values of b of several nanometers, which we consider as an upper limit because this is the value for very hydrophobic surfaces, we find a ζ-potential of several millivolts, that is, about an order of magnitude smaller than the ζ-potential of ~ -35 mV measured for air bubbles in water [138]. Assuming that the transition from bulk-like to vapor-like hydrodynamic properties occurs effectively at one molecular layer beneath the surface, which is realistic in the view of the high self-diffusion constant of the top water layer found in molecular dynamics simulations [139, 140], the ζ-potential is negative. A negative peak is found at $x_j^0 = -0.28$ nm, that is, about one water layer below the surface, effectively leaving the air bubble with a net negative charge. However, the ζ-potential varies depending on the hydrodynamic properties of the interfacial region, and a positive peak is obtained at $x_j^0 = -0.10$ nm. In Fig. 3.5, we show the ζ-potential when the charge density profile is calculated with respect to the laterally averaged x_j^{GDS} ($\rho(x_j)$ is shown in the inset). Qualitatively, the graph shows the same features as Fig. 3.4, but the amplitude of the ζ-potential is lower because the charge profile is smoothed by lateral averaging.

In conclusion, the ζ-potential resulting from the charge transfer is small, even when finite slip between the charges in the water and vapor phase is taken into account. The sign of the ζ-potential can be positive or negative, depending on the nature of the viscosity profile. To improve the current model, the viscosity profile across the air-water interface needs to be calculated explicitly.

3.5 Radial Flow in Compressible Fluids

In Ref. [62], a non-zero radial velocity component is reported in a pressure-driven flow inside a (16, 16) carbon nanotube, see Fig. 3.6 (b), in stark contrast with continuum Poiseuille-flow predictions. The non-zero radial flow is claimed to be related to the inhomogeneous density profile. Let us analyze the effect of compressibility and a space-

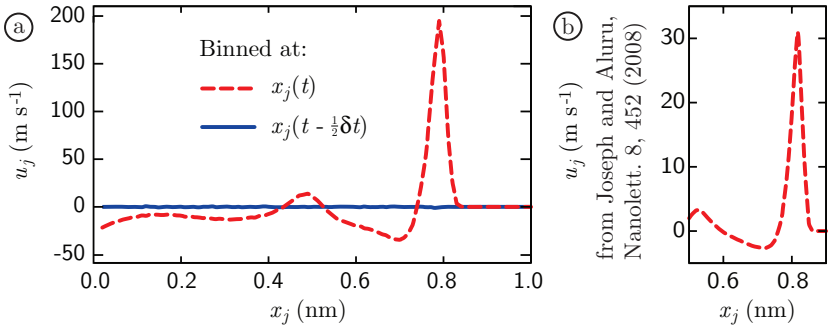

Figure 3.6: *Radial velocity inside a (16,16) carbon nanotube without reservoir.* (a) *Electro-osmotic velocity calculated with binning at t (dashed red line) and the correct binning at* $t - {}^1/_2\,\delta t$ *(solid blue line).* (b) *Graph taken from Ref. [62] showing a pressure-driven radial velocity in the same (16,16) carbon nanotube.*

dependent mass density $\varrho\,(\boldsymbol{x})$ on the radial velocity profile. The continuity equation in its most general form is given by

$$\frac{\partial \varrho}{\partial t} + \nabla \cdot (\varrho \boldsymbol{u}) = 0. \tag{3.38}$$

When the density $\varrho\,(x_j)$ and the velocity $\boldsymbol{u}\,(x_j)$ depend on the radial coordinate x_j, the radial component of Eq. 3.38 reduces in steady state to

$$u_j\,(x_j)\,\nabla_j \varrho\,(x_j) + \varrho\,(x_j)\,\frac{1}{x_j}\nabla_j\,(x_j u_j\,(x_j)) = 0. \tag{3.39}$$

Multiplying by x_j and integrating once over x_j yields

$$\int x_j u_j\,(x_j)\,\nabla_j \varrho\,(x_j)\,\mathrm{d}x_j + \int \varrho\,(x_j)\,\nabla_j\,(x_j u_j\,(x_j))\,\mathrm{d}x_j = c, \tag{3.40}$$

with c an integration constant. Integration by parts of the first term on the left-hand side gives

$$x_j u_j\,(x_j)\,\varrho\,(x_j) = c. \tag{3.41}$$

Eq. 3.41 fixes $u_j\,(x_j)$ as a function of $\varrho\,(x_j)$. When the density $\varrho\,(x_j)$ vanishes at the wall of the tube, the velocity should remain finite, showing that the only physical solution is $c = 0$ and therefore $u_j\,(x_j) = 0$, also for compressible fluids of variable density.

To find out why the simulations of Ref. [62] exhibit a non-zero radial flow profile, we calculate the radial velocity $u_j(x_j)$ in simulations of a $(16, 16)$ nanotube from radially binned water molecule positions $x_j(t)$ according to $u_j(x_j[t-\tau]) = (x_j[t] - x_j[t-\delta t])/\delta t$ with δt the integration time step. The correct positioning of the velocity requires choosing $\tau = {}^1/_2\,\delta t$, and in this case u_j vanishes, as shown as a solid line in Fig. 3.6 (a), in agreement with standard hydrodynamic theory. Incorrectly using $\tau = 0$ gives a spurious non-vanishing u_j profile (broken line), similar to profiles reported in Ref. [62]. The reason for this is that a water molecule that at time t happens to be close to the surface is, due to the impenetrability of the surface, likely to origin from a position further away from the surface at time $t - \delta t$.

3.6 Summary & Conclusions

We study the effect of a deviation from the no-slip boundary condition on the properties of pressure-driven and electrokinetic flow through rectangular nanochannels and carbon nanotubes, as well as the electrophoretic motion of gas bubbles. The extremely large slip length measured in carbon nanotubes greatly reduces the fluidic resistance to pressure-driven flow and at the same time enhances the efficiency of electrokinetic energy conversion. Experimental values of the electrokinetic energy conversion efficiency in hydrophilic silicon oxide channels can be modeled using a slip length of $b = -0.3$ nm, corresponding to one highly viscous layer of water molecules at the interface. In the direction perpendicular to the tube wall, the no-slip boundary condition holds rigidly, also for systems with spatially varying density. Using the standard Navier-Stokes equation, we explicitly prove the Onsager reciprocal relation for electrokinetic flow, namely that the electro-osmotic conductance and the streaming conductance are equal. From the equality we conclude that systems of spherically symmetric particles, as considered in this chapter, do not exhibit electro-osmotic flow in static electric fields if no mobile charges are present. Rotation of water molecules, which has not been taken into account so far, will be treated in detail in Chapter 4. Finally, we show that the mobile charge density resulting from charge transfer between water molecules does not contribute significantly to the electrophoretic mobility of air bubbles in water, regardless of the hydrodynamic boundary conditions.

Chapter 4

Electrokinetics at Aqueous Interfaces without Mobile Charges

We theoretically consider the possibility of using electric fields in aqueous channels of cylindrical and planar geometry to induce transport in the absence of mobile ionic charges. Using the Navier-Stokes equation, generalized to include the effects of water spinning, dipole orientation and relaxation, we show analytically that pumping of a dipolar liquid through an uncharged hydrophobic channel can be achieved by injecting torque into the liquid, based on the coupling between molecular spinning and fluid vorticity. Pumping is possible continuously, using rotating electric fields and suitably chosen interfacial boundary conditions, or transiently, by suddenly switching on a homogeneous electric field. A static electric field, however, does not induce a steady-state flow in channels, irrespective of the geometry. Using molecular dynamics (MD) simulations, we confirm that static fields do not lead to any pumping, in contrast to earlier publications. The origin of the pumping observed in MD simulations of carbon nanotubes and oil droplets in a static electric field is tracked down to an imprudent implementation of Lennard-Jones interaction truncation schemes. The work described in this chapter has been published in Refs. [iv], [vii], [ix] and [x].

4.1 Introduction

Efficient conversion of power from one form to another is nowadays a pressing issue. In fluidic applications, this mainly comes down to conversion between electrical and mechanical energy: the key elements of fluidic systems are pumps for converting electrical power into a hydrostatic pressure difference, and turbines or electro-osmotic power generators for the reverse process. The realization of the full potential of laboratory minimization depends crucially on the design and fabrication of these active fluidic components on the nano scale. In particular, pumps are of critical importance for the two principal functionalities of chip-sized laboratories: transport and mixing [2, 3].

It has long been recognized that electro-osmosis is a very efficient and scalable mechanism to use in nano-scale pumps [4]. The classical electro-osmotic pump is based on a charged surface and operated with ionic solutions. Under influence of an electric field,

the ions move along the surface and drag the fluid along. Alternatively, electro-osmotic pumping can be achieved at a neutral channel surface with a salt solution of which the cations and anions have different affinities for the surface [67, 141]. In this case, the asymmetric distribution of ions generates a finite torque in the interfacial liquid layer, causing the fluid to move in one direction.

The use of carbon nanotubes as channels and pumps in nanofluidic devices has been a major aim for the nanofluidic community ever since the discovery that water moves almost frictionless through carbon nanotubes, see Chapter 3 [42, 43]. However, the fact that nanotubes are uncharged limits the possibilities for their use as active electro-osmotic components. Different ways of pumping fluid with carbon nanotubes have been suggested. Using molecular dynamics simulations, Insepov *et al.* demonstrated that gas molecules can be moved peristaltically through a nanotube under influence of a traveling acoustic wave [142]. A little later, Longhurst and Quirke showed that a temperature gradient moves decane molecules through a nanotube, also using molecular dynamics simulations [143]. A slightly different method was proposed by Král and Tománek, making use of the semi-conducting properties of nanotubes to move particles through the tube due to the coupling to laser-excited propagating electrons [144].

Many examples of efficient nano-scale pumps and channels are found in nature, where different protein channels transport water, ions and macromolecules in a highly specific manner across membranes [5, 6]. A synthetic channel exhibiting some of the selective transport and fast flow properties of biological channels would have a wide range of possible applications, not only for pumping, but also for filtering and desalination. To realize this goal, Gong *et al.* designed a nanotube with a fixed external charge distribution mimicking the charge distribution on an aquaporin channel. In molecular dynamics simulations, they observed a finite water flow through the tube [61]. Fixed charges outside a carbon nanotube also influence the pressure-driven passage of water molecules [59]. Finally, uncharged channels filled with solutions of the relatively symmetric salts sodium chloride or potassium chloride were found to exhibit electro-osmotic flow [62–64].

The pumping efficiency and performance of electrokinetically driven channels can be expressed in terms of the ζ-potential, which is a material property defined by the Helmholtz-Smoluchowski equation

$$\zeta = -\frac{\eta u}{\varepsilon\varepsilon_0 E}, \tag{4.1}$$

with η the shear viscosity, $\varepsilon\varepsilon_0$ the permittivity, E the electric field and u the bulk fluid velocity in the direction of E. According to standard theory, a non-zero ζ-potential arises only in the presence of mobile charged species, which limits the use of electrokinetic effects in uncharged nano-channels. However, the ζ-potential of solutes in water has been a source of controversy for many years [45, 49, 50]. Ever since the first electrophoretic measurements it has been known that nominally uncharged substances like air bubbles and oil droplets in pure water exhibit a negative ζ-potential [45]. Generally, this negative ζ-potential of uncharged solutes is attributed to the accumulation of negatively charged ions at the solute surface [45–47]. In contrast with this traditional view, a recent simulation paper reports non-zero ζ-potentials for heptane droplets in pure H_2O without mobile ions [51]. Similarly, several molecular dynamics simulations show electro-osmotic flow in hydrophobic channels: Joseph and Aluru report flow in a carbon nanotube under a constant electric field [60] and Gong *et al.* report flows in carbon nanotubes induced by fixed charges outside the nanotube [44, 61]. Most of these simulations [51, 60, 61], the results of which we will critically re-evaluate in this chapter, have been performed using

the molecular dynamics simulation package GROMACS [145]. Apart from their ability to specifically adsorb different types of ions, aqueous interfaces have a strong ordering effect on the first few molecular layers next to the interface. Molecules in the outermost interfacial water layer are preferentially oriented with their H-atoms pointing outward, giving rise to a considerable dipole density [65]. This structured water next to the interface has a profound influence on the dielectric properties, the viscosity and the interaction with ions, among many other surface characteristics [36, 67]. In an attempt to rationalize the surprising results of the simulation exhibiting electrokinetic effects at uncharged aqueous interfaces, the coupling of the electric field to the dipolar surface layer was speculated to provide an alternative mechanism for the appearance of a non-zero ζ-potential, inducing flow through rotation of the ordered water molecules [51, 60].

In this chapter we discuss two central questions: First, can the dipolar ordering of the water surface layer give rise to a non-zero ζ-potential in a static and uniform electric field? And second, can the dipolar nature of water be exploited for electro-hydraulic power conversion, and in that way enable the use of uncharged channels as active electrokinetic components? We show that using a static electric field, electro-osmotic pumping of pure water in a planar or cylindrical hydrophobic channel is impossible. This result, which is confirmed by extensive molecular dynamics simulations, comes from an analysis based on a generalized Navier-Stokes formulation that includes angular momentum in the form of spinning molecules as well as dipolar ordering and relaxation. Employing rotating electric fields combined with suitable boundary conditions, on the other hand, the coupling between water molecular rotation and vorticity can be used to pump a dipolar fluid through a nanofluidic channel.

4.2 Generalized Navier-Stokes Approach

4.2.1 Conservation of Angular Momentum

Whenever an internal force $\boldsymbol{F}^{int}$ acts on some element of a continuum, stress builds up that is described by a non-vanishing stress tensor P for which $\mathsf{P}_{ij}\hat{n}_j \mathrm{d}\mathcal{A} = \mathrm{d}F_i^{int}$, with $\mathrm{d}\mathcal{A}$ the surface area of the element and $\hat{\boldsymbol{n}}$ the vector normal to the surface. Note that in the following we denote P_{ij} as the shear stress tensor in order to distinguish it from the stress tensor associated with the spinning of molecules. The shear stress tensor can be split into a part corresponding to the hydrostatic pressure p and a friction part $\mathsf{\Pi}$, which in turn can be split into a symmetric part $\mathsf{\Pi}^s$ and an antisymmetric part $\mathsf{\Pi}^a$,

$$\mathsf{P} = -p\mathsf{U} + \mathsf{\Pi} \quad \text{and} \quad \mathsf{\Pi} = \mathsf{\Pi}^s + \mathsf{\Pi}^a, \tag{4.2}$$

with U the unit tensor. For a mono-atomic fluid the antisymmetric part $\mathsf{\Pi}^a$ of the shear stress tensor is zero. In a polar fluid, the interaction between two points in the fluid is not only modeled via the internal force vector and the associated stress tensor, but also via the torque per unit mass $\boldsymbol{\Gamma}^{int}$. Equivalent to Cauchy's stress principle for the force $\boldsymbol{F}^{int}$, there is a spin stress tensor C for which $\mathsf{C}_{ij}\hat{n}_j \mathrm{d}\mathcal{A} = \mathrm{d}\Gamma_i^{int}$ holds. The total rate of change of the angular momentum per unit mass $\boldsymbol{L}$, integrated over a material volume $\mathcal{V}$, can be written as

$$\iiint_{\mathcal{V}} \frac{\partial}{\partial t}\left(\varrho \boldsymbol{L}\right) \mathrm{d}\mathcal{V} + \oiint_{\partial\mathcal{V}} \left(\varrho \boldsymbol{L}\right) \boldsymbol{u}\cdot\hat{\boldsymbol{n}}\, \mathrm{d}\mathcal{A} = \iiint_{\mathcal{V}} \varrho \frac{\mathrm{d}\boldsymbol{L}}{\mathrm{d}t}\, \mathrm{d}\mathcal{V}, \tag{4.3}$$

with $\boldsymbol{u}$ the velocity of the molecules and $\varrho\left(\boldsymbol{x}, t\right)$ the mass density. The material derivative $\mathrm{d}/\mathrm{d}t$ is defined as $\mathrm{d}/\mathrm{d}t = \partial/\partial t + \boldsymbol{u}\cdot\nabla$. These considerations lead to the following balance

equation for the total rate of change of $\boldsymbol{L}$,

$$\begin{aligned}\iiint_{\mathcal{V}} \varrho \frac{\mathrm{d}\boldsymbol{L}}{\mathrm{d}t}\,\mathrm{d}\mathcal{V} &= \iiint_{\mathcal{V}} \varrho\,(\boldsymbol{\Gamma} + \boldsymbol{x}\times\boldsymbol{F})\,\mathrm{d}\mathcal{V} + \oiint_{\partial\mathcal{V}} \hat{\boldsymbol{n}}\cdot(\mathsf{C} + \boldsymbol{x}\times\mathsf{P})\,\mathrm{d}\mathcal{A} \\ &= \iiint_{\mathcal{V}} \varrho\,(\boldsymbol{\Gamma} + \boldsymbol{x}\times\boldsymbol{F}) + \nabla\cdot\mathsf{C} + \nabla\cdot(\boldsymbol{x}\times\mathsf{P})\,\mathrm{d}\mathcal{V},\end{aligned} \tag{4.4}$$

with $\boldsymbol{x}$ the position vector. Rearranging the last term on the right-hand side of Eq. 4.4 yields $\nabla\cdot(\boldsymbol{x}\times\mathsf{P}) = \boldsymbol{x}\times(\nabla\cdot\mathsf{P}) + 2\boldsymbol{\Pi}^a$, where $\boldsymbol{\Pi}^a_k = -1/2\,\epsilon_{ijk}\Pi^a_{ij}$ is the antisymmetric part of the shear stress tensor in axial vector representation, with ϵ_{ijk} the Levi-Civita tensor. Realizing that Eq. 4.4 holds for any volume $\mathcal{V}$ yields the local conservation of total angular momentum:

$$\varrho\frac{\mathrm{d}\boldsymbol{L}}{\mathrm{d}t} = \varrho\,(\boldsymbol{\Gamma} + \boldsymbol{x}\times\boldsymbol{F}) + \nabla\cdot\mathsf{C} + \boldsymbol{x}\times(\nabla\cdot\mathsf{P}) + 2\boldsymbol{\Pi}^a. \tag{4.5}$$

The total angular momentum can be written as the sum of the vorticity contribution $\boldsymbol{x}\times\boldsymbol{u}$ and a spin contribution $\mathsf{I}\boldsymbol{\omega}$, accounting for molecular rotation,

$$\boldsymbol{L} = \boldsymbol{x}\times\boldsymbol{u} + \mathsf{I}\boldsymbol{\omega}, \tag{4.6}$$

with I the moment of inertia per unit mass and $\boldsymbol{\omega}$ the average angular velocity of the constituent particles. The moment of inertia I is a tensor depending on the mass distribution within the particles and on the local orientational distribution. Because of the approximate mass isotropy of the water molecules, the tensor I is almost diagonal even if the orientational distribution of water molecules is very anisotropic, as happens to be the case close to an interface [146]. We therefore take I to be a diagonal tensor with value I. For the first part of Eq. 4.6 we write down a separate conservation law, starting from the conservation law for linear momentum,

$$\varrho\frac{\mathrm{d}\boldsymbol{u}}{\mathrm{d}t} = \varrho\boldsymbol{F} + \nabla\cdot\mathsf{P}. \tag{4.7}$$

We take the vectorial product of $\boldsymbol{x}$ with Eq. 4.7, leading to

$$\varrho\frac{\mathrm{d}}{\mathrm{d}t}(\boldsymbol{x}\times\boldsymbol{u}) = \varrho\,(\boldsymbol{x}\times\boldsymbol{F}) + \boldsymbol{x}\times(\nabla\cdot\mathsf{P})\,. \tag{4.8}$$

The difference between Eqs. 4.5 and 4.8 gives the conservation law for the spin part of the angular momentum density:

$$\varrho I\frac{\mathrm{d}\boldsymbol{\omega}}{\mathrm{d}t} = \varrho\boldsymbol{\Gamma} + \nabla\cdot\mathsf{C} + 2\boldsymbol{\Pi}^a. \tag{4.9}$$

To leading order, C only depends on $\boldsymbol{\omega}$. Equation 4.9 then shows that to leading order, the only coupling between the vorticity part and the spin part of the angular momentum comes from the antisymmetric part of the shear stress tensor Π^a.

4.2.2 Material Equations

We now derive expressions for the terms occurring on the right-hand side of Eq. 4.9. If two neighboring fluid elements moving with velocity $\boldsymbol{u}$ are rotating each with the angular velocity $\boldsymbol{\omega} = 1/2\,\nabla\times\boldsymbol{u}$, the internal spin and the vorticity are synchronized, and no stress results. The antisymmetric part of the shear stress tensor should therefore be a function

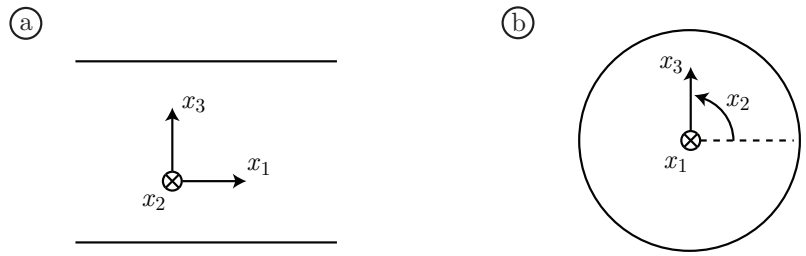

Figure 4.1: *Sketches of* (a) *the rectangular geometry and* (b) *the cylindrical geometry.*

of $^1/_2 \nabla \times \boldsymbol{u} - \boldsymbol{\omega}$. Additionally, $\boldsymbol{\Pi}^a$ should vanish when $\nabla \times \boldsymbol{u} = 2\boldsymbol{\omega}$, and the axial vector of $\boldsymbol{\Pi}^a$ should have the same direction as $\nabla \times \boldsymbol{u} - 2\boldsymbol{\omega}$ [147]. Therefore, to leading order we can write

$$\boldsymbol{\Pi}^a = \eta_r \left(\nabla \times \boldsymbol{u} - 2\boldsymbol{\omega} \right), \tag{4.10}$$

with η_r the vortex viscosity. To leading order, the spin stress tensor C should depend on spatial differences in the spin field $\boldsymbol{\omega}$ only. By equilibrating the second moments of the force, the spin stress tensor can be proven to be symmetric [148]. Disregarding higher derivatives as for the shear stress tensor we write

$$\mathsf{C}_{ij} = \nu_v \nabla_k \omega_k \delta_{ij} + \nu \left(\nabla_j \omega_i + \nabla_i \omega_j - {}^2/_3 \nabla_k \omega_k \delta_{ij} \right), \tag{4.11}$$

with ν the spin viscosity, ν_v the volume spin viscosity and using the Einstein summation convention as in the rest of the chapter. Combining Eqs. 4.9, 4.10 and 4.11 yields

$$\varrho I \frac{\mathrm{d}\boldsymbol{\omega}}{\mathrm{d}t} = \varrho \boldsymbol{\Gamma} + 2\eta_r \left(\nabla \times \boldsymbol{u} - 2\boldsymbol{\omega} \right) + \nu \Delta \boldsymbol{\omega} + \left(\nu + {}^1/_3 \, \nu_v \right) \nabla \nabla \cdot \boldsymbol{\omega}. \tag{4.12}$$

The flow velocity is described by the Navier-Stokes equation for incompressible fluids in the absence of a body force,

$$\varrho \frac{\mathrm{d}\boldsymbol{u}}{\mathrm{d}t} = -\nabla p + \eta \Delta \boldsymbol{u} - \eta_r \nabla \times \left(\nabla \times \boldsymbol{u} - 2\boldsymbol{\omega} \right), \tag{4.13}$$

with p the hydrostatic pressure and η the shear viscosity.

4.2.3 General Stationary Solution For Planar Substrates

Considering a rectangular geometry with the fluid confined to a slab between two surfaces, as sketched in Fig. 4.1 (a), both the velocity and spin field depend only on x_3 because of translational invariance along the x_1 and x_2 directions. Additionally, because of incompressibility, the velocity is restricted to the x_1 direction, leading to $\boldsymbol{u} = \hat{e}_1 u_1 (x_3)$ and $\boldsymbol{\omega} = \boldsymbol{\omega} (x_3)$. Thus, the only non-zero component of the vorticity $\nabla \times \boldsymbol{u}$ is the x_2 component. In steady state, Eq. 4.12 reduces to

$$\begin{aligned} 0 =& \varrho \Gamma_1 + \nu \nabla_3^2 \omega_1 - 4\eta_r \omega_1 \\ 0 =& \varrho \Gamma_2 + \nu \nabla_3^2 \omega_2 + 2\eta_r \left(\nabla_3 u_1 - 2\omega_2 \right) \\ 0 =& \varrho \Gamma_3 + \nu \nabla_3^2 \omega_3 - 4\eta_r \omega_3 + \left(\nu + {}^1/_3 \, \nu_v \right) \nabla_3^2 \omega_3, \end{aligned} \tag{4.14}$$

so if no torque is applied in x_1 and x_3 directions, the angular velocity in these directions is zero. Assuming spatially constant hydrostatic pressure p, we work out Eq. 4.13 for the assumptions mentioned above and integrate once over x_3, leading to

$$(\eta + \eta_r)\,\nabla_3 u_1 = 2\eta_r \omega_2 + c_1\,(\eta + \eta_r)\,, \tag{4.15}$$

where c_1 is an integration constant that has to be determined from the boundary conditions. Eq. 4.15 indicates that the vorticity arising from molecular rotation is a linear function of the angular velocity of the molecules. Inserting Eq. 4.15 in the x_2 component of Eq. 4.14 yields the following differential equation for ω_2,

$$0 = \frac{\varrho\Gamma_2}{\nu} + \left(\nabla_3^2 - \kappa^2\right)\omega_2 + \frac{2c_1\eta_r}{\nu}, \tag{4.16}$$

which is valid for arbitrary torque Γ_2. The square of the spin screening length κ used in Eq. 4.16 is defined as

$$\kappa^2 = \frac{4\eta\eta_r}{\nu\,(\eta + \eta_r)}. \tag{4.17}$$

If Γ_2 has a spatial dependence, but is independent of ω_2, Eq. 4.16 has the following solution,

$$\omega_2\,(x_3) = c_2 e^{\kappa x_3} + c_3 e^{-\kappa x_3} + \int_{-\infty}^{\infty} \frac{\varrho\Gamma_2\,(x_3') + 2\eta_r c_1}{2\kappa\nu}\; e^{-\kappa|x_3 - x_3'|}\,\mathrm{d}x_3', \tag{4.18}$$

where the constants c_i are determined by the boundary conditions. The flow profile follows from Eq. 4.15 as

$$\begin{aligned} u_1\,(x_3) = c_1 x_3 + \frac{\nu\kappa^2}{2\eta}\Bigg[&\frac{c_2}{\kappa}\,e^{\kappa x_3} - \frac{c_3}{\kappa}\,e^{-\kappa x_3} + \frac{c_4}{\kappa} \\ &+ \iint_{-\infty}^{\infty} \frac{\varrho\Gamma_2\,(x_3') + 2\eta_r c_1}{2\kappa\nu}\; e^{-\kappa|x_3 - x_3'|}\,\mathrm{d}x_3'\,\mathrm{d}x_3\Bigg]. \end{aligned} \tag{4.19}$$

4.2.4 Torque from a Static Uniform Electric Field

The ζ-potential is given by the bulk fluid flow induced in the direction of a static electric field. To solve Eq. 4.16 for this situation, we calculate the torque $\boldsymbol{\Gamma} = \boldsymbol{\mu} \times \boldsymbol{E}$ for a constant electric field E_1^0 in x_1 direction. We model the dipolar ordering of the interfacial water layer by an additional x_3-dependent electric field $E_3^{\mu}\,(x_3)$ in x_3 direction. This field accounts for the interaction between neighboring water molecules and plays the role of the crystal field that is used in ordinary mean-field theory for magnetic systems. The total electric field in the system becomes $\boldsymbol{E} = \hat{e}_3 E_3^{\mu}\,(x_3) + \hat{e}_1 E_1^0$. The linear evolution equation for the polarization density $\boldsymbol{\mu} = \boldsymbol{\mu}\,(x_3)$ is given by

$$\frac{\mathrm{d}\boldsymbol{\mu}}{\mathrm{d}t} = \frac{1}{\tau}\,(\alpha\boldsymbol{E} - \boldsymbol{\mu}) + \boldsymbol{\omega} \times \boldsymbol{\mu}, \tag{4.20}$$

with τ the relaxation time of the orientation and α the polarizability per unit mass. Because of translational invariance and directional symmetry in x_2 direction, the dipole moment in x_2 direction vanishes: $\mu_2 = 0$. Since also $E_2 = 0$, it follows that the torque

$\Gamma_1 = \Gamma_3 = 0$, and therefore $\omega_1 = \omega_3 = 0$ by virtue of Eq. 4.14. Eq. 4.20 is solved for $\boldsymbol{\mu}$ in steady state, yielding

$$\mu_1 = \frac{\alpha E_1^0 + \tau\omega_2\alpha E_3^\mu}{1+\tau^2\omega_2^2} \quad \text{and} \quad \mu_3 = \frac{\alpha E_3^\mu - \tau\omega_2\alpha E_1^0}{1+\tau^2\omega_2^2}. \tag{4.21}$$

For the x_2 component of the torque density, $\Gamma_2 = \mu_3 E_1 - \mu_1 E_3$, it follows

$$\Gamma_2 = -\frac{\tau\omega_2\alpha\left(E_1^{0\,2} + E_3^{\mu\,2}\right)}{1+\tau^2\omega_2^2}. \tag{4.22}$$

Inserting Eq. 4.22 into Eq. 4.16 yields the following equation for the spin field,

$$0 = -\frac{\varrho\tau\omega_2\alpha\left(E_1^{0\,2} + E_3^{\mu\,2}\right)}{\nu\left(1+\tau^2\omega_2^2\right)} + \left(\nabla_3^2 - \kappa^2\right)\omega_2 + \frac{2c_1\eta_r}{\nu}. \tag{4.23}$$

Strikingly, Eq. 4.23 is quadratic in the external field strength E_1^0, which means that switching the sign of E_1^0 leaves the equation invariant. Also, since c_1 is an arbitrary integration constant only subject to the spinning boundary conditions at the surface, the sign of ω_2 is undetermined, meaning that a non-zero value of ω_2 would require a spontaneous symmetry breaking, which seems unphysical. In fact, it can be shown that in hydrodynamics, the stable solution corresponds to the solution of minimal dissipation or minimal entropy production, which is obviously the solution corresponding to $\omega_2 = 0$ [127]. Therefore, the only physical and also stable solution is the one corresponding to a vanishing spin field, $\omega_2 = 0$ and thus the integration constant c_1 also vanishes, $c_1 = 0$. If $\omega_2 = 0$, the vorticity also vanishes according to Eq. 4.15, and no flow results. From the Helmholtz-Smoluchowski equation (Eq. 4.1) it is directly evident that this means that neutral solutes in a pure dipolar fluid without mobile charges have zero ζ-potential, in accord with the Onsager reciprocal relation discussed in Sec. 3.3. This stands in contrast with a few published molecular dynamics simulation results [51, 60, 61], as mentioned in the introduction, and will be discussed and resolved with the help of molecular dynamics simulations further below.

4.2.5 Homogeneous Time-Dependent Electric Fields

For time-dependent electric fields, the time derivatives on the left-hand sides of Eqs. 4.12 and 4.13 do not vanish. For homogeneous fields, however, all substantial time derivatives reduce to partial time derivatives, due to the assumption that $u_1(x_3, t)$ is the only non-zero component of the fluid velocity. Again, we consider the case where no electric field is applied in x_2 direction, and $\mu_2 = 0$ because of symmetry and translational invariance. Because from Eq. 4.14 it follows that $\omega_1 = \omega_3 = 0$, the equations for the polarization density (Eq. 4.20) reduce to

$$\begin{aligned} \frac{\partial\mu_1}{\partial t} &= \frac{1}{\tau}(\alpha E_1 - \mu_1) + \omega_2\mu_3 \\ \frac{\partial\mu_3}{\partial t} &= \frac{1}{\tau}(\alpha E_3 - \mu_3) - \omega_2\mu_1. \end{aligned} \tag{4.24}$$

Via ω_2, changes in the polarization in x_1 direction are coupled to changes in x_3 direction and *vice versa*, so the whole system of equations has to be solved simultaneously. The

homogeneous solution ($\boldsymbol{E} = 0$) to Eq. 4.24 equals

$$\begin{aligned} \mu_1(x_3,t) &= e^{-t/\tau}\left(C_1\sin\Omega_2 + C_2\cos\Omega_2\right) \\ \mu_3(x_3,t) &= e^{-t/\tau}\left(C_1\cos\Omega_2 - C_2\sin\Omega_2\right), \end{aligned} \tag{4.25}$$

with C_i denoting integration constants and

$$\Omega_2 = \int_0^t \omega_2\left(x_3,t'\right)\mathrm{d}t'. \tag{4.26}$$

The particular solutions of Eq. 4.24 depend on the electric field applied.

Torque from an electric field step function. For an electric field $E_3^\mu(x_3)$ in x_3 direction that is constant in time and a spatially constant field in x_1 direction of strength E_1^0 that is switched on at $t = 0$, the particular solution is a constant dipole density, leading to the full solution

$$\begin{aligned} \mu_1(x_3,t) &= e^{-t/\tau}\left(C_1\sin\Omega_2 + C_2\cos\Omega_2\right) + \frac{\alpha E_1^0 + \alpha\tau\omega_2(x_3,t)\,E_3^\mu(x_3)}{1+\tau^2\omega_2(x_3,t)^2} \\ \mu_3(x_3,t) &= e^{-t/\tau}\left(C_1\cos\Omega_2 - C_2\sin\Omega_2\right) + \frac{\alpha E_3^\mu(x_3) - \alpha\tau\omega_2(x_3,t)\,E_1^0}{1+\tau^2\omega_2(x_3,t)^2}. \end{aligned} \tag{4.27}$$

We determine C_1 and C_2 from the initial conditions: $\mu_1 = 0$ and $\mu_3(x_3) = \alpha E_3^\mu(x_3)$ at $t = 0$, giving non-zero expressions for both C_1 and C_2:

$$\begin{aligned} C_1(x_3) &= \frac{\alpha E_3^\mu(x_3)\,\tau^2\omega_2(x_3,0)^2 - \alpha\tau\omega_2(x_3,0)\,E_1^0}{1+\tau^2\omega_2(x_3,0)^2} \\ C_2(x_3) &= -\frac{\alpha E_1^0 + \alpha\tau\omega_2(x_3,0)\,E_3^\mu(x_3)}{1+\tau^2\omega_2(x_3,0)^2}, \end{aligned} \tag{4.28}$$

with $\omega_2(x_3,0)$ the spin field at $t = 0$. The torque density $\Gamma_2 = \mu_3 E_1 - \mu_1 E_3$ becomes

$$\begin{aligned} \Gamma_2(x_3,t) = e^{-t/\tau}\Big[&\left(C_1E_1^0 - C_2E_3^\mu(x_3)\right)\cos\Omega_2 - \left(C_2E_1^0 + C_1E_3^\mu(x_3)\right)\sin\Omega_2\Big] \\ &- \frac{\alpha\tau\omega_2(x_3,t)\left({E_1^0}^2 + E_3^\mu(x_3)^2\right)}{1+\tau^2\omega_2(x_3,t)^2}. \end{aligned} \tag{4.29}$$

The conservation law for the angular momentum (Eq. 4.12) and the Navier Stokes equation (Eq. 4.13) form another set of coupled partial differential equations which are difficult to solve in the general case. However, considering the fact that Γ_2 contains both sines and cosines of Ω_2 it is clear that $\omega_2(x_3,t) = 0$ is no longer a solution. For $t \to \infty$, Eq. 4.29 reduces to the torque from a constant electric field (Eq. 4.22), and the flow vanishes. In conclusion, suddenly switching on a spatially constant electric field will give rise to a transient pumping effect that quickly fades away.

4.2.6 Torque from a Rotating Electric Field

Continuous pumping of fluid can only be achieved when a steady-state torque is injected into the system. The easiest way to apply a steady-state torque to a dipolar fluid is using

a rotating electric field. Adding an electric field that is rotating in the $x_1 - x_3$ plane to the dipolar ordering field E_3^μ, the total electric field is given by

$$E_1 = E_\gamma \sin \gamma t \quad \text{and} \quad E_3 = E_\gamma \cos \gamma t + E_3^\mu \left(x_3\right), \tag{4.30}$$

with γ the frequency and E_γ the amplitude of the rotating field. Again, we assume $\boldsymbol{u} = \hat{e}_1 u_1 \left(x_3\right)$ and $\boldsymbol{\omega} = \boldsymbol{\omega}\left(x_3\right)$. Because of the combination of the rotating field and the time-independent field E_3^μ, the torque, and therefore the spin and velocity fields, depend on time. This time dependence, however, is a periodically varying contribution to otherwise constant quantities. Because we are not interested in the short-time scale behavior of the flow, we time-average Eqs. 4.12 and 4.13 over one cycle of the rotating field, leading to the analogues of Eqs. 4.14 and 4.15, now containing the time-averaged quantities $\bar{\Gamma}_2\left(x_3\right)$, $\bar{\omega}_2\left(x_3\right)$ and $\bar{u}_1\left(x_3\right)$. Inserting the rotating electric field into Eq. 4.20 for the time evolution of the dipole moment, we find the following solution,

$$\begin{aligned}
\mu_1\left(x_3, t\right) &= \alpha E_\gamma \cos\phi \sin\left(\gamma t - \phi\right) + \frac{\alpha E_3^\mu \omega_2 \tau}{1 + \omega_2^2 \tau^2} \\
&\quad + e^{-t/\tau}\left(C_1 \cos \omega_2 t + C_2 \sin \omega_2 t\right) \\
\mu_3\left(x_3, t\right) &= \alpha E_\gamma \cos\phi \cos\left(\gamma t - \phi\right) + \frac{\alpha E_3^\mu}{1 + \omega_2^2 \tau^2} \\
&\quad + e^{-t/\tau}\left(C_2 \cos \omega_2 t - C_1 \sin \omega_2 t\right),
\end{aligned} \tag{4.31}$$

where we use the definition $\phi = \arctan\left[\left(\gamma - \omega_2\right)\tau\right]$. In Eq. 4.31, ω_2 depends on x_3, and C_1 and C_2 are constants that can be determined from the initial conditions. Therefore, if the field has persisted for a sufficient amount of time, the dipole density will follow the electric field with a phase difference ϕ. The time-averaged torque is given by

$$\bar{\Gamma}_2 = \frac{\gamma}{2\pi} \int_0^{\frac{2\pi}{\gamma}} \left(\mu_3 E_1 - \mu_1 E_3\right) \mathrm{d}t. \tag{4.32}$$

Inserting $\boldsymbol{E}$ from Eq. 4.30 and $\boldsymbol{\mu}$ from Eq. 4.31 we find in the long-time limit

$$\bar{\Gamma}_2 = \frac{\alpha E_\gamma^2 \left(\gamma - \omega_2\right)\tau}{1 + \left(\gamma - \omega_2\right)^2 \tau^2} - \frac{\alpha {E_3^\mu}^2 \omega_2 \tau}{1 + \omega_2^2 \tau^2}. \tag{4.33}$$

The appearance of E_3^μ in the equation for the time-averaged torque comes from the fact that the spin field couples the dipole density in x_3 direction to the dipole density in x_1 direction. Because E_3^μ depends on x_3, the equation for $\bar{\omega}_2$ (Eq. 4.16 with Γ_2 and ω_2 replaced by $\bar{\Gamma}_2$ and $\bar{\omega}_2$ respectively) does not have an analytical solution anymore. To proceed, we first solve for $\bar{u}_1$ analytically using a perturbative approximation for the torque, afterwards we solve for $\bar{u}_1$ numerically.

Perturbative analysis. For the sake of power counting we assume the electric fields E_γ and E_3^μ to be of order E. Because the polarization $\boldsymbol{\mu}$ depends linearly on the electric field, the torque $\boldsymbol{\Gamma} = \boldsymbol{\mu} \times \boldsymbol{E}$ is proportional to E^2. To leading order, the spin field ω_2 is proportional to the torque Γ_2, and therefore also to E^2. Performing a perturbation analysis of Eq. 4.33 in powers of E yields to leading order

$$\bar{\Gamma}_2 = \frac{\alpha E_\gamma^2 \gamma \tau}{1 + \gamma^2 \tau^2} + \mathcal{O}\left(E^4\right). \tag{4.34}$$

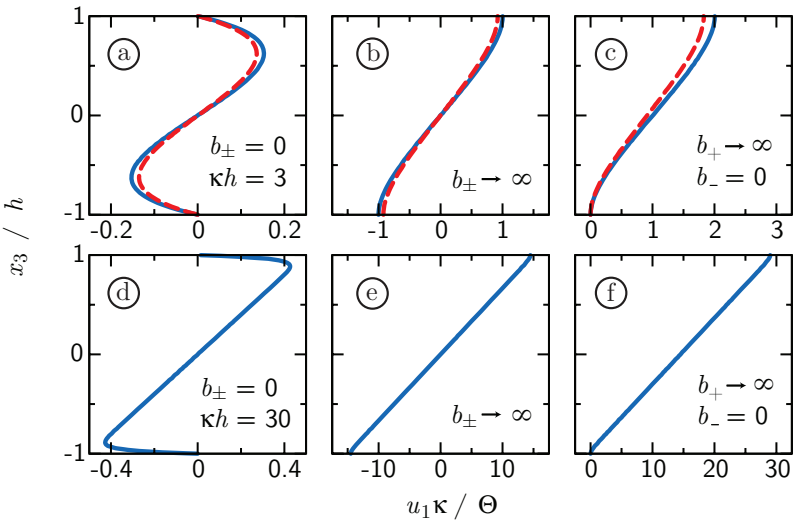

Figure 4.2: *Rescaled flow velocity in channels of rescaled height $\kappa h = 3$ (top) and $\kappa h = 30$ (bottom) for vanishing spin slip length $s = 0$. Solid lines depict the flow profiles from the perturbative approach for* (a) *and* (d)*: a symmetric hydrophilic channel (Eq. 4.42),* (b) *and* (e)*: a symmetric hydrophobic channel (Eq. 4.43) and* (c) *and* (f)*: a channel with a hydrophilic bottom and hydrophobic top surface (Eq. 4.47). The numerical solutions to Eqs. 4.15, 4.16 and 4.33 are shown as dashed lines, using the interfacial dipolar orientation field $E_3^\mu(x_3)$ from simulations as input.*

The effect of the ordering field E_3^μ is of fourth order in the electric field strength, and therefore negligible compared to the leading second order. Nevertheless, pumping of fluid is only possible through surface effects: if the molecules at the boundary are completely free to spin, no momentum will be transferred and no pumping will occur. Obviously, the surface dipolar orientation has a major influence on the spin field at the wall, and neglecting it eliminates most of the interesting physics. Therefore, in the following analysis we include the surface effects of the dipolar order through the boundary condition for the spin field. With Eq. 4.34, Eq. 4.16 has the following solution,

$$\bar{\omega}_2 = \frac{\varrho\bar{\Gamma}_2 + 2\eta_r c_1}{\nu\kappa^2} + c_2 e^{\kappa x_3} + c_3 e^{-\kappa x_3}, \tag{4.35}$$

with integration constants c_i. Using Eq. 4.15 we finally obtain

$$\bar{u}_1 = \left[\frac{\varrho\bar{\Gamma}_2 + 2c_1\,(\eta_r + \eta)}{2\eta}\right] x_3 + \frac{\nu\kappa^2}{2\eta}\left[\frac{c_2}{\kappa}\, e^{\kappa x_3} - \frac{c_3}{\kappa}\, e^{-\kappa x_3} + \frac{c_4}{\kappa}\right]. \tag{4.36}$$

Boundary conditions. Eq. 4.36 contains 4 integration constants. At each channel wall, positioned at $x_3 = \pm h$, there are two boundary conditions, one for the velocity field and one for the spin field. We assume that the velocity at the wall linearly depends on the local shear stress,

$$\mp\, b_\pm \nabla_3 \bar{u}_1|_{\pm h} = \bar{u}_1|_{\pm h}, \tag{4.37}$$

where b is commonly referred to as the slip length, with b_- the slip length at the lower plate and b_+ at the upper plate. For the spin boundary condition, we introduce the spin

slip length s [149]

$$\mp s_{\pm} \nabla_3 \bar{\omega}_2|_{\pm h} = \bar{\omega}_2|_{\pm h}, \tag{4.38}$$

with s_- the spin slip length at the lower plate and s_+ at the upper plate. In a microscopic description, the spin slip length will be largely determined by the restriction on the spinning of the molecules at the wall imposed by orienting wall interactions and by the interaction between neighboring interfacial water molecules. On the hydrodynamic theory level, we treat the slip lengths as free parameters.

Symmetric boundaries. For symmetric boundary conditions $b_- = b_+ = b$ and $s_- = s_+ = s$, Eq. 4.36 gives the following result,

$$\bar{u}_1 = \frac{\Theta \left[(\kappa b \, \mathrm{Cs} + \mathrm{Sn}) \, x_3 - (b+h) \sinh \kappa x_3 \right]}{2 \left[\kappa \, (b+h) \, (\mathrm{Cs} + \kappa s \, \mathrm{Sn}) + (\eta_r/\eta) \, (\kappa h \, \mathrm{Cs} - \mathrm{Sn} + (b+h) \, \kappa^2 s \, \mathrm{Sn}) \right]}, \tag{4.39}$$

where we use the abbreviations $\mathrm{Sn} = \sinh \kappa h$ and $\mathrm{Cs} = \cosh \kappa h$. The typical frequency (or shear rate) is defined by the parameter combination

$$\Theta = \frac{\varrho \alpha E_\gamma^2 \gamma \tau}{\eta \, (1 + \gamma^2 \tau^2)}. \tag{4.40}$$

From Eq. 4.39 and the expression for Θ it follows that the largest amplitude of the flow profile is achieved for $\gamma\tau = 1$, which means for a driving frequency that equals the dipolar relaxation frequency. From calculations and molecular dynamics simulations it is known that the spin viscosity η_r is an order of magnitude smaller than the shear viscosity η [150, 151]. In the limit $\eta_r \ll \eta$, Eq. 4.39 reduces to

$$\bar{u}_1 = \Theta \left[\frac{(\kappa b \cosh \kappa h + \sinh \kappa h) \, x_3 - (b+h) \sinh \kappa x_3}{2\kappa \, (b+h) \, (\cosh \kappa h + \kappa s \sinh \kappa h)} \right]. \tag{4.41}$$

Clearly, the spin slip length s only affects the magnitude of the flow, and not the flow profile. Taking $s = 0$, which is reasonable in view of the strong orienting field at the boundary, and $b = 0$, corresponding to hydrophilic boundaries, Eq. 4.41 can be further simplified to yield

$$\bar{u}_1 = \Theta \left[\frac{x_3 \sinh \kappa h - h \sinh \kappa x_3}{2\kappa h \cosh \kappa h} \right]. \tag{4.42}$$

In Figs. 4.2 (a) and 4.2 (d), the flow profile of Eq. 4.42 is shown as a solid line for channels of rescaled height $\kappa h = 3$ and $\kappa h = 30$ respectively. Taking $s = 0$ and $b \to \infty$, corresponding to very hydrophobic surfaces or air-water interfaces, on the other hand, Eq. 4.41 simplifies to

$$\bar{u}_1 = \Theta \left[\frac{x_3}{2} - \frac{\sinh \kappa x_3}{2\kappa \cosh \kappa h} \right], \tag{4.43}$$

as shown in Figs. 4.2 (b) and 4.2 (e). It is easy to see that for all symmetric channels, the integrated flux Φ vanishes and the net pumping is zero:

$$\Phi = \int_{-h}^{h} \bar{u}_1 \, (x_3) \, \mathrm{d}x_3 = 0. \tag{4.44}$$

Therefore, the symmetry in x_3 direction has to be broken in order to achieve pumping.

Asymmetric boundaries. We consider the limiting case of a channel with a hydrophilic bottom surface ($b_- = 0$) and a hydrophobic top surface ($b_+ \to \infty$). For symmetric spin slip conditions $s_- = s_+ = s$ we find from Eq. 4.36

$$\bar{u}_1 = \Theta \left[\frac{(x_3 + h)\,\kappa \cosh \kappa h - \sinh \kappa h - \sinh \kappa x_3}{2\kappa \left(\cosh \kappa h + (1 + \eta_r/\eta)\,\kappa s \sinh \kappa h \right)} \right], \tag{4.45}$$

which for $\eta_r \ll \eta$ reduces to

$$\bar{u}_1 = \Theta \left[\frac{(x_3 + h)\,\kappa \cosh \kappa h - \sinh \kappa h - \sinh \kappa x_3}{2\kappa \left(\cosh \kappa h + \kappa s \sinh \kappa h \right)} \right]. \tag{4.46}$$

For reasons already mentioned – and because again the spin slip length does not affect the shape of the flow profile – we set it to zero, $s = 0$, leading to

$$\bar{u}_1 = \Theta \left[\frac{x_3 + h}{2} - \frac{\sinh \kappa h + \sinh \kappa x_3}{2\kappa \cosh \kappa h} \right]. \tag{4.47}$$

The profile of Eq. 4.47 is shown in Figs. 4.2 (c) and 4.2 (f) as solid lines. In the asymmetric case, the integrated flow of the channel is for large channels ($\kappa h \ll 1$) given by

$$\Phi = \int_{-h}^{h} \bar{u}_1 \mathrm{d}x_3 \simeq \Theta h^2, \tag{4.48}$$

and thus Φ is clearly finite. It follows by comparison with simple shear flow that Θ is a measure of the shear rate in the channel.

4.2.7 Numerical Solution

To verify the validity of the assumptions inherent to the perturbative approximation, we solve Eq. 4.16 with Eq. 4.33 for the spin field and Eq. 4.15 for the velocity field numerically, subject to the boundary conditions of Eqs. 4.37 and 4.38. As input, the polarizability α and relaxation time τ are needed, as well as the interfacial orienting dipole field E_3^μ. To obtain those parameters we perform a series of molecular dynamics simulations.

Relaxation parameters. We simulate a box of 2180 SPC/E water molecules ($4.0 \times 4.0 \times 4.0$ nm, isotropic pressure coupling, periodic boundary conditions in all directions) with an initially isotropic distribution of water dipoles. At $t = 0$ we turn on an electric field in x_1 direction of strength $E_1^0 = 0.1\ \mathrm{V\,nm^{-1}}$. Relative to experimental values this is a strong electric field, but it is verified that the response is still reasonably linear. We perform 10 cycles of orientation (field turned on for 25 ps) and relaxation (field turned off for 25 ps), and average the result of the orientation part of each cycle. In Fig. 4.3 (a), we plot the average dipole moment per water molecule as a function of time. With a molecular dipole moment of SPC/E water of $\mu_{\mathrm{SPC/E}} = 0.05\ \mathrm{nm}\,e$, we see that the dipolar orientation is sufficiently far from being saturated and we are thus in the linear-response regime. With $\boldsymbol{E} = E_1^0 \hat{\boldsymbol{e}}_1$ and $\mu_1 = 0$ at $t = 0$, the solution to Eq. 4.20 is

$$\mu_1 = \alpha E_1^0 \big(1 - e^{-t/\tau}\big). \tag{4.49}$$

Fitting Eq. 4.49 to the curve in Fig. 4.3 (a) gives a dipolar relaxation time of $\tau = 7 \pm 2$ ps and a polarizability per unit mass of $\alpha = 3.3 \pm 0.3 \times 10^6\ \mathrm{m^2 e V^{-1} kg^{-1}}$, with e the elementary

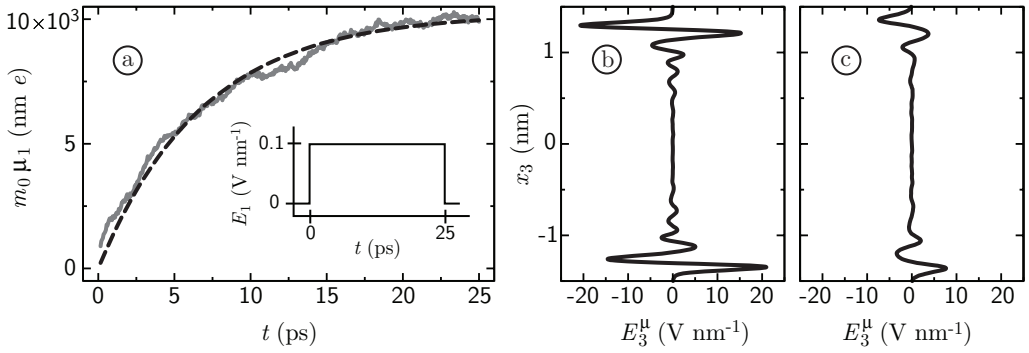

Figure 4.3: (a) *Average dipole moment per molecule, $m_0\mu_1$ with m_0 the mass of a water molecule, as a function of time after turning on an electric field of* 0.1 *V nm^{-1} (solid line). Shown as a dashed line is a fit with Eq. 4.49, and the applied electric field is shown in the inset. Electric field due to the dipolar ordering E_3^μ as a function of x_3 for* (b) *a hydrophilic diamond and* (c) *a hydrophobic diamond.*

charge. The value for τ agrees within 20 per cent with experimental numbers [69] and the value for the polarizability gives in conjunction with the Kirkwood-Fröhlich formula, $\varepsilon = 1 + \varrho\alpha/\varepsilon_0$ with $\varrho = 998\ \mathrm{kg\,m^{-3}}$, a value for the dielectric constant of $\varepsilon = 61 \pm 6$, which is quite close to the known result of $\varepsilon = 71$ for the SPC/E water model [100]. The small deviation might be caused by non-linear effects at the field strength used.

Interfacial orienting dipole field. We also calculate the intrinsic orienting field $E_3^\mu(x_3)$ from molecular dynamics simulations. We simulate two different systems, a hydrogen-terminated diamond and a hydroxide-terminated diamond, as a typical hydrophobic and hydrophilic system, respectively. The hydroxide-terminated surface is constructed by replacing every second C-H group at the surface of the diamond by a C-O-H group, representing a surface coverage of $x_{\mathrm{OH}} = 1/2$, in the notation of Ref. [74]. The systems are solvated in a box of dimensions $6 \times 3 \times 5$ nm containing 1856 SPC/E water molecules, and the electric field is calculated from integrating the charge density over the normal coordinate x_3. In Fig. 4.3 (b – c), the resulting profiles of E_3^μ are shown as a function of x_3 for the two diamond surface types.

Other parameters. The parameters used in the comparison are $\eta = 10^{-3}$ Pa s, $\eta_r = 0.1\eta$ [150], $\varrho = 10^3$ kg m^{-3} and $\kappa^2 = 4\eta\eta_r/[\nu(\eta + \eta_r)]$. For the spin viscosity, of which no estimates are available for water, we make the assumption $\nu = a^2\eta_r$ with $a = 0.3$ nm of the order of the water molecule diameter. This assumption seems reasonable as it is very well obeyed by *e.g.* liquid nitrogen [151–153]. As an example, we choose $s_- = s_+ = 0.5$ nm and $b_- = b_+ = 1.5$ nm, which are reasonable values for a hydrophobic surface [74]. As a dashed line in Fig. 4.4 (a), the torque density $\bar{\Gamma}_2(x_3)$ obtained from Eq. 4.33 is shown as a function of x_3. The torque density is calculated for a rotating electric field and the E_3^μ profile of the hydrophobic diamond, which is shown in Fig. 4.3 (c). The perturbative approximation of the torque density according to Eq. 4.34 is represented by a solid line. Apart from the first ~ 0.5 nm at the wall, the variations in the numerically calculated torque density are small compared to the mean value, and the agreement with the perturbative result is very good. Directly at the wall there are strong oscillations in the torque density, owing

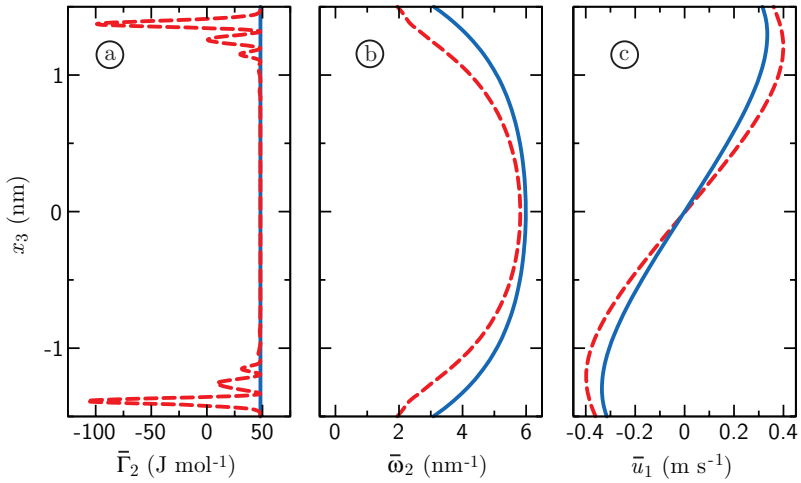

Figure 4.4: (a) *Torque induced by a* $E_\gamma = 0.1$ *Vnm*$^{-1}$ *electric field, rotating at a frequency of* 0.14 *THz* ($\gamma = \tau^{-1}$), (b) *the resulting spin field* $\bar{\omega}_2(x_3)$ *using symmetric boundary conditions of* $s = 0.5$ *nm and* (c) *the resulting flow profile* $\bar{u}_1(x_3)$ *using symmetric boundary conditions of* $b = 1.5$ *nm. The numerical solutions to Eqs 4.15, 4.16 and 4.33 are shown as dashed lines and the analytical approximations, given in Eqs. 4.34, 4.35 and 4.36 are shown as solid lines.*

to the dipole field E_3^μ and the non-linearity of Eq. 4.33. In Figs. 4.4 (b) and 4.4 (c), the numerical solutions to Eqs. 4.15, 4.16 and 4.33 for the spin and velocity field are shown as dashed lines. In the same graphs, the perturbative approximations of Eqs. 4.35 and 4.36 for the spin field and the velocity field are shown as solid lines. Despite the strong oscillations of the torque density directly at the wall, the perturbative approximations are in fair agreement with the numerically calculated profiles, justifying the approximation for small electric field. For the symmetric boundary conditions $b_\pm = 0$ and $b_\pm \to \infty$, and for the asymmetric boundary conditions $b_- = 0, b_+ \to \infty$, the numerical solutions are shown as dashed lines in the top panels of Fig. 4.2, again showing good agreement with the analytically calculated profiles. For the curves shown in Fig. 4.2 we employ for $E_3^\mu(x_3)$ the simulation results obtained with the hydrophilic diamond surfaces for the surfaces with $b = 0$, and the simulation results obtained with the hydrophobic diamond surfaces for the surfaces with $b \to \infty$.

Power dissipation. For a rotating electric field we calculate the power dissipation per unit volume of fluid directly from the rotating dipole moment, leading to the average power dissipation of

$$\bar{P} = \frac{\gamma}{2\pi} \int_0^{2\pi/\gamma} \varrho \frac{\partial \boldsymbol{\mu}}{\partial t} \cdot \boldsymbol{E} \, \mathrm{d}t. \tag{4.50}$$

Inserting the expressions for $\boldsymbol{\mu}$ from Eq. 4.31 and discarding terms of $\mathcal{O}\left(E^4\right)$, we obtain the explicit solution

$$\bar{P} = \gamma \eta \Theta. \tag{4.51}$$

At the typical microwave oven driving frequency of $\gamma = 2\pi \times 2.5$ GHz and an electric field strength of $E_\gamma = 10^{-4}$ V nm^{-1} we find $\bar{P} = 9$ GW m^{-3}. A similar calculation for a unidirectional oscillating electric field, on the other hand, yields $\bar{P}_{uni} = \gamma \eta \Theta / 2$, which is the standard expression for the dissipation due to dipolar relaxation given in Ref. [69], for

example. We thus see that rotating and planar electric fields exhibit identical dissipation; the factor 2 coming from the difference in the spatially averaged quadratic field strength.

Heating effects. Heating of water under influence of microwave radiation is a well-known phenomenon which deserves careful consideration when designing an electro-hydraulic pump. The channel height $2h$ at which the temperature difference between the center and the wall of the channel has a value ΔT is calculated from equating the heat transport through a surface area $\mathcal{A}$ to the power dissipated in a volume $h\mathcal{A}$,

$$k\mathcal{A}\frac{\Delta T}{h} = \bar{P}h\mathcal{A}, \tag{4.52}$$

with k the heat transport coefficient, which has the value $k = 0.6\ \mathrm{W\,m^{-1}K^{-1}}$ for water. At $\gamma = 2\pi \times 2.5$ GHz and $E_\gamma = 10^{-4}\ \mathrm{V\,nm^{-1}}$, the height of the channel for which the temperature difference has the value $\Delta T = 10$ K follows from Eq. 4.52 as $h = 0.03$ mm. This directly shows that heating of the fluid due to dipolar dissipation is negligible for nanofluidic applications. For larger devices, heating should be further reduced, which can be achieved by reducing the driving frequency or the electric field strength.

Pumping efficiency. As a measure of the efficiency of electro-hydraulic pumping with a rotating electric field, we compare the dissipation $\bar{P}$ from Eq. 4.51 to the power dissipation in a simple shear flow generated by a force $F_0\hat{e}_1$ acting on the top surface and a force $-F_0\hat{e}_1$ acting on the bottom surface. We set the shear rate, which equals $\nabla_3 u_1 = F_0/\eta\mathcal{A}$, equal to $\Theta/2$ in order to match the shear generated in the rotating electric field case. The power dissipated per unit volume turns out to be

$$P_{shear} = \frac{2F_0\nabla_3 u_1}{\mathcal{A}} = \frac{\eta\Theta^2}{2}. \tag{4.53}$$

The dissipation ratio is given by

$$\frac{P_{shear}}{\bar{P}} = \frac{\Theta}{2\gamma} \ll 1, \tag{4.54}$$

where for the last inequality we assumed that the response frequency Θ is typically much smaller than the driving frequency γ. It transpires that generating shear flows by exerting surface forces is for typical parameters more efficient than using a rotating microwave, but a microwave-driven pump might be advantageous in certain devices and applications, because of the lack of mechanical parts, for example.

Length scales. In the limit of $\eta_r \ll \eta$, we find a spin screening length $\kappa^{-1} = 0.15$ nm, using the molecular length scale $a = 0.3$ nm. Conventional devices used to create a shear flow can be easily constructed down to a channel size of several tens of micrometers [154, 155]. The length scale $\kappa^{-1} \simeq 0.15$ nm shows that the limit $\kappa h \gg 1$ is relevant and realized already for nanometer-sized channels. A rotating electric field is therefore useful for creating shear flows in channels of a few nanometer up to tens of micrometers, where conventional devices are difficult to use and dipolar heating is not problematic yet. In the limit $\kappa h \gg 1$, the profiles in the planar channels converge to a simple shear flow, with a shear rate of $\Theta/2$. Although the maximum shear rate is obtained for $\gamma\tau = 1$, let us consider the experimentally easily realizable driving frequency of $\gamma = 2\pi \times 2.5$ GHz,

which is the driving frequency of a common microwave oven. For a realistic external field strength $E_\gamma = 10^{-4}$ V nm^{-1}, water viscosity $\eta = 10^{-3}$ Pa s and density $\varrho = 10^3$ kg m^{-3} we find a response frequency of $\Theta = 570$ s^{-1} and thus predict sizeable shear effects.

4.2.8 Cylindrical Geometry

We take x_1 to be the axial coordinate, x_2 the angular coordinate and x_3 the radial coordinate, see Fig. 4.1 (b). Note that this is an uneven permutation of the usual form of the cylindrical coordinates. Again, we assume $\boldsymbol{u} = \hat{e}_1 u_1(x_3)$ (axial flow) and $\boldsymbol{\omega} = \boldsymbol{\omega}(x_3)$ (only dependent on the radial coordinate). The Navier Stokes equation transforms to

$$\varrho \frac{\mathrm{d}u_1}{\mathrm{d}t} = \frac{\eta}{x_3}\frac{\partial}{\partial x_3}\left(x_3\frac{\partial u_1}{\partial x_3}\right) + \frac{\eta_r}{x_3}\frac{\partial}{\partial x_3}\left(x_3\frac{\partial u_1}{\partial x_3} - 2x_3\omega_2\right) \tag{4.55}$$

Integrating Eq. 4.55 once over x_3 yields in the stationary state

$$0 = (\eta + \eta_r)\frac{\partial u_1}{\partial x_3} - 2\eta_r\omega_2 - \frac{c_1(\eta + \eta_r)}{x_3}. \tag{4.56}$$

At the same time,

$$\varrho I\frac{\mathrm{d}\omega_2}{\mathrm{d}t} = \varrho\Gamma_2 + 2\eta_r\left(\frac{\partial u_1}{\partial x_3} - 2\omega_2\right) + \frac{\nu}{x_3}\frac{\partial}{\partial x_3}\left(x_3\frac{\partial\omega_2}{\partial x_3}\right). \tag{4.57}$$

Combining Eqs. 4.56 and 4.57 gives the cylindrical equivalent of Eq. 4.16,

$$0 = \frac{\varrho\Gamma_2}{\nu} + \left(\nabla_3^2 - \kappa^2\right)\omega_2 + \frac{2c_1\eta_r}{\nu x_3}, \tag{4.58}$$

with $\nabla_3^2 = x_3^{-1}(\partial/\partial x_3)\, x_3\, (\partial/\partial x_3)$. In this section we solve Eqs. 4.56 and 4.58 for different scenarios.

Static electric field. The torque resulting from a static electric field is given again by Eq. 4.22. In analogy to the planar case, a static field does not induce a flow through the nanotube.

Constant torque. A steady-state torque, on the other hand, will induce a flow in the cylindrical geometry. Equivalent to the planar case, the torque resulting from a rotating electric field is in good approximation a constant given by Eq. 4.34. Different from the planar situation, however, Eq. 4.58 with constant Γ_2 does not have an analytical solution. Therefore, we solve Eq. 4.58 numerically, after which the velocity profile is calculated from integrating Eq. 4.56. The geometry needed to generate an electric field rotating in the $x_1 - x_3$ plane consists of two concentric cylinders with radii R_1 and R_2, with the radius of the inner cylinder $R_1 > 0$ because Eq. 4.58 diverges in the limit $x_3 \to 0$. A rotating field is generated by applying a sine-like potential difference between the inner cylinder and the outer cylinder, and a cosine-like potential difference between two additional electrodes at both ends of the tube. The boundary conditions at $x_3 = R_1, R_2$ are given by the equivalent expressions of Eqs. 4.37 and 4.38. Due to the intrinsic asymmetry of the system in x_3 direction, the velocity profile not only depends on the difference $R_2 - R_1$, but also on the absolute value of R_1. For $R_1 \to \infty$, Eq. 4.58 approaches Eq. 4.16, so we only treat the case for small R_1 here. In Fig. 4.5, the numerically calculated flow profile is shown for two

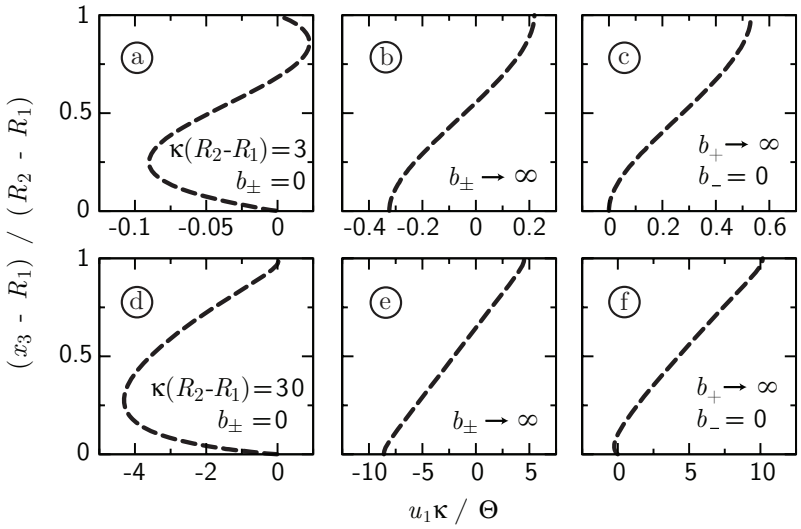

Figure 4.5: *Numerical results for the flow velocity between two concentric cylinders for values of the rescaled inter-cylinder distance* $\kappa\,(R_2 - R_1) = 3$ *(top) and* $\kappa\,(R_2 - R_1) = 30$ *(bottom). The boundary conditions used are symmetric hydrophilic* (a) *and* (d)*, symmetric hydrophobic* (b) *and* (e) *and hydrophilic inner cylinder with hydrophobic outer cylinder* (e) *and* (f)*.*

different values of the rescaled distance $\kappa\,(R_2 - R_1)$ between the two concentric cylinders. The case of symmetric hydrophilic boundary conditions, $b_- = b_+ = 0$, is shown in Figs. 4.5 (a) and 4.5 (d). Contrary to the planar case, the net flow Φ as defined in Eq. 4.44 is non-zero due to the asymmetry of the geometry in x_3 direction. In Figs. 4.5 (b) and 4.5 (e) the flow profile is shown for symmetric hydrophobic boundaries, $b_-, b_+ \to \infty$. In this case the net flow is zero because no momentum can be transferred between the tubes and the fluid. Finally, in Figs. 4.5 (c) and 4.5 (f) the profile is shown for a hydrophilic inner cylinder and a hydrophobic outer cylinder, showing a net positive flow.

4.2.9 Viscosity of a Fluid Consisting of Non-Spherical Particles

Viscosity is generally measured in shear flows. We consider a one-dimensional shear flow of non-spherical particles in a slit of height $2h$, known as a Couette flow, and investigate the effect of molecular rotation on the effective viscosity. To generate a shear flow, forces $F_0\hat{e}_1$ and $-F_0\hat{e}_1$ are applied to the top and bottom plates of the slit. The combination of the Navier-Stokes equation and conservation of angular momentum (Eq. 4.16) in absence of a body torque gives the following equation for the spin field,

$$0 = \left(\nabla_3^2 - \kappa^2\right)\omega_2 + \frac{2c_1\eta_r}{\nu}, \tag{4.59}$$

which has the solution

$$\omega_2 = \frac{2c_1\eta_r}{\kappa^2\nu} + c_2 e^{\kappa x_3} + c_3 e^{-\kappa x_3}. \tag{4.60}$$

In absence of a body force, as is appropriate for a Couette flow, the vorticity is given by Eq. 4.15,

$$\nabla_3 u_1 = \frac{2\eta_r}{\eta + \eta_r}\,\omega_2 + c_1. \tag{4.61}$$

Because $u_1(-x_3) = -u_1(-x_3)$, the vorticity is even, and $\omega_2(x_3) = \omega_2(-x_3)$. Inserting this boundary condition in Eq. 4.60 gives $c_2 = c_3$. Solving Eq. 4.61 and using the symmetry condition $u_1(0) = 0$ yields

$$u_1 = \left(\frac{\eta_r}{\eta} + 1\right) c_1 x_3 + \frac{4\eta_r c_2}{\kappa(\eta + \eta_r)} \sinh \kappa x_3. \tag{4.62}$$

The integration constants c_1 and c_2 are set by the boundary conditions on the spin and velocity field. For the spin field ω_2 we take the boundary condition given in Eq. 4.38 with the spin slip length $s_\pm = s$, from which the integration constant c_2 follows as

$$c_2 = -\frac{c_1 \eta_r}{\kappa^2 \nu (\kappa s \sinh \kappa h + \cosh \kappa h)}. \tag{4.63}$$

For relatively large channels ($\kappa h \gg 1$) – which is any channel with a height exceeding several nanometers – $c_2 \approx 0$. The boundary condition on the velocity field comes from the force on the plates. The relation between the stress tensor and the internal force $\boldsymbol{F}^{int}$ resisting the external force $\boldsymbol{F}_0$ is given by

$$\mathrm{d}F_i^{int} = \mathsf{P}_{ij} \hat{n}_j \mathrm{d}\mathcal{A} = \left(-p\delta_{ij} + \Pi_{ij}^s + \Pi_{ij}^a\right) \hat{n}_j \, \mathrm{d}\mathcal{A}, \tag{4.64}$$

which for the given geometry becomes

$$\mathrm{d}F_1^{int} = \eta \nabla_3 u_1 + \eta_r (\nabla_3 u_1 - 2\omega_2) \hat{n}_3 \, \mathrm{d}\mathcal{A}. \tag{4.65}$$

Using that a force F_0 is applied across the surface area $\mathcal{A}$ of each plate, the boundary condition on the velocity field is expressed as

$$c_1 = \frac{F_0}{(\eta + \eta_r)\mathcal{A}}. \tag{4.66}$$

Inserting c_1 and c_2 into the equation for the flow profile gives

$$u_1 = \frac{F_0}{\eta \mathcal{A}} \left[x_3 + \frac{\eta_r \sinh \kappa x_3}{\kappa(\eta + \eta_r)(\kappa s \sinh \kappa h + \cosh \kappa h)} \right]. \tag{4.67}$$

For channels of $kh \gg 1$, Eq. 4.67 reverts to the usual equation for a Couette flow. Since viscosity is usually measured in large channels, that means that the rotation does not have an influence on the viscosity measured in a shear flow. The vortex viscosity η_r does affect the flow profile close to the wall via the second term in Eq. 4.67, but since $\eta_r \ll \eta$ [150, 151], deviations from the pure Couette flow profile are minor.

4.3 Molecular Dynamics Simulations

4.3.1 Interaction Energy

In molecular dynamics simulations, the Lennard-Jones force is typically truncated at a finite cut-off distance, which can be effectuated in various ways. The default way is to keep the force unchanged out to $r = r_c$, where the force is set to zero, leaving a force discontinuity at $r = r_c$. We will refer to this method as the simple cut-off scheme. Another way is to attenuate the force smoothly to reach zero at $r = r_c$ without discontinuity. In

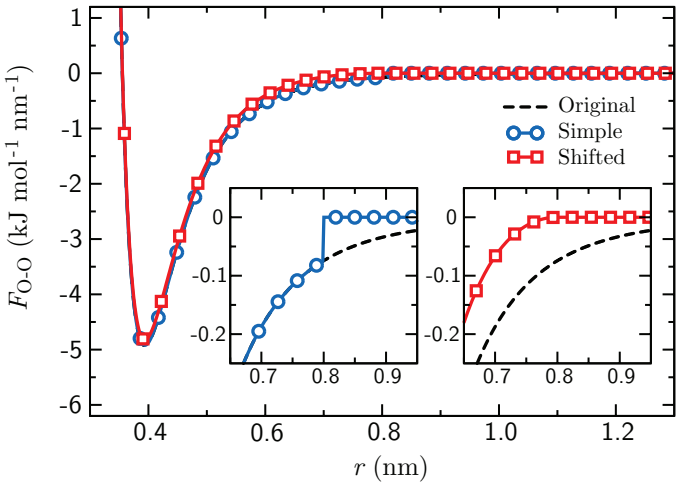

Figure 4.6: *Truncated Lennard-Jones force between two water molecules for $r_c = 0.8$ nm for the two different truncation schemes. Also shown is the original Lennard-Jones force. Details of the truncation region are shown in the insets for the simple cut-off (left) and the shifted cut-off scheme (right).*

GROMACS, this so-called shifted force F_s is implemented by adding a non-linear function to the original force F_o,

$$F_s = \begin{cases} F_o + ar^2 + br^3 & \text{if } r < r_c \\ 0 & \text{if } r \geq r_c. \end{cases} \tag{4.68}$$

The coefficients a and b are given by

$$\begin{aligned} a &= -768\,\epsilon\,\sigma^{12}\,r_c^{-15} + 240\,\epsilon\,\sigma^6\,r_c^{-9} \\ b &= 720\,\epsilon\,\sigma^{12}\,r_c^{-16} - 216\,\epsilon\,\sigma^6\,r_c^{-10}, \end{aligned} \tag{4.69}$$

with ϵ and σ the parameters of the Lennard-Jones interaction and r_c the truncation length in nanometers. The original Lennard-Jones force is given by

$$F_o = 4\epsilon\left[12\frac{\sigma^{12}}{r^{13}} - 6\frac{\sigma^6}{r^7}\right]. \tag{4.70}$$

The interactions between dissimilar atoms are calculated by $\epsilon_{ij} = \sqrt{\epsilon_i\epsilon_j}$ and $\sigma_{ij} = \sqrt{\sigma_i\sigma_j}$, with i and j indices denoting atom type. Examples of the simple and the shifted force are plotted in Fig. 4.6. The curves have been verified by running simulations of two colliding particles.

Other simulation details. The long-range electrostatics are handled using particle mesh Ewald summation. For the simple cut-off scheme, the real-space truncation length for both the Coulomb interaction and the Lennard-Jones interaction is set equal to the list radius, which is the default option in GROMACS. For the simple cut-off scheme, setting the list radius larger than the truncation length is not allowed in GROMACS. For the shifted scheme, the real-space truncation length for the Coulomb interaction and the list radius is set 0.2 nm larger than the Lennard-Jones interaction. The temperature is

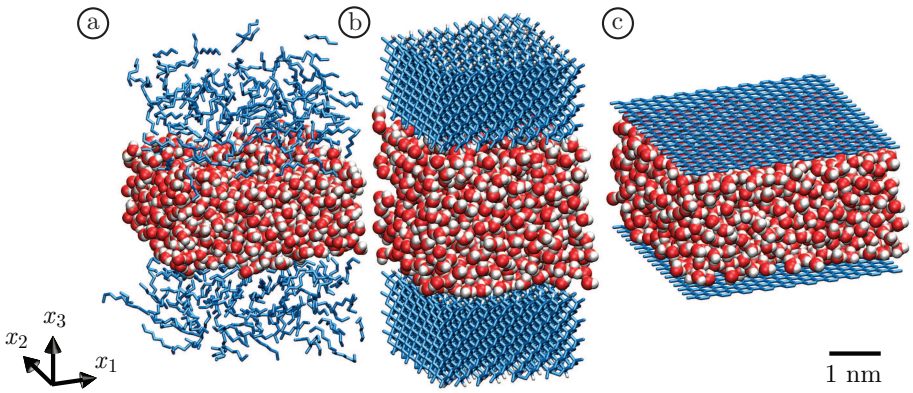

Figure 4.7: *Snapshots of the planar simulation systems consisting of* (a) *a water slab in contact with a slab of heptane,* (b) *a water slab confined by two diamond blocks, and* (c) *a water slab confined by two graphene sheets.*

kept constant at 300 K using a Berendsen thermostat. All systems are equilibrated at a constant pressure of 1 bar using a Berendsen barostat, after which the substrate is frozen and the simulations are run at constant volume, except for the nanotube simulations with reservoir, where an anisotropic Parrinello-Rahman barostat is used throughout the entire simulation. We use periodic boundary conditions in all directions. We perform molecular dynamics simulations for both Lennard-Jones truncation schemes and for different values of r_c.

- It is verified that the update frequency of the list of interacting atoms has no influence on the velocity of the molecules.
- For the simple cut-off scheme, choosing a list radius smaller than the truncation length is found to make no difference.
- Running simulations using single (32 bits) or double (64 bits) numerical precision gives the same results.
- Changing the real space Coulomb truncation length does not make any difference, as expected.
- Choosing the list radius and real-space Coulomb cut-off length equal to the Lennard-Jones truncation length in the shifted scheme does not change the results.
- Using a Nosé-Hoover thermostat instead of a Berendsen thermostat does not change the velocity of the molecules.

4.3.2 Flow Profiles

Planar geometry with a homogeneous electric field. We simulate three different planar substrates in pure water. The first simulation system consists of a hydrogen-terminated diamond surface (double FCC, 2323 C-atoms, 226 H-atoms), solvated in 920 water molecules, giving a total system size of $3.2 \times 3.2 \times 4.7$ nm. The carbon atoms are modeled by the GROMOS 96 force field ($\epsilon_C = 0.277$ kJ mol^{-1} and $\sigma_C = 0.358$ nm). The hydrogen atoms

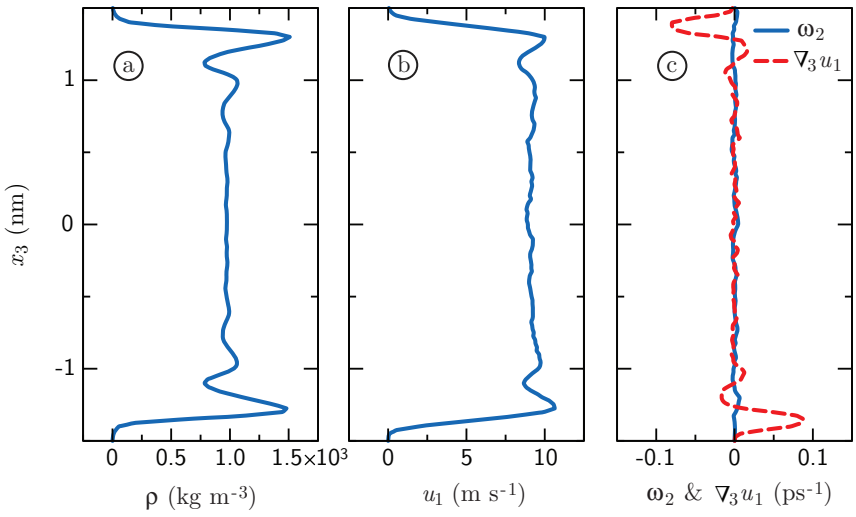

Figure 4.8: *Results of the simulation of the planar diamond system (contact angle* $\sim 111°$*) at* $E = 0.4$ *V nm*$^{-1}$ *as a function of the distance to the wall* x_3*, using the simple cut-off Lennard-Jones truncation and cut-off length* $r_c = 0.8$ *nm.* (a) *Density profile of the fluid.* (b) *Velocity in* x_1 *direction.* (c) *Spin field* ω_2 *(solid line) and vorticity* $\nabla_3 u_1$ *(dashed line).*

have their usual mass, but the Lennard-Jones parameters are set to zero. The contact angle of the diamond equals $\sim 111°$, as calculated from the virial tensor following Ref. [128]. A second set of simulations are performed for an oil slab solvated in water. The simulation box has a size of $4.0 \times 4.0 \times 5.9$ nm, containing 250 $CH_3(CH_2)_5CH_3$ (heptane) molecules and 1013 water molecules. The heptane is modeled exactly as in Ref. [51], with 5 unified CH_2 atoms (Lennard-Jones parameters: $\epsilon_{CH_2} = 0.411$ kJ mol^{-1}, $\sigma_{CH_2} = 0.407$ nm) terminated with 2 CH_3 atoms (Lennard-Jones parameters: $\epsilon_{CH_3} = 0.867$ kJ mol^{-1}, $\sigma_{CH_3} = 0.375$ nm). The third simulation system consists of two frozen sheets of graphene, separated by a vacuum gap of 2.5 nm. The Lennard-Jones parameters of the carbon atoms are identical to the ones used for the diamond simulations. The system is solvated in 1339 SPC/E water molecules, giving a system size of $4.3 \times 4.4 \times 4.9$ nm. The graphene sheet has a contact angle of $\sim 180°$. All simulation systems are visualized in Fig. 4.7.

First, we present simulation results for the diamond surface with a simple cut-off scheme at $r_c = 0.8$ nm. The water density between two periodic images of the diamond is shown in Fig. 4.8 (a). We define the bulk of the system as the region where the water density is constant. The velocity of the fluid is calculated from a numerical derivative of the positions of the centers of mass of the molecules. In Fig. 4.8 (b), the velocity profile of the centers of mass of the water, $u_1(x_3)$, is shown. The velocity in x_1 direction is clearly non-zero, and the fluid moves in the direction of the external electric field, in marked contrast to the analytical results presented in the preceding sections. We will clarify this contradiction further below. As a dashed line in Fig. 4.8 (c), the x_2 component of the vorticity $\nabla_3 u_1$ is shown, together with the spin field ω_2, depicted as a solid line. According to Eq. 4.15 the vorticity should be a linear function of the spin field. Although the vorticity is non-zero, the spin field is zero over the whole range, indicating an unphysical decoupling of the spin and the vorticity, which might serve as a first hint to the failure of the simulation method.

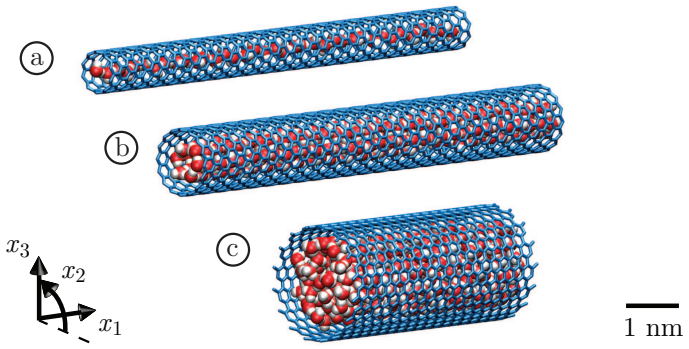

Figure 4.9: *Snapshots of the nanotube simulations without reservoir with* (a) *a (10,0)* CNT, (b) *a (16,0)* CNT *and* (c) *a (16,16)* CNT.

Cylindrical geometry with a homogeneous electric field. For the cylindrical geometry we simulate three carbon nanotubes (CNT's): a (10,0), a (16,0) and a (16,16) CNT, with diameters of 0.782 nm, 1.25 nm and 2.17 nm respectively, as shown in Fig. 4.9. The tubes have a length of 10, 10 and 5 nm, containing 37, 202 and 358 water molecules respectively. The C-C bond has a length of 0.142 nm and the Lennard-Jones parameters of the carbon atoms are identical to the ones used for the diamond simulations. The CNT's are equilibrated in a large bath of solvent using a semi-isotropic Berendsen barostat at 1 bar. After equilibration, the water outside the nanotube is removed. In axial direction, the simulation box is set to the same size as the nanotube, so the nanotube is connected directly to its periodic image. In the other two directions, the box size is 5×5 nm.

In Fig. 4.10 (a), we plot the density inside a (16,16) CNT using a simple cut-off scheme at $r_c = 0.8$ nm. Inside the carbon nanotube, the density never reaches a constant value. Since the velocity shows a plug profile, see Fig. 4.10 (b), we calculate the average velocity of all water molecules inside the tube to use for further analysis. In Fig. 4.10 (c), the spin field ω_2 is shown as a function of x_3. The noise near the nanotube wall and in the center is due to bad statistics, caused by molecules entering the depletion layer for a very short time near the wall and by the small averaging volume in the center. In between the center and the surface, the spin field is zero like in the planar case.

4.3.3 Truncation Length Dependence

Planar systems with homogeneous electric fields. In Fig. 4.11 (a – c), the ζ-potential of the three planar substrates is shown for the two different truncation schemes. The ζ-potential is calculated from Eq. 4.1 and the error bars depict the statistical standard deviation of the velocity in the bulk region as defined above. Clearly, the ζ-potential of all three substrates depends strongly on the truncation scheme used. This dependence on the truncation scheme has no physical meaning, since the minute change of the force profile should not lead to such a tremendous variation of the flow velocity. Besides, according to our analytic calculation, the flow must vanish irrespective of details of the force. The unphysical dependence on the cut-off length in the simple truncation scheme vanishes for large values of the truncation length, and the ζ-potentials in both cut-off schemes converge to zero. The truncation length dependence of the ζ-potential shows that the non-zero flow observed in Figs. 4.8 (b) and 4.10 (b) and by Refs. [51, 60] is an artifact related to the

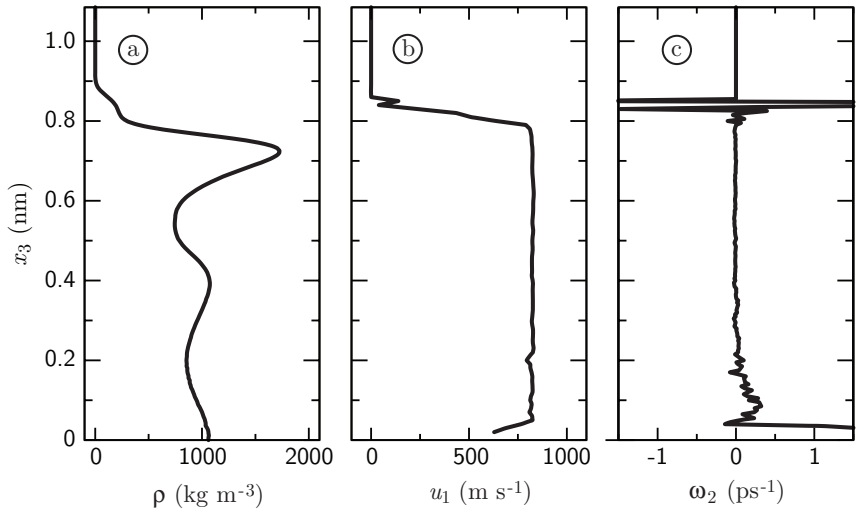

Figure 4.10: *Results of simulations of a (16,16) carbon nanotube without reservoir using the simple cut-off scheme and cut-off length $r_c = 0.8$ nm.* (a) *Density inside the nanotube as a function of the radial distance x_3 from the center.* (b) *Axial velocity in x_1 direction as a function of x_3.* (c) *Spin field in x_2 direction as a function of x_3.*

implementation of the Lennard-Jones force truncation in the simple cut-off scheme.

Cylindrical geometry with homogeneous electric fields. The ζ-potential of each nanotube is calculated from the average velocity inside the tube using Eq. 4.1. In Fig. 4.11 (d – f), we plot the ζ-potentials of the three nanotubes as a function of the truncation length, showing the same convergence to zero electro-osmotic flow as in the rectangular cases. This zero-flow result is in agreement with our analytical theory for the cylindrical geometry. Comparison of our results for the planar and cylindrical cases show that the spurious flow effect is obtained irrespective of details of the geometry.

Nanotubes with reservoir. Identical to Ref. [60], we also simulate a (16,0) carbon nanotube of length 9.8 nm connecting two reservoirs as shown in Fig. 4.12 (a), to compare our results quantitatively to the results of Ref. [60]. We use a Nosé-Hoover thermostat and an anisotropic Parrinello-Rahman barostat. For each scheme and various r_c, we simulate for 5 ns and collect the last 3 ns for analysis while for $r_c = 1.0$ nm we extend the simulation time by 40 ns. The total size of the periodically repeated reservoir is $4.0 \times 3.6 \times 1.8$ nm. There are 1057 water molecules in the system.

To estimate the ζ-potential of the (16,0) CNT connecting two reservoirs, we calculate the flux in x_1 direction through a cross section located at one end of the nanotube. Note that our definition of the flux differs from the definition used in Ref. [60], see Sec. 4.3.5. The cumulative flux is shown as a function of time for both cut-off schemes in Fig. 4.12 (b), from which the flux is calculated using linear regression. The average velocity u_1 inside the nanotube is calculated by dividing the flux by the linear molecule density inside the nanotube, after which the ζ-potential is calculated from Eq. 4.1. The resulting ζ-potential is shown in Fig. 4.13 (b) as a function of the truncation length. Although the ζ-potential is smaller than when in absence of reservoirs, which has to do with the friction a water molecule encounters when entering or exiting the nanotube, again the results show

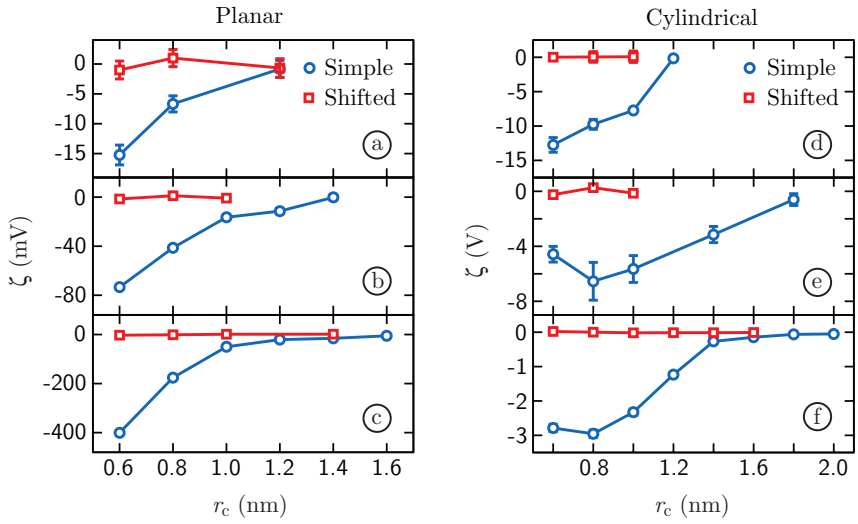

Figure 4.11: *Left: The ζ-potential of three planar systems,* (a) *an oil slab,* (b) *a hydrophobic diamond and* (c) *a graphene sheet in pure water as a function of the truncation length r_c, calculated from the velocity in the bulk region (see text). Right: The ζ-potential of three cylindrical systems,* (d) *a (10,0) carbon nanotube,* (e) *a (16,0) carbon nanotube and* (f) *a (16,16) carbon nanotube, calculated from the average velocity inside the tube.*

a striking yet unphysical difference between the cut-off schemes: For the simple cut-off at $r_c = 1.0$ nm we find an average flux of 22 ± 8 ns^{-1}, comparable to 34.0 ± 5.2 ns^{-1} from Ref. [60], while the shifted cut-off exhibits vanishing flux. In the limit $r_c \to \infty$, the spurious difference between the cut-off schemes disappears and the water flux vanishes, in accordance with the generalized hydrodynamic theory presented in the previous sections. We simulate exactly the same system of a (16,0) carbon nanotube between reservoirs using the alternative simulation package LAMMPS [156]. In LAMMPS, both the simple cut-off and the shifted cut-off as used in GROMACS are implemented. As shown in Fig. 4.13 (b), the flux vanishes, even for small r_c, regardless of the cut-off scheme. We conclude that electro-osmosis, *i.e.* the electric-field induced steady flow, of pure water in a carbon nanotube is a simulation artifact and related to the implementation of the cut-off scheme in GROMACS [145].

The effect of ions. We also simulate an artificial hydrophobic surface identical to the one used by Huang *et al.* [67, 141], solvated in 1 M sodium chloride. The surface consists of an FCC lattice of atoms with Lennard-Jones parameters $\epsilon_{\mathrm{FCC}} = 0.686$ kJ mol^{-1} and $\sigma_{\mathrm{FCC}} = 0.337$ nm and has a contact angle of 140°. The Lennard-Jones parameters of the ions are given by $\epsilon_{\mathrm{Na}} = 0.0617$ kJ mol^{-1} and $\sigma_{\mathrm{Na}} = 0.258$ nm for Na^+ and $\epsilon_{\mathrm{Cl}} = 0.446$ kJ mol^{-1} and $\sigma_{\mathrm{Cl}} = 0.445$ nm for Cl^-. The inter-plate distance corresponds to a pressure of 10 ± 5 bar [141].

As shown in Fig. 4.13 (a), the artificial hydrophobic surface has a non-zero ζ-potential. Huang *et al.* use a simple cut-off scheme with a truncation length of 1.0 nm and the LAMMPS simulation package, giving zero electro-osmotic flow. The fact that our simulations yield a non-zero ζ-potential using a simple cut-off scheme indicates that this is a GROMACS-related issue, and not due to the simple cut-off *per se*. Note that in simulations

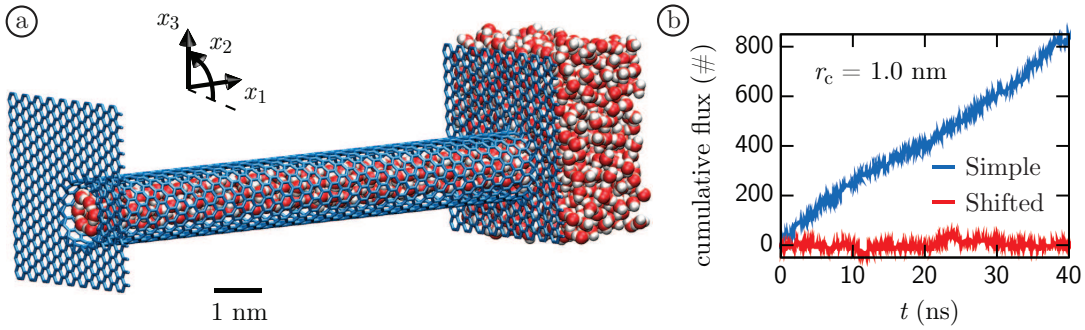

Figure 4.12: (a) *Snapshot of the (16,0) nanotube simulations with reservoir.* (b) *Cumulative flux through the tube as a function of time for an electric field strength of* 1 *V/nm for the two different Lennard-Jones cut-off schemes with* $r_c = 1.0$ *nm, simulated with* GROMACS. *For each cut-off length, the* ζ*-potential is calculated from the derivative of the cumulative flux as shown in* (b)*, the line density inside the tube and Eq. 4.1.*

of electrolyte solutions at neutral surfaces a small, but finite electrokinetic effect can exist in principle, because the sodium and chloride ions have slightly dissimilar surface affinities, giving rise to a small electrostatic surface potential. However, this small contribution is totally dominated by the erroneous flow generated within the simple cut-off scheme.

Zero-field flux. As a simple test of the effect of the electric field, we perform long simulations of a 9.8 nm long $(10, 0)$ nanotube between reservoirs with and without electric field. The results are shown in Fig. 4.14 for zero and non-zero external electric fields. Most strikingly, the flux is non-zero for the simple cut-off scheme, shown in Fig. 4.14 (b), regardless of whether an external electric field is applied or not. The same effect is in fact displayed in Fig. 1 of Ref. [60]. Again, in the shifted scheme this unphysical effect is absent. Since it is self-evident that in the absence of an electric field no flux should result, this proves our point most forcefully that something is fundamentally wrong with the simple cut-off scheme as implemented in GROMACS, leading to erroneous coupling between orientation and flux. The residual flux fluctuations for the shifted cut-off scheme shown in Fig. 4.14 (a) suggest that the simulations in the $(10, 0)$ nanotube have not converged on the time scale of 40 ns, which simply makes the $(10, 0)$ nanotube unsuited for studying equilibrium properties in general.

Point charges at carbon nanotubes. For a set of fixed point charges the electric field is spatially inhomogeneous. We simulate the system shown in Fig. 4.15 (a) for 5 ns, collect the last 3 ns for analysis and calculate the flux as a function of the cut-off length for the two different cut-off schemes. We use a Berendsen thermostat and update the neighbor list every 10 timesteps. We define the three negative charges next the to nanotube to be in one charge group and the three compensating positive charges in another (see below for further explanation). The differences between our system and the system used in Ref. [61] are that the charges next to our tube are negative, external charges and tube atoms are frozen, our tube is longer and our reservoir is larger. From the flux and the average number of particles per unit length we calculate the average velocity inside the tube, shown in Fig. 4.15 (b) as a function of the cut-off length for the two different truncation schemes. Clearly, the velocity depends on the cut-off length like in the case of a homogeneous electric

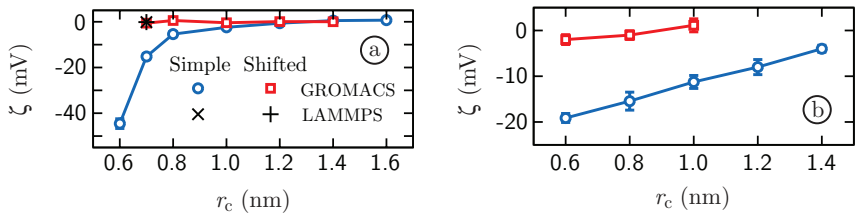

Figure 4.13: (a) *The ζ-potential of a (16,0) nanotube connecting two reservoirs as a function of the Lennard-Jones cut-off length, simulated with* GROMACS *(circles and squares), and simulated with* LAMMPS *(cross and plus), for both cut-off schemes. For each cut-off length, the ζ-potential is calculated from a linear fit to the cumulative flux, the line density inside the tube and Eq. 4.1.* (b) *The ζ-potential of an artificial hydrophobic surface (consisting of an* FCC *lattice of Lennard-Jones atoms) in the presence of a 1 M sodium chloride solution as a function of the truncation length r_c.*

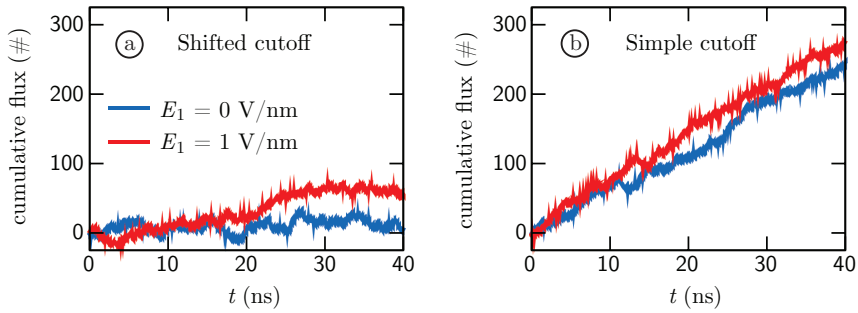

Figure 4.14: *Cumulative flux through a (10,0) carbon nanotube with (red lines, field strength 1 V/nm) and without (blue lines) external electric field. Cutoff schemes used are* (a) *shifted and* (b) *simple, both at r_c = 1.0 nm. The flux is calculated according to the unconditional definition (see Sec. 4.3.5 "Definition of Flux" in the text). The system size is* $3.0 \times 2.7 \times 13.7$ nm *containing* 1008 SPC/E *water molecules.*

field and simple cut-off. However, the velocity resulting from an inhomogeneous electric field also shows a cut-off length dependence for a shifted cut-off scheme. This shows that using a shifted cut-off scheme does not necessarily prevent the flow. Indeed, since there is nothing unphysical about the simple cut-off *per se*, we have no reason to believe that a shifted cut-off should perform better in any case; it is the numerical implementation of the cut-off scheme in GROMACS that produces questionable results.

Following a recent publication [157], we also investigate the effect of the use of charge groups. For a charge group, Coulomb interactions are calculated for all individual charges in the group, but the position of each individual charge is approximated by the geometrical mean of the constituent particles [158]. In the simulations by Ref. [61] and the simulations shown in Fig. 4.15 the fixed charges close to the nanotube are grouped within a single charge group. The artificial pumping disappears for both cut-off schemes even for a short cut-off length of 0.7 nm if we do not use a charge group for the fixed external charges. This confirms the findings of Ref. [157]. Finally, using the alternative simulation package NAMD 2, the directional flux vanishes altogether [159].

Nanoscale pumping of water by AC electric fields. Contrary to static electric fields, time-dependent electric fields can in principle be used to drive a system without free

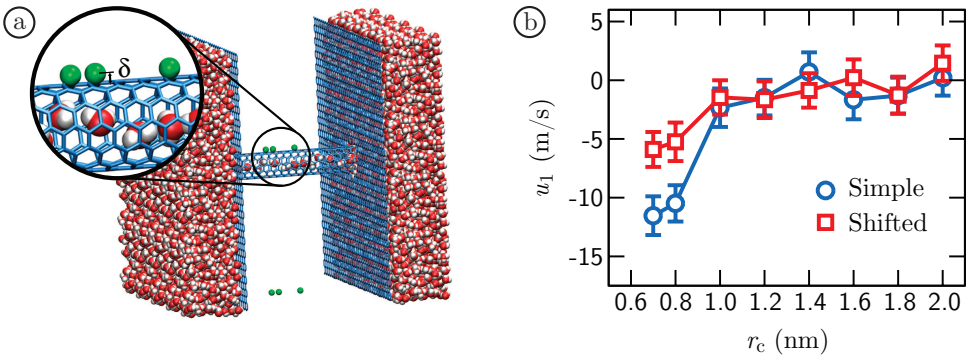

Figure 4.15: (a) *Snapshot of the (10,0) nanotube with fixed negative charges. The charges are located at* 1.92 *nm,* 2.64 *nm and* 2.88 *nm distance from the right end of the tube and the distance between the charges and the nanotube is* $\delta = 0.093$ *nm. Charges are -0.5, -0.5 and -1 e from left to right, with charges of opposite sign at the bottom of the box for compensation. The system size is* $8.8 \times 8.4 \times 8.8$*, the tube length is* 4.8 *nm and the system contains* 8389 TIP3P *water molecules. The neighbor list is updated every* 10 *timesteps of* 2 *fs each.* (b) *Dependence of the average axial velocity* u_1 *inside the nanotube on the cut-off length* r_c *for the two different cut-off schemes.*

charges, as we have shown in Sec. 4.2. Using MD simulations, we demonstrate pumping of water through a carbon nanotube (CNT), employing a periodic array of oscillating point charges attached to the outside of the CNT [160]. The oscillating charges generate a running electromagnetic wave, which induces flow through two distinct mechanisms: dipole rotation (as discussed in Sec. 4.2) and polarization-dragging. The latter hinges upon the force exerted on a dipole moment by the first spatial derivative of the electric field, and is found to dominate over the dipole rotation mechanism in this case. We refer to Ref. [iv] for details.

4.3.4 Dependence of the Flow Velocity on Other Simulation Parameters

For inhomogeneous electric fields resulting from a set of point charges, there are a few additional simulation settings that may influence the resulting water dynamics [157]. To speed up the simulation, each molecule carries a list of molecules with which it has significant interaction, the so-called neighbor list. Reducing the update frequency of this list speeds up the calculation, while increasing the risk of inaccuracies. In Fig. 4.16 (a) we show the ζ-potential of a planar hydrophobic diamond (double face-centered cubic lattice of C-atoms, contact angle $\theta = 111°$) in a homogeneous electric field as a function of the number of steps between neighbor list updates (*nstlist*). The Lennard-Jones simple cut-off is set to $r_c = 0.8$ nm. A value of $nstlist = 1$ means the list is updated every step. From Fig. 4.16 (a), we conclude that for a spatially constant electric field the neighbor list update frequency does not have a significant influence on the ζ-potential of the solute.

In case of numerical artifacts, a dependence on the size of the integration time step may be expected as well. In Fig. 4.16 (b), the spurious ζ-potential of a hydrophobic diamond is shown as a function of the integration time step for $r_c = 0.8$ nm. Larger time steps than 2 fs are not possible because of the fast dynamics of the hydrogen atoms. The flow dynamics do not depend significantly on the integration time step, showing that the problem is not related to integration accuracy.

Like any flow, the magnitude of the spurious flow depends strongly on the particularities

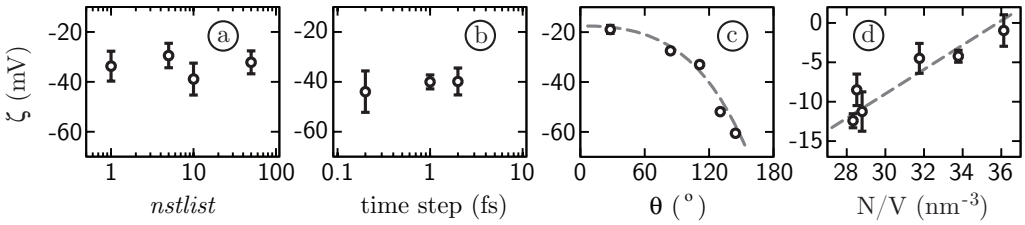

Figure 4.16: (a) *Dependence of the spurious ζ-potential of a hydrophobic diamond (contact angle of* 111°*) on the number of steps between neighbor list updates (nstlist) using a timestep of* 1 *fs and* (b) *dependence on the integration time step using nstlist* = 50. (c) *The ζ-potential of a diamond surface as a function of contact angle and* (d) *the ζ potential of an artificial hydrophobic surface (θ* = 140°*) with* 1 *M* NaCl *as a function of the molecular water density N/V, using a timestep of* 1 *fs and neighbor list update frequency of* 1/50 *timesteps. Dashed lines are drawn as a guide to the eye. We use a simple Lennard-Jones cut-off at* $r_c = 0.8$ *nm* (a-c) *and* $r_c = 1.0$ *nm* (d). *The electric field strength is* 0.4 *V/nm* (a-d) *and the system size in* (a-c) *is* $3.2 \times 3.2 \times 4.7$ *nm containing* 928 SPC/E *water molecules and one diamond. System size in* (d) *is* $3.9 \times 3.9 \times 16.4$ *nm, containing* 2052 SPC/E *water,* 40 Na^+ *and* 40 Cl^- *molecules confined between two slabs.*

of the system, most notably the contact angle of the substrate and the pressure in the system. In Fig. 4.16 (c) we show the ζ-potential of the diamond surface in contact with pure water. The contact angle of the diamond is modified by adjusting the Lennard-Jones interaction strength ϵ between the carbon atoms and the water molecules. For each simulation system, the contact angle is determined from the virial according to the method employed by Ref. [128]. All simulations are done using a simple cut-off truncation scheme and a truncation length of $r_c = 0.8$ nm. Using shifted truncation, the electro-osmotic flow is zero for any contact angle. Shown in Fig. 4.16 (d) is the ζ-potential of an artificial single face-centered cubic lattice (Lennard-Jones parameters $\epsilon_{\text{FCC}} = 0.686$ kJ/mol, $\sigma_{\text{FCC}} = 0.337$ nm, $\theta = 140°$) in a solution of 1 M NaCl in water as a function of the average number density of water $N/\mathcal{V}$ in the volume between the plates. Calculating the pressure from the force on the center of mass of each plate divided by the plate area gives a pressure of 1 bar at an average density of 29 nm^{-3}. We use a simple cut-off scheme for the Lennard Jones interaction with a truncation length of 1.0 nm. The apparent ζ-potential decreases with increasing density. We note that the dependence of the ζ-potential on the surface contact angle and the water density shown in Fig. 4.16 are spurious, in the sense that the electro-osmotic flow should vanish altogether in this case. This is also true for the salt solution, since the cations and anions of NaCl show almost the same adsorption affinities on a hydrophobic surface. Fig. 4.16 does show, however, that the magnitude of the artifact varies appreciably depending on the particularities of the system, and that the spurious flow is most pronounced for hydrophobic systems with a low average density of water molecules, a class of systems to which carbon nanotubes belong as well.

4.3.5 Definition of Flux

In the first paper on water in carbon nanotubes, Hummer *et al.* found that the filling of nanotubes goes in bursts [43]. This bursting behavior seems manifest also in simulation trajectories of Ref. [60], particularly in the (10,0) nanotube. Let us discuss the way bursts in the cumulative flux emerge in the original analysis of Ref. [60]. Due to conservation of mass, the average flux through a given cross section of the carbon nanotube does not

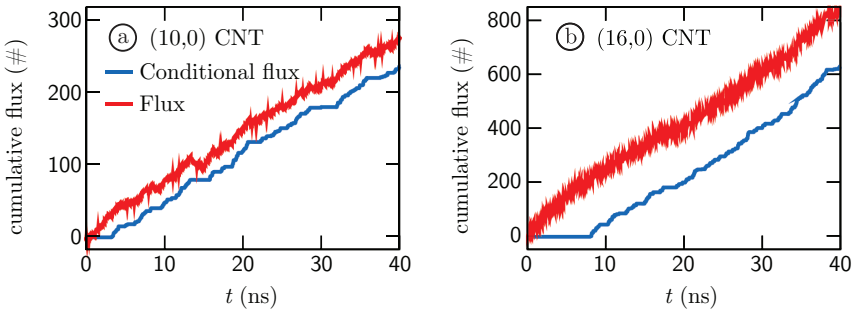

Figure 4.17: *Axial flux (x_1 direction) through a (10,0) nanotube* (a) *and a (16,0) nanotube* (b) *at $E_1 = 1.0$ V nm^{-1} using simple cut-off at $r_c = 1$ nm. Shown in red is the flux calculated using the straightforward counting of molecules, shown in blue is the conditional flux, where molecules exiting the tube are counted only if they previously entered from the other side. Simulation boxes are identical to the ones described in Figs. 4.13 and 4.14. We use a time step of* 1 *fs and neighbor list update every* 50 *steps.*

depend on the position of the cross section. Therefore, without restricting the generality of our arguments, we define the flux as the number of water molecules passing the edge of the simulation box. This we call the *cumulative flux*. In Ref. [60], on the other hand, the flux is defined as the number of particles exiting the tube on one end that have previously entered on the other end. This definition we denote as the *conditional cumulative flux* and it implicitly contains a tube length dependence. We perform simulations of 40 ns with a 5 ns equilibration period using a 1.0 nm simple cut-off scheme and an electric field of 1 V/nm. In Fig. 4.17 (a – b) we show the results for two tube diameters, (10,0) and (16,0) respectively, both connecting two reservoirs. The results have been analyzed using both the straightforward counting of molecules passing the edge of the box (denoted as flux), and using the definition from Ref. [60] (denoted as conditional flux). For long times, both definitions of the flux converge to the same value but for shorter times, there are distinct differences. The first, obvious effect of the conditional definition of the flux is that the first particles exiting the tube, which are the particles that were located in the tube from the start, do not contribute to the conditional flux since they did not previously enter the tube. This explains the initial $4-8$ ns waiting time and suggests that using the conditional definition of the flux is not very efficient in terms of computer time. The second effect is a suppression of noise: particles moving back and forth are only counted if their motion persists for the full tube length. This explains the striking lack of noise in the results shown in Ref. [60], as well as a large part of the alleged bursting behavior. From the unconditional flux, the bursting is by far not as pronounced as in the filling curves from Hummer *et al.* [43].

4.4 Summary & Conclusions

Using a combination of analytical theory based on a generalized Navier-Stokes equation and molecular dynamics simulations, we show that interfacial water ordering does not give rise to steady-state flow in static electric fields. This means that the interfacial dipole potential due to the water ordering does not contribute to the ζ-potential. Nevertheless, electro-hydraulic pumping of dipolar fluids is possible: an electric field step function gives

rise to transient flow, while a rotating electric field in an asymmetric channel can be used to drive flows in steady state. In a symmetric channel, a rotating electric field induces a shear profile, but no net pumping. An electric field in the shape of a traveling wave, produced by phase-shifted AC voltages applied to an array of external electrodes, can also be used to drive pure water through a carbon nanotube. The equilibrium flow observed with static electric fields in previous molecular dynamics simulations of pure water, however, were caused by particularities of the simple Lennard Jones force truncation scheme in GROMACS. The unphysical dependence of the flow velocity on the Lennard-Jones truncation scheme vanishes for truncation length $r_c \to \infty$ for all simulated geometries and surfaces. Using a shifted Lennard-Jones truncation scheme within GROMACS, pure water does not give rise to a non-zero ζ-potential for any value of the truncation length, in agreement with the analytical theory presented. Using the LAMMPS molecular dynamics package, the spurious flow effect is not observed, regardless of the truncation scheme used. Small values of the truncation length also lead to spurious flow in the presence of the static inhomogeneous electric field produced by fixed charged outside a carbon nanotube. In contrast with the situation for homogeneous electric fields, the spurious flow persists when using a shifted truncation scheme, vanishing only for large values of the truncation length. We conclude that the spurious flow observed in molecular dynamics simulations of both planar and cylindrical geometries is an implementation-related issue in GROMACS, and not caused by the use of truncation schemes *per se*.

Chapter 5

Electro-Osmotic Mobility and Electric Surface Conductivity

We calculate the electro-osmotic mobility and surface conductivity at a solid-liquid interface from a modified Poisson-Boltzmann equation, including spatial variations of the dielectric function and the viscosity that where extracted previously from molecular dynamics simulations of aqueous interfaces. The low-dielectric region directly at the interface leads to a substantially reduced surface capacitance. At the same time, ions accumulate into a highly condensed interfacial layer, leading to the well-known saturation of the electro-osmotic mobility at large surface charge density regardless of the hydrodynamic boundary conditions. The experimentally well-established apparent excess surface conductivity follows from our model for all hydrodynamic boundary conditions without additional assumptions. Our theory fits multiple published sets of experimental data on hydrophilic and hydrophobic surfaces with striking accuracy, using the non-electrostatic ion-surface interaction as the only fitting parameter. This chapter is based on Ref. [ii].

5.1 Introduction

When immersed in water, particles typically acquire a net surface charge, which is compensated for by a cloud of counterions in solution. This surface charge usually dominates the interactions between particles in colloidal suspensions. The bare surface charge density can be measured using charge titration [161]. It is well established, however, that the bare surface charge density cannot be used directly in classical models to describe dynamic properties of colloidal suspensions, such as coagulation kinetics, electro-osmotic mobility and effective viscosity [80, 162–164]. Instead, the ions and water molecules within a few molecular diameters from the surfaces of the colloidal particles decisively affect the suspension's macroscopic kinetic behavior. A deep understanding of the relation between bare surface charge, electro-osmotic mobility and the closely related phenomenon of surface conductivity is of supreme importance in many areas of physical chemistry. For instance, electrophoresis is commonly used in modern-day biochemistry for separation of chemicals based on minute differences in surface properties [165]. Furthermore, electrokinetic driving is the method of choice to generate flow in microfluidic devices [2, 3], which are becoming

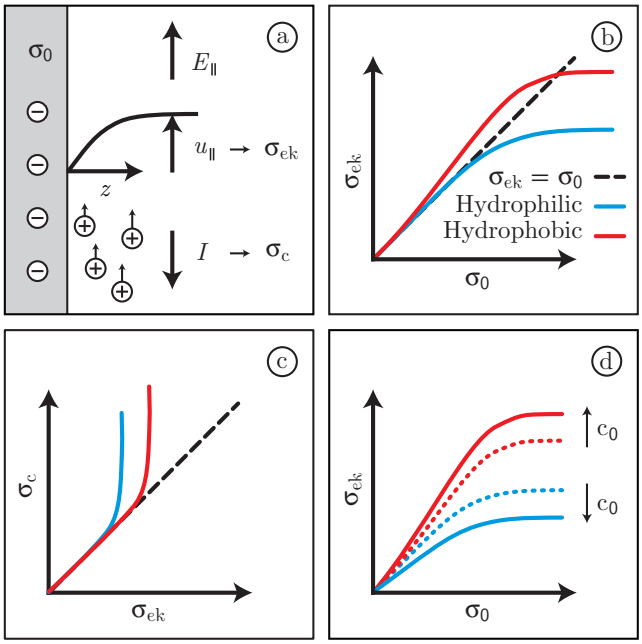

Figure 5.1: *Sketch of the basic model and general features of experimental data.* (a) *An electric field $E_\parallel$ parallel to a surface with bare charge density σ_0 produces an electro-osmotic flow profile $u_\parallel(z)$, from which the electrokinetic surface charge density σ_{ek} is calculated. The conductive surface charge density σ_c is calculated from the electric current I in response to $E_\parallel$.* (b) *σ_{ek} is experimentally found to saturate as a function of σ_0; saturation occurs at higher values for hydrophobic surfaces than for hydrophilic surfaces.* (c) *σ_c exceeds σ_{ek} at all surface types.* (d) *When the bulk salt concentration c_0 is raised, σ_{ek} increases at hydrophobic surfaces, and decreases at hydrophilic surfaces.*

ever more popular tools for biochemical analysis and clinical pathology. On a much larger scale, seismic activity in water-saturated soil produces electrokinetic signals, which are found to precede large earthquakes [166] and can be exploited for seismic imaging of the sub-surface [167]. Finally, the electrostatic and hydrodynamic properties of the colloid-water interface determine the stability of colloidal systems [168, 169], which is a crucial factor in many branches of chemical industry, such as food, water purification, pharmaceuticals, paints, and ceramics. To comprehend and control the macroscopic behavior of each of these systems, detailed knowledge of the hydrodynamic and electrostatic properties of the interfacial molecular layers is indispensable. Despite the immense practical and fundamental interest, however, the effect of these microscopic properties on macroscopic kinetics is poorly understood.

Electrokinetic measurements in controlled environments are a particularly sensitive tool to assess the dynamic properties of interfacial layers. The basic model for an electrolyte in contact with a surface carrying an immobilized bare surface charge density σ_0 is sketched in Fig. 5.1 (a). Driven by a tangential electric field $E_\parallel$, counterions move along the surface, dragging water molecules along. This electro-osmotic flow profile $u_\parallel(z)$ can be used to estimate the "electrokinetically active" surface charge density σ_{ek}, using the Gouy-Chapman model and the Stokes equation with a no-slip boundary condition. At the same time, the electric conductivity of the interfacial fluid is higher than the bulk conductivity due to the presence of counterions [170, 171], to an extent that is usually expressed by the

Dukhin number [172]. In conjunction with a suitable model, this surface conductivity can be used as an alternative way of estimating the surface charge density [132], leading to the conductive surface charge density σ_c. Clearly, the precise values of σ_{ek} and σ_c are highly model-dependent, and typically, σ_0, σ_{ek} and σ_c do not agree. As a specific numerical example, we consider silica nanochannels, where measuring the electrokinetic surface charge density using the streaming current at low salt concentration gives $\sigma_{ek} = -4$ mC/m^2 [173]. Calculating the conductive surface charge density in the same type of channels from measurements of the electric conductance, on the other hand, yields $\sigma_c = -50$ mC/m^2 [132], whereas the literature value for the bare charge density of silica, calculated from titration at a bulk salt concentration of 1 mM, is even higher: $\sigma_0 = -100$ mC/m^2 [174]. This example shows that the discrepancies mentioned are not small corrections, but major effects. In particular, three puzzling, but universal experimental trends have impeded the advancement of colloidal science in the past. First, the electrokinetic surface charge density σ_{ek} is found to saturate as a function of the bare surface charge density σ_0, independent of surface roughness or polarity [80, 175, 176], see the sketch in Fig. 5.1 (b). Traditionally, this issue has been rationalized using the inhomogeneity of the viscosity at the interface [176]. Assuming a hydrodynamically stagnant interfacial water layer, the calculated electrokinetic surface charge density σ_{ek} is found to agree with experiments [175]. Using this model on hydrophobic interfaces, however, where the fluid is known to slip along the surface (see Chapter 3), the electrokinetic surface charge density σ_{ek} exceeds the bare surface charge density σ_0, contrary to experimental evidence. Second, the conductive surface charge density σ_c is found to exceed the electrokinetic surface charge density σ_{ek} [130, 132, 173, 177–180], see Fig. 5.1 (c). This excess surface conductivity is referred to as *anomalous surface conduction*, and is found for all systems, independent of surface composition [179–181]. Traditionally, the excess surface conductivity is rationalized by the awkward assumption that ions in the hydrodynamically stagnant layer still conduct charge [80, 172, 179, 180, 182–185], which is clearly at odds with physical intuition. Third, whereas the electrokinetic surface charge density σ_{ek} increases with increasing bulk salt concentration c_0 at hydrophobic surfaces, such as silver iodide, it decreases at hydrophilic surfaces, such as titanium oxide and iron oxide-hydroxide [80, 175], see Fig. 5.1 (d).

Whereas the interfacial viscosity has been widely used to rationalize and model the experimental results described above, the interfacial dielectric function has not been taken into account up to now. In this paper, we include the variation of the dielectric function, which has been shown to work well in the description of interfacial capacitance [88], as well as the variation of the viscosity at the interface on the mean-field level. Including a low-dielectric layer at the surface leads to accumulation of counterion charge close to the interface, thereby reducing the electro-osmotic flow independent of the hydrodynamic boundary conditions. The relation between counterion condensation enhancement and saturation of the electrophoretic mobility has been established earlier for branched polymeric particles of roughly spherical shape [186]. In contrast, the surface conductivity is affected less by the ion condensation, explaining the discrepancies between the bare, conductive and electrokinetic surface charge densities.

5.2 Mobility and Conductivity

We consider a charged planar surface in contact with water, having translational invariance in the x and y directions. The dielectric tensor, the viscosity, the electric field and the

displacement field only depend on the perpendicular coordinate z.

5.2.1 Electrokinetic Surface Charge Density

For laminar flows, the electro-osmotic flow velocity profile $u_{\parallel}(z)$ in response to a parallel electric field $E_{\parallel}$ is calculated from the Stokes equation,

$$\nabla\eta(z)\,\nabla u_{\parallel}(z) = -\rho(z)\,E_{\parallel}, \tag{5.1}$$

with spatially varying viscosity $\eta(z)$ and charge density $\rho(z)$. Note that $\rho(z)$ is the ionic charge density and polarization charges do not enter the force balance, as shown earlier [187]. The hydrodynamic boundary condition of either slip or a high-viscosity layer is taken into account via the viscosity profile $\eta(z)$, which in conjunction with the condition $u_{\parallel}(0) = 0$ is designed to reproduce the flow profile at macroscopic distances from the interface, as will be elaborated later. The electro-osmotic mobility is found by integrating Eq. 5.1 twice using $u_{\parallel}(0) = 0$ as a boundary condition,

$$\frac{u_{\parallel}(z)}{E_{\parallel}} = -\int_0^z \frac{D_{\perp}(z')}{\eta(z')}\,\mathrm{d}z', \tag{5.2}$$

with $D_{\perp}(z)$ being the displacement field perpendicular to the surface, which obeys Gauss's law, $\nabla D_{\perp}(z) = \rho(z)$. Experimentally, electro-osmotic velocity is measured far away from the interface. Assuming that the permittivity is spatially constant and equal to its bulk value ε_{bulk}, and $\eta(z) = \eta_{bulk}$ in Eq. 5.2, the electro-osmotic mobility is given by the Helmholtz-Smoluchowski equation,

$$\lim_{z\to\infty} \frac{u_{\parallel}(z)}{E_{\parallel}} = -\frac{\varepsilon_0\varepsilon_{bulk}}{\eta_{bulk}}\,\zeta, \tag{5.3}$$

with $\zeta = \int_0^{\infty} \left(D_{\perp}(z)/\varepsilon_0\varepsilon_{bulk}\right)\mathrm{d}z$ being the electrostatic potential at $z = 0$. A derivation of Eq. 5.3 is given in Appendix B. Because the surface potential is typically not measured directly, it is often more convenient to express ζ in terms of the equivalent surface charge density. Using the standard Poisson-Boltzmann relation between the surface potential and the surface charge density, which is valid on the mean-field level, the electro-osmotic mobility of Eq. 5.2 is expressed as an equivalent surface charge density, referred to as the electrokinetic surface charge density σ_{ek},

$$\sigma_{ek} = \sqrt{\frac{8c_0\varepsilon_0\varepsilon_{bulk}}{\beta}}\,\sinh\left[\frac{\beta e\,\zeta}{2}\right], \tag{5.4}$$

with c_0 the bulk salt concentration. Eq. 5.4 is known as the Grahame equation. The ζ-potential is calculated using Eq. 5.3, where the electro-osmotic mobility is either measured experimentally or calculated from Eq. 5.2. A derivation of Eq. 5.4 is given in Appendix B.

5.2.2 Conductive Surface Charge Density

The electric conductivity close to charged surfaces is enhanced with respect to the bulk due to the presence of excess ionic charges. This surface conductivity can be conveniently measured in small channels at low salt concentration, in which case the contribution from

the bulk vanishes [132]. The surface conductivity is given by the sum of a convective part, due to the electro-osmotic flow, and a conductive part, due to the electrophoretic mobility of the ions,

$$\begin{aligned}\frac{I}{E_{\parallel}} = &\int_0^{\infty} e\big[c_+(z) - c_-(z)\big]\left[u_{\parallel}(z)/E_{\parallel}\right]\mathrm{d}z \\ &+ \int_0^{\infty} e\big[\nu_+(c_+(z) - c_0) + \nu_-(c_-(z) - c_0)\big]\mathrm{d}z,\end{aligned} \tag{5.5}$$

with $\nu_{\pm}$ the electrophoretic mobility of the positive and negative ions. Note that we subtract the bulk contribution to the conductive part of Eq. 5.5. Similar to the Grahame equation (Eq. 5.4), the surface conductivity can be expressed as an equivalent surface charge density using the Gouy-Chapman theory, giving

$$\sigma_c = \frac{\kappa^2\eta_{bulk}}{4ec_0 + \nu\kappa^2\eta_{bulk}}\sqrt{\frac{I}{E_{\parallel}}}\sqrt{\frac{I}{E_{\parallel}} + \frac{32e^2c_0^2}{\kappa^3\eta_{bulk}} + \frac{8ec_0\nu}{\kappa}}. \tag{5.6}$$

A derivation of Eq. 5.6 is given in Appendix B. Since the predominant salt types being considered in the experiments that we compare our results with (Sec. 5.5.2) are K^+ ($\nu_+ = 7.62 \times 10^{-8}$ m^2/Vs), Cl^- ($\nu_- = 7.91 \times 10^{-8}$ m^2/Vs) and NO_3^- ($\nu_- = 7.40 \times 10^{-8}$ m^2/Vs), we assume $\nu_+ = \nu_- = \nu$, which is a good approximation for both KCl and $\mathrm{KNO_3}$.

5.3 Viscosity & Dielectric Profile

Viscosity profile. We model the variations in viscosity at the interface by a step function,

$$\eta(z) = \begin{cases} \eta_i & \text{if } z < z_s \\ \eta_{bulk} & \text{otherwise,} \end{cases} \tag{5.7}$$

with η_i the viscosity in a layer of width z_s and η_{bulk} the bulk viscosity. Note that the definition of a viscosity at sub-atomic length scales is problematic, and the profile of Eq. 5.7 is only intended to reproduce, within a continuum model, the flow characteristics found experimentally at distances $z > z_s$. For most hydrophobic surfaces the fluid slips along the wall [36], which is commonly taken into account by the Navier hydrodynamic boundary condition, $b\nabla u_{\parallel}(z)\,|_0 = u_{\parallel}(z)\,|_0$, with positive slip length b. In simulations of water at a very hydrophobic diamond surface, the viscosity is found to be constant and equal to the bulk value η_{bulk} for $z > 0.15$ nm, leading to a slip length of $b = 2.15$ nm. Setting $u_{\parallel}(0) = 0$, we reproduce the same flow profile for $z > z_s$ by assigning $\eta_i = \eta_{bulk}/15$ and $z_s = 0.15$ nm. For most hydrophilic surfaces, on the other hand, the fluid in the first molecular layer adjacent to the wall sticks to the surface [36]. Molecular dynamics simulation on smooth hydrophilic surfaces have shown that the interfacial layer is not truly stagnant, it merely has an enhanced viscosity [74, 125]. Following the simulation results of Ref. [74] we take $z_s = 0.3$ nm and $\eta_i = 3\eta_{bulk}$. In Fig. 5.2 (a), we show the viscosity profile $\eta(z)$ of Eq. 5.7 at hydrophilic and very hydrophobic surfaces. For easy reference, we characterize each viscosity profile by its apparent slip length,

$$b = z_s\left(\eta_{bulk}/\eta_i - 1\right). \tag{5.8}$$

Electrophoretic mobility. In general, the electrophoretic mobility of ions $\nu_{\pm}$ depends on the ion concentration and the viscosity of the fluid [188]. The ion mobility directly at

the interface is not known (note that the conclusion that the interfacial mobility equals the bulk mobility [182] relies heavily on the electrostatic model used). Here, we use the simplest approach, where only the bulk-like viscous drag on the ions is taken into account, resulting in a mobility that is inversely proportional to the local viscosity.

Dielectric profile. In order to describe the dielectric profile at a similarly simplistic level as the viscosity, we use a step function as well,

$$\varepsilon_\perp(z) = \begin{cases} 1 & \text{if } z < z_\perp^{\mathrm{DDS}} \\ \varepsilon_{bulk} & \text{otherwise,} \end{cases} \tag{5.9}$$

with $z_\perp^{\mathrm{DDS}}$ the dielectric dividing surface as defined in Sec. 2.4.1 [88]. The profile in Eq. 5.9 is designed to reproduce the electrostatic potential calculated in molecular dynamics simulations at positions $z \gtrsim 1$ nm from the interface [88]. For $z_\perp^{\mathrm{DDS}}$ we use two different values: $z_\perp^{\mathrm{DDS}} = 0.10$ nm, corresponding to a hydrophilic surface, and $z_\perp^{\mathrm{DDS}} = 0.12$ nm, corresponding to a very hydrophobic surface, as directly taken from Sec. 2.4.1. The inverse dielectric profiles $\varepsilon_\perp^{-1}(z)$ in the approximation of Eq. 5.9 are shown in Fig. 5.2 (b) for hydrophilic and very hydrophobic surfaces.

5.4 Scaling Analysis

In this section, we qualitatively investigate how the dielectric profile $\varepsilon_\perp(z)$ as given in Eq. 5.9 affects the counterion distribution, and consequently σ_{ek} and σ_c.

Counterions at a charged plate. The electrokinetic and conductive surface charge densities defined in Eqs. 5.4 and 5.6 are directly affected by the viscosity profile $\eta(z)$. The dielectric profile $\varepsilon_\perp(z)$ does not affect σ_{ek} and σ_c directly, but it does have a decisive influence on the ion distribution, which in turn has a major impact on σ_{ek} and σ_c. For a qualitative picture of the effect of $\varepsilon_\perp(z)$, we consider the situation of an infinite charged plate in contact with a solution containing only counterions. We keep the viscosity constant, $\eta(z) = \eta_{bulk}$. According to the Gouy-Chapman model, the ions form a diffuse layer when $\varepsilon_\perp(z) = \varepsilon_{bulk}$, and by definition $\sigma_{ek} = \sigma_c = \sigma_0$. This relation is also valid in the limit of low salt concentration ($c_0 \to 0$), in which case the solution contains only counterions. Using the profile of Eq. 5.9, on the other hand, a large portion of the ions will condense into the low-dielectric area because of the steep increase of the electric potential resulting from the low dielectric constant. This model of a low-dielectric layer of condensed ions has been proposed long ago by Otto Stern based on experimental double-layer capacitance data [22], and we have confirmed in Sec. 2.4.3 that Eq. 5.9 in conjunction with a mean-field model indeed reproduces the salt-concentration dependence of the double-layer capacitance [88]. In our present scaling analysis, we use a delta function as a model for the charge distribution to mimic the condensed layer of ions,

$$\rho(z) = -\sigma_0 \delta(z - d), \tag{5.10}$$

with d the typical distance to the surface. A typical value of d would be the radius of an ion. The electrophoretic mobility of Eq. 5.2 is integrated by parts, which leads to

$$\zeta = -\frac{1}{\varepsilon_0 \varepsilon_{bulk}} \int_0^\infty z\, \rho(z)\, \mathrm{d}z, \tag{5.11}$$

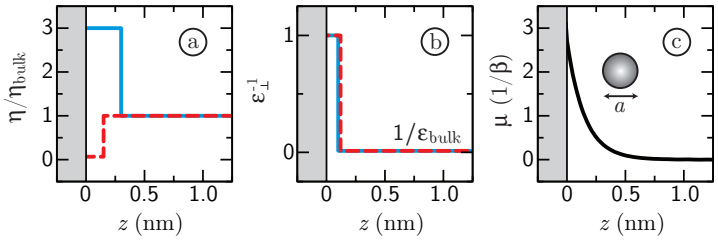

Figure 5.2: (a) *Normalized viscosity profile (Eq. 5.7).* (b) *Inverse dielectric profile* $\varepsilon_\perp^{-1}(z)$ *(Eq. 5.9).* (c) *Non-electrostatic potential* $\mu_\pm(z)$ *(Eq. 5.21) with* $\alpha = 1$. *Also shown is an ion with diameter* a.

using the definition of ζ given in Eq. 5.3. Inserting Eq. 5.10 into Eq. 5.11 gives

$$\zeta = \frac{\sigma_0\, d}{\varepsilon_0 \varepsilon_{bulk}} \tag{5.12}$$

which scales linearly with σ_0 for a given distance d. The behavior of σ_{ek}, defined by Eq. 5.4 and using Eq. 5.12, as a function of σ_0 depends on how d behaves as a function of σ_0.

To calculate the conductivity we insert Eq. 5.10 into Eq. 5.5,

$$\frac{I}{E_\parallel} = \int_0^\infty \left(-\sigma_0 \frac{u_\parallel(z)}{E_\parallel} + \nu|\sigma_0| \right) \delta(z-d)\, \mathrm{d}z. \tag{5.13}$$

The flow velocity at $z = d$ turns out to be $u_\parallel(d) = -E_\parallel \sigma_0 d/2\eta_{bulk}$, from which the conductivity follows as

$$\frac{I}{E_\parallel} = \frac{\sigma_0^2\, d}{2\eta_{bulk}} + \nu|\sigma_0|. \tag{5.14}$$

Contrary to the electro-osmotic mobility, which depends linearly on σ_0, the conductivity scales with σ_0^2. That means that the conductive surface charge density σ_c will exceed the electrokinetic surface charge density σ_{ek} for large σ_0 (provided d does not become infinitesimally small), which rationalizes the experimentally measured excess surface conductivity that is sketched in Fig. 5.1 (c). The analysis above shows that the so-called *anomalous surface conduction* follows naturally from the standard dynamic equations when the double-layer width deviates from the standard mean-field prediction for a uniform dielectric constant.

5.5 Modified Poisson-Boltzmann Equation

To quantitatively examine the electrokinetic and conductive surface charge densities σ_{ek} and σ_c as a function of the bare surface charge density σ_0, we solve the Poisson-Boltzmann equation in conjunction with the Stokes equation (Eq. 5.1) using the dielectric profile of Eq. 5.9 and the viscosity profile of Eq. 5.7.

Modified Poisson-Boltzmann equation. We assume that the electric field is linearly related to the displacement field by the local inverse dielectric tensor $\varepsilon_\perp^{-1}(z)$,

$$\varepsilon_0 E_\perp(z) = \varepsilon_\perp^{-1}(z)\, D_\perp(z), \tag{5.15}$$

where $\perp$ indicates the component perpendicular to the interface. Eq. 5.15 is a good approximation in case of a slowly varying $D_\perp(z)$ [24, 88]. Taking the derivative of Eq. 5.15 and using $\nabla\psi(z) = -E_\perp(z)$, with $\psi(z)$ the electrostatic potential, and $\nabla D_\perp(z) = \rho(z)$, with $\rho(z)$ the ionic charge density, we arrive at the modified Poisson equation

$$\varepsilon_0 \nabla^2 \psi(z) = \varepsilon_\perp^{-1}(z)\,\rho(z) - D_\perp(z)\,\nabla\varepsilon_\perp^{-1}(z)\,. \tag{5.16}$$

The displacement field $D_\perp(z)$ is given by

$$D_\perp(z) = \int_0^z \rho\left(z'\right) \mathrm{d}z'. \tag{5.17}$$

Eqs. 5.16 and 5.17 constitute an integro-differential equation [33]. We consider a solution of monovalent ions. The free charge density is calculated from the ionic densities $c_+(z)$ and $c_-(z)$,

$$\rho(z) = e\left(c_+(z) - c_-(z)\right), \tag{5.18}$$

with e being the absolute charge of an electron. To ensure that the ionic density does not exceed its physical limit set by the ionic volume, we include a fermionic steric interaction to calculate the ionic densities from the unrestricted ionic densities $\tilde{c}_+(z)$ and $\tilde{c}_-(z)$ [189–192],

$$c_\pm(z) = \frac{\sqrt{2}\,\tilde{c}_\pm(z)}{\sqrt{2} + a_+^3\left(\tilde{c}_+(z) - c_0\right) + a_-^3\left(\tilde{c}_-(z) - c_0\right)}, \tag{5.19}$$

with c_0 being the bulk salt concentration and a_+ and a_- being the diameters of positive and negative ions respectively. The denominator in Eq. 5.19 restricts the maximum density $c_\pm(z)$ to $\sqrt{2}\,a_\pm^{-3}$, which is the maximum density of close-packed (face-centered cubic or hexagonal close-packed) spheres of diameter $a_\pm$. The unrestricted ionic densities $\tilde{c}_+(z)$ and $\tilde{c}_-(z)$ follow the Boltzmann distribution

$$\tilde{c}_\pm(z) = c_0 \exp\left[-\mu_\pm(z) \mp \beta e \psi(z)\right], \tag{5.20}$$

with β being the inverse thermal energy and $\mu_+(z)$ and $\mu_-(z)$ being the non-electrostatic contributions to the potential of the positive and negative ions respectively. Combining Eqs. 5.16, 5.17, 5.18, 5.19 and 5.20 yields the modified Poisson-Boltzmann equation.

Non-electrostatic potential. For the non-electrostatic potential $\mu_\pm(z)$, we use a heuristic function of the form

$$\mu_\pm(z) = \alpha \exp\left[1 - 2z/a_\pm\right]. \tag{5.21}$$

The dependence of the non-electrostatic potential on the surface and ion type is parameterized by the ion diameter $a_\pm$ and the interaction strength α. In Fig. 5.2 (c), we show the non-electrostatic potential of Eq. 5.21 with $\alpha = 1$, together with a sketch of an ion with diameter a. We first set $\alpha = 0$ to show the trends of σ_{ek} and σ_c and then use α as a fit parameter to compare with experimental data.

Volume fraction. Because it better reflects the distribution of the ions than the density of point charges, we plot the fraction $\varphi_\pm(z)$ of the volume occupied by ions, calculated by convolution of the point charge density with the molecular volume $v_\pm(z)$,

$$\varphi_\pm(z) = \int c_\pm\left(z'\right) v_\pm\left(z - z'\right) \mathrm{d}z', \tag{5.22}$$

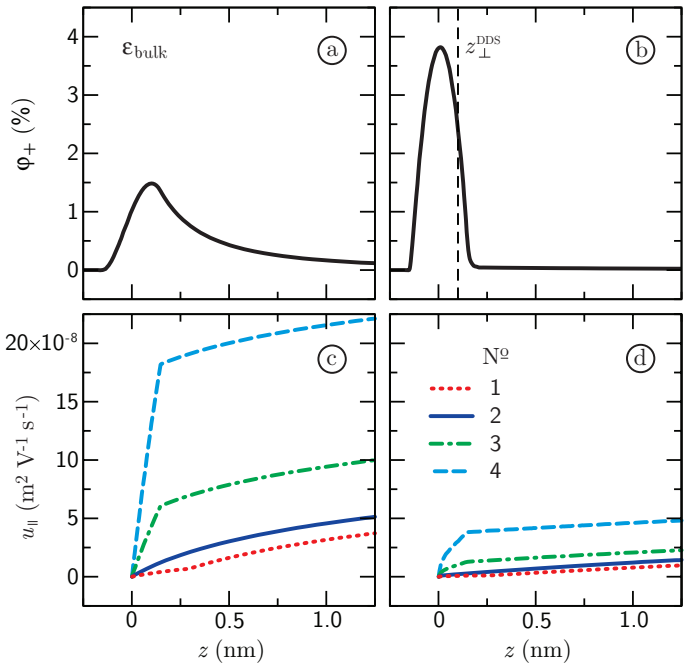

Figure 5.3: *Volume fraction of ions, calculated from a convolution according to Eq. 5.22 of the ion density $c_+(z)$ with the molecular volume of Eq. 5.23, using* (a) *a bulk dielectric constant and* (b) *a dielectric dividing surface at $z_\perp^{\mathrm{DDS}} = 0.1$ nm, as appropriate for a hydrophilic surface. The corresponding electro-osmotic mobility profiles are shown* (c, d) *for four different viscosity profiles (Eq. 5.7 with the parameters listed in Tab. 5.1), with apparent slip length b calculated using Eq. 5.8: $\eta_{bulk}/\eta_i = 15$ and $z_s = 0.15$ nm ($b = 2.1$ nm, dashed lines), $\eta_{bulk}/\eta_i = 5$ and $z_s = 0.15$ nm ($b = 0.6$ nm, dash-dotted lines), no slip (solid lines) and $\eta_{bulk}/\eta_i = 1/3$ with $z_s = 0.3$ nm ($b = -0.2$ nm, dotted lines). The bare surface charge density equals $\sigma_0 = -0.6$ e/nm^2 and the bulk salt concentration is $c_0 = 1$ mM. For the steric interactions defined in Eq. 5.19 we use $a_+ = a_- = 0.3$ nm and no non-electrostatic ion-wall interaction: $\mu_\pm(z) = 0$.*

with $v_\pm(z)\,\mathrm{d}z$ the volume of an ion slice of width $\mathrm{d}z$,

$$v_\pm(z) = \begin{cases} \pi\left(a_\pm^2/4 - z^2\right) & \text{if } |z| < a_\pm/2 \\ 0 & \text{otherwise.} \end{cases} \tag{5.23}$$

The volume fraction is used only for plotting the ion distribution; for all calculations we still assume that the charge is located at a single point in the center of the ion.

5.5.1 Numerical Results & Discussion

We numerically solve the modified Poisson-Boltzmann equation (Eqs. 5.16–5.20) using a fixed bare surface charge density σ_0 located at $z = 0$ and vanishing electrostatic potential at infinity as boundary conditions. The ion centers are allowed to approach $z = 0$, thereby partly penetrating the solid, which accounts for surface softness. For the fermionic steric repulsion of Eq. 5.19 we use $a_\pm = 0.3$ nm.

In Fig. 5.3 we show the volume fraction profile of counterions $\varphi_+(z)$, at bulk salt concentration $c_0 = 1$ mM, for two different approximations of the dielectric function: (a) $\varepsilon_\perp(z) = \varepsilon_{bulk}$ and (b) using $\varepsilon_\perp(z)$ from Eq. 5.9 with the hydrophilic $z_\perp^{\mathrm{DDS}} = 0.1$ nm. The

Table 5.1: *Combinations of z_s and η_i used for the viscosity profile of Eq. 5.7. We also give the apparent slip length b according to Eq. 5.8.*

№	Surface type	z_s (nm)	η_{bulk}/η_i	b (nm)
1	Hydrophilic	0.3	1/3	−0.2
2	No slip	–	1	0.0
3	Moderately hydrophobic	0.15	5	0.6
4	Very hydrophobic	0.15	15	2.1

non-electrostatic interaction is set to zero, $\mu_{\pm}(z) = 0$. The bare surface charge density is $\sigma_0 = -0.6\ e/\mathrm{nm}^2$, which is the value measured for silica at 10^{-3} M KCl and pH = 7.5 [161]. Clearly, the counterions accumulate much closer to the wall when the dielectric profile is taken into account, which is due to the steep increase of the potential in the low-dielectric region. It should be noted that, although the density of ions directly at the wall is enhanced, it never exceeds its physical limit because of the fermionic steric repulsion introduced in Eq. 5.19. The electro-osmotic mobility $u_{\parallel}(z)/E_{\parallel}$ in the first nanometer next to the surface, calculated from Eq. 5.2, is shown in Figs. 5.3 (c)–(d) using the viscosity profile from Eq. 5.7 with four different combinations of η_i and z_s, which are listed in Tab. 5.1. Each combination can be characterized by its apparent slip length using Eq. 5.8: very hydrophobic ($\eta_{bulk}/\eta_i = 15$ and $z_s = 0.15$ nm, giving $b = 2.1$ nm), moderately hydrophobic ($\eta_{bulk}/\eta_i = 5$ and $z_s = 0.15$ nm, giving $b = 0.6$ nm), no slip ($\eta_i = \eta_{bulk}$, $b = 0$) and hydrophilic ($\eta_{bulk}/\eta_i = 1/3$ and $z_s = 0.3$ nm, giving $b = -0.2$ nm). Figs. 5.3 (c) and (d) already show a strikingly different behavior: the mobility is significantly lower when a dielectric dividing surface $z_{\perp}^{\mathrm{DDS}}$ is taken into account via Eq. 5.9 compared to using ε_{bulk}.

First puzzle: Saturation of the electrokinetic surface charge density. In Fig. 5.4, we plot (a) the electrokinetic surface charge density σ_{ek}, defined in Eq. 5.4, and (c) the conductive surface charge density σ_c, defined in Eq. 5.6 as a function of the bare surface charge density σ_0, using a bulk dielectric constant ($\varepsilon_{\perp}(z) = \varepsilon_{bulk}$) and four different viscosity profiles (Eq. 5.7 with the parameters listed in Tab. 5.1). Using the very hydrophobic viscosity profile (№ 4. in Tab. 5.1, $b = 2.1$ nm) or the moderately hydrophobic profile (№ 3. in Tab. 5.1, $b = 0.6$ nm), the electrokinetic surface charge density σ_{ek} exceeds the bare surface charge density σ_0, contrary to experimental evidence [175]. The correct behavior, $\sigma_{ek} < \sigma_0$, is only recovered when using a viscous layer (№ 1. in Tab. 5.1, $b = -0.2$ nm). At the same time, however, σ_c is also lowered, at roughly the same rate as σ_{ek}, see Fig. 5.4 (c). When a dielectric dividing surface is introduced, shown in Figs. 5.4 (b) & (d), the electrokinetic surface charge density saturates as a function of the bare surface charge density for all viscosity profiles. Because experiments show that saturation of σ_{ek} occurs at every surface type, we conclude that a dielectric profile of the form of Eq. 5.9 is necessary to explain the trend of the experimental mobility data that is sketched in Fig. 5.1 (b). The main effect of the hydrodynamic boundary condition is that σ_{ek} saturates at higher values at hydrophobic surfaces then at hydrophilic surfaces, again in agreement with experimental data [193]. Interestingly, the electrokinetic surface charge density rises above σ_0 for low values of σ_0, to which we will come back below.

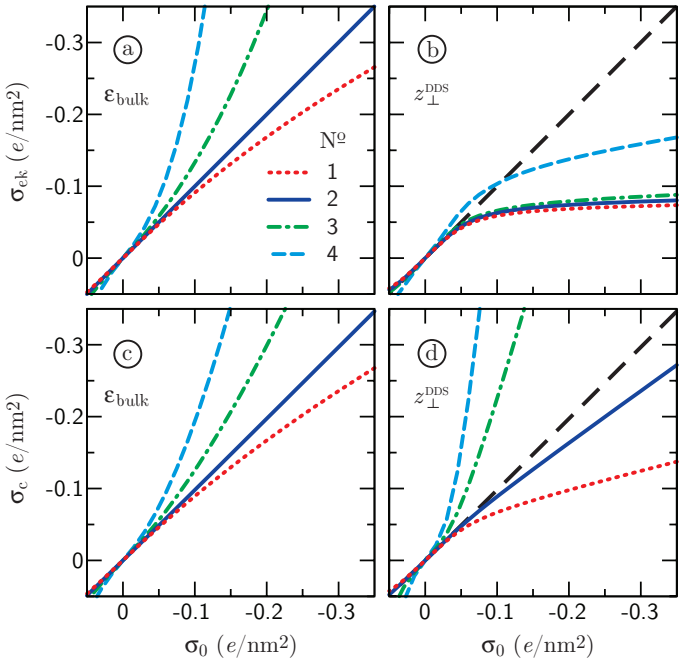

Figure 5.4: *Electrokinetic surface charge density* σ_{ek} (a, b) *and conductive surface charge density* σ_c (c, d) *as a function of the bare surface charge density* σ_0*, using a bulk dielectric constant* $\varepsilon_\perp(z) = \varepsilon_{bulk}$ *on the left* (a, c) *and using* $\varepsilon_\perp(z)$ *from Eq. 5.9 on the right* (b, d)*, with* $z_\perp^{\text{DDS}} = 0.1$ *nm (hydrophilic) when* $b \leq 0$ *and* $z_\perp^{\text{DDS}} = 0.12$ *nm (hydrophobic) when* $b > 0$*. The parameters of the viscosity profiles used are listed in Tab. 5.1:* № *1. Hydrophilic, dotted lines* ($z_s = 0.3$ *nm,* $\eta_{bulk}/\eta_i = 1/3$*,* $b = -0.2$ *nm);* № *2. No slip, solid lines* ($\eta_i = \eta_{bulk}$*,* $b = 0$*);* № *3. Moderately hydrophobic, dashed-dotted lines* ($z_s = 0.15$ *nm,* $\eta_{bulk}/\eta_i = 5$*,* $b = 0.6$ *nm);* № *4. Very hydrophobic, dashed lines* ($z_s = 0.15$ *nm,* $\eta_{bulk}/\eta_i = 15$*,* $b = 2.1$ *nm). For all curves, the bulk salt concentration is* $c_0 = 1$ *mM. No non-electrostatic interaction potential is used,* $\mu_\pm(z) = 0$*, and for the steric interaction* $a_\pm = 0.3$ *nm.*

Second puzzle: Anomalous surface conductivity. We plot the conductive surface charge density σ_c as a function of the electrokinetic surface charge density σ_{ek} in Fig. 5.5, using (a) $\varepsilon_\perp(z) = \varepsilon_{bulk}$ and (b) the dielectric profile of Eq. 5.9. Without dielectric profile, σ_c is close to, or below σ_{ek}, whereas σ_c features a steep increase when the dielectric profile is used, in agreement with the experimental trends sketched in Fig. 5.1 (c). Thus the excess conductivity, which is traditionally referred to as anomalous surface conductance [179–181, 194], follows directly from the dielectric profile $\varepsilon_\perp(z)$.

Third puzzle: Salt-concentration dependence of the electrokinetic surface charge density. In Fig. 5.6 (a), we plot the electrokinetic surface charge density σ_{ek} as a function of the bare surface charge density σ_0 at different values of the bulk salt concentration c_0. Curves are shown for a very hydrophobic surface (№ 4. in Tab. 5.1: $b = 2.1$ nm and $z_\perp^{\text{DDS}} = 0.12$ nm) and for a typical hydrophilic surface (№ 1. in Tab. 5.1: $b = -0.2$ nm and $z_\perp^{\text{DDS}} = 0.10$ nm). Clearly, the electrokinetic surface charge density is higher at hydrophobic surfaces than at hydrophilic surfaces at all salt concentrations, in accordance with experimental results [175, 193]. The difference between the surface types is primarily caused by the different viscosity profiles; $z_\perp^{\text{DDS}}$ is comparable for both surface types. Sim-

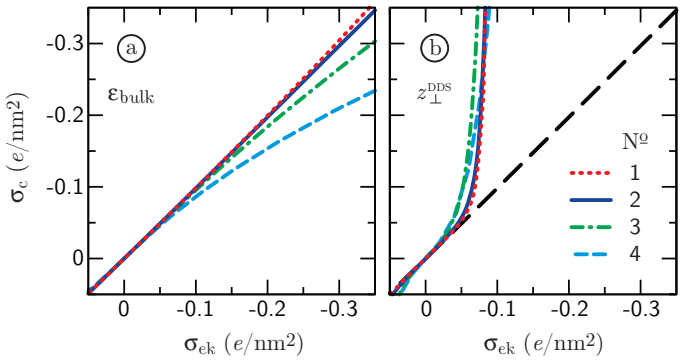

Figure 5.5: *Conductive surface charge density σ_c versus electrokinetic surface charge density σ_{ek},* (a) *using $\varepsilon_\perp(z) = \varepsilon_{bulk}$ and* (b) *using Eq. 5.9 with $z_\perp^{DDS} = 0.1$ nm (hydrophilic) when $b \leq 0$ and $z_\perp^{DDS} = 0.12$ nm (hydrophobic) when $b > 0$. Eq. 5.7 is used for the viscosity profile, with the parameters listed in Tab. 5.1. For all curves, the bulk salt concentration is $c_0 = 1$ mM. No non-electrostatic interaction potential is used, $\mu_\pm(z) = 0$, while steric interaction (Eq. 5.19) is included with $a_\pm = 0.3$ nm.*

ilar to the experimental trend sketched in Fig. 5.1 (d) [175], the behavior as a function of salt concentration is opposite at the two surface types: Whereas σ_{ek} increases with increasing salt concentration at the hydrophobic surface, it decreases with increasing salt concentration at the hydrophilic surface. The reason for this opposite behavior is that for moderate and high bulk salt concentration, $c_0 > 10^{-3}$ M, the charge distribution shifts toward the wall upon increasing c_0 (decreasing Debye screening length), and more charge is located in the region of varying viscosity. At hydrophilic surfaces, the effect of the higher viscosity in the interfacial layer is to decrease the electrokinetic surface charge density σ_{ek}, whereas at hydrophobic surfaces the low viscosity increases σ_{ek}. At low salt concentrations, $c_0 \leq 10^{-3}$ M, the effect diminishes because the width of the charge distribution in that regime is not determined by the bulk salt concentration.

Apart from the dependence on surface type discussed above, the electrokinetic surface charge density also depends on the specific ion-surface interaction, which has a significant non-electrostatic component. In our calculations, this contribution is modeled by the function $\mu_\pm(z)$ given in Eq. 5.21, which has only one parameter, α (keeping the decay length fixed and equal to the ion diameter $a_\pm$). In Fig. 5.6 (b), we plot σ_{ek} as a function of σ_0 for different values of the non-electrostatic interaction strength α for fixed $c_0 =$ 1 mM. Positive values of α repel ions from the surface, thereby increasing σ_{ek}, whereas negative values attract ions to the surface, decreasing σ_{ek}. Interestingly, varying α within a moderate range of only several times the thermal energy has an equally large effect on σ_{ek} as the surface-type dependence shown in Fig. 5.6 (a). To calculate the value of α, the surface adsorption excess can be compared with molecular dynamics simulations. Simulations of uncharged polar and non-polar self-assembled monolayers show that cations are attracted to polar surfaces, but repelled from non-polar ones [122]. From these results we expect that α is negative for hydrophilic surfaces and positive for hydrophobic surfaces. Note that the ion-surface potential may be much more complex than the simple form assumed in Eq. 5.21.

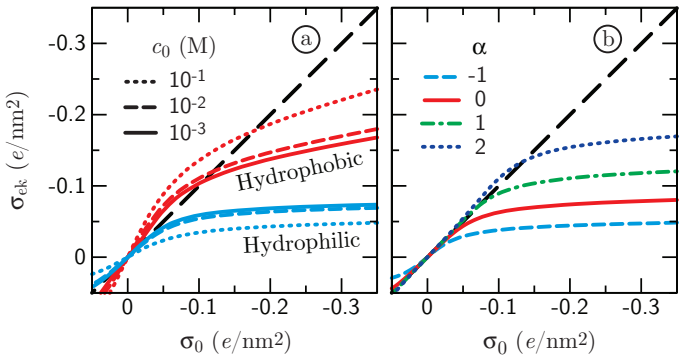

Figure 5.6: (a) *Effect of the bulk salt concentration c_0 on the electrokinetic surface charge density σ_{ek} as a function of the bare surface charge density σ_0 for hydrophilic surfaces (blue lines), calculated using $z_s = 0.3$ and $\eta_{bulk}/\eta_i = 1/3$ (№ 1. in Tab. 5.1) in combination with $z_\perp^{\mathrm{DDS}} = 0.10$ nm, and for hydrophobic surfaces (red lines), calculated using $z_s = 0.15$ nm and $\eta_{bulk}/\eta_i = 15$ (№ 4. in Tab. 5.1) in combination with $z_\perp^{\mathrm{DDS}} = 0.12$ nm. For all curves $a_\pm = 0.3$ nm and $\mu_\pm(z) = 0$.* (b) *Dependence of σ_{ek} on the strength α of the non-electrostatic potential $\mu_\pm(z)$ given in Eq. 5.21. For illustration purposes, we use the hydrophilic dielectric dividing surface $z_\perp^{\mathrm{DDS}} = 0.10$ nm and bulk viscosity $\eta_i = \eta_{bulk}$. The bulk salt concentration $c_0 = 1$ mM.*

5.5.2 Fitting Experimental Data

In the previous sections we have shown that the dielectric profile of Eq. 5.9 induces condensation of ions into a thin layer, and that the resulting electrokinetic and conductive surface charge densities qualitatively correspond to the experimental trends sketched in Fig. 5.1. In the following, we will fit the model to published experimental data using the interaction strength α of the non-electrostatic potential $\mu_\pm(z)$, given in Eq. 5.21, as a free parameter.

In Fig. 5.7, we show measurements of the electrokinetic surface charge density σ_{ek} taken from Ref. [175] as symbols, together with the fitted curves. At the hydrophilic surfaces, the model captures the data very well over the entire range of the bare surface charge density σ_0. Note that the data presented in Ref. [175] have been corrected using a different model for the anomalous surface conduction, and that the raw data reproduced here have been reconstructed. At the hydrophobic surface, the electrokinetic surface charge density σ_{ek} exceeds the bare surface charge density for $|\sigma_0| < 0.15\ e/\mathrm{nm}^2$, which is reproduced by the model. Originally, this apparent extra electrokinetic surface charge was considered to be a measurement error [175]. From our calculations we conclude, however, that it is possibly caused by hydrodynamic slip at the solid surface. At high absolute values of the bare surface charge density σ_0, the model disagrees with the experimental data at the hydrophobic surface, which probably has to do with the simplified model used. The fit parameter α is negative at the hydrophilic surfaces, indicating that ions are attracted to polar surfaces, and slightly positive at the hydrophobic surface, indicating that ions are repelled from non-polar surfaces, in line with results from molecular dynamics simulations [122]. Again, the opposite trend of σ_{ek} as a function of bulk salt concentration at the two surface types in Fig. 5.7 is captured very well within our model.

As symbols in Fig. 5.8, we reproduce experimental data of the conductive surface charge density σ_c as a function of the electrokinetic surface charge density σ_{ek} at (a) hydrophilic surfaces and (b) hydrophobic surfaces in contact with a KCl solution at several low salt

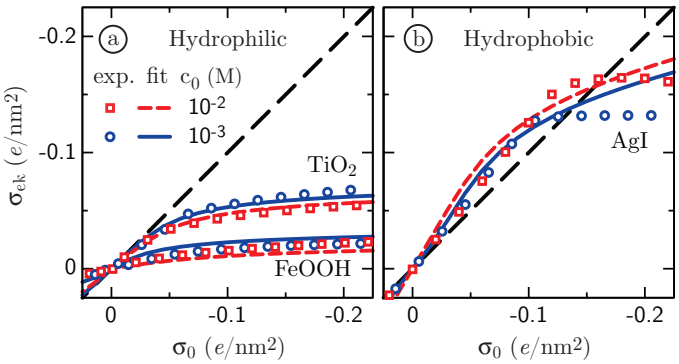

Figure 5.7: *Comparison of theory predictions to experimental data from Ref. [175] (symbols), taken at different concentrations* KNO_3*. Data points are a discretization of the curves presented in Ref. [175]. In order to cancel the surface conduction correction [175], the hydrophilic curves have been reconstructed according to* $\sigma_{ek} = \sinh\left(\sinh^{-1}\left(\sigma_{ek}^{corr.}\right)/1.55\right)$*, with* $\sigma_{ek}^{corr.}$ *the values reported in Ref. [175]. For the hydrophilic curves,* $z_\perp^{\mathrm{DDS}} = 0.10$ *nm,* $z_s = 0.3$ *nm and* $\eta_i = 3\eta_{bulk}$*, giving* $b = -0.2$ *nm (viscosity profile* Nº 1 *in Tab. 5.1). For the hydrophobic curves,* $z_\perp^{\mathrm{DDS}} = 0.12$ *nm,* $z_s = 0.15$ *nm and* $\eta_i = \eta_{bulk}/15$*, giving* $b = 2.1$ *nm (viscosity profile* Nº 4 *in Tab. 5.1). The fit parameters used are* $\alpha = -0.25$ *(*TiO_2*),* $\alpha = -1.7$ *(FeOOH) and* $\alpha = 0.25$ *(AgI).*

concentrations c_0. The data on silica particles [195] and polystyrene particles [181, 196] have been taken from literature directly. The data on rectangular silica channels [130] have been fitted numerically with the Gouy-Chapman model for a slit-like geometry to extract σ_{ek} and σ_c from the streaming potential and the electrical conductance respectively. The spread in the data is likely to be caused by the different materials and geometries used in the experiments. In Fig. 5.8 (a), we show our model for the hydrophilic viscosity profile (Nº 1. in Tab. 5.1: $b = -0.2$ nm) using $\alpha = 0$ (solid line) and $\alpha = -1$ (broken line) for illustration. The salt concentration for all calculated curves is $c_0 = 1$ mM, because at low salt concentration the dependence of σ_{ek} and σ_c on c_0 is minor. The model captures the data very well, using an attractive non-electrostatic potential with an interaction strength between $\alpha = 0$ and $\alpha \simeq -1$. For the curves in Fig. 5.8 (b), we use the viscosity profile Nº 4. in Tab. 5.1 ($b = 2.1$ nm), as appropriate for very hydrophobic surfaces. We use $\alpha = 0$ (solid line) and $\alpha = 1$ (dotted line), showing that the hydrophobic surface can be modeled with a non-electrostatic interaction around $\alpha = 0$, or a slightly repulsive potential of the order of $\alpha = 1$. The slight non-electrostatic attraction at the hydrophilic surface and repulsion at the hydrophobic surface corresponds well to the fit parameters used to model σ_{ek} in Fig. 5.7, as well as to the trend expected from simulations of uncharged polar and non-polar surfaces [122]. However, fitting the capacitance data shown in Fig. 2.12 in Sec. 2.4.3, which are taken in a different concentration regime, requires a repulsive non-electrostatic potential for all data. The only difference in the model is the use of the viscosity profile, which is not needed to calculate the capacitance. Therefore, the discrepancy is likely to be related to the fact that we use the viscosity profiles from molecular dynamics simulations at atomically smooth surfaces. A more accurate viscosity profile, or including the effect of surface roughness, may reconcile the different results. Alternatively, the effective boundary position at which the electrostatic external potential is applied, on which the double-layer capacitance depends sensitively, might be displaced from the aqueous phase in measurements on conducting materials, such as graphene layers.

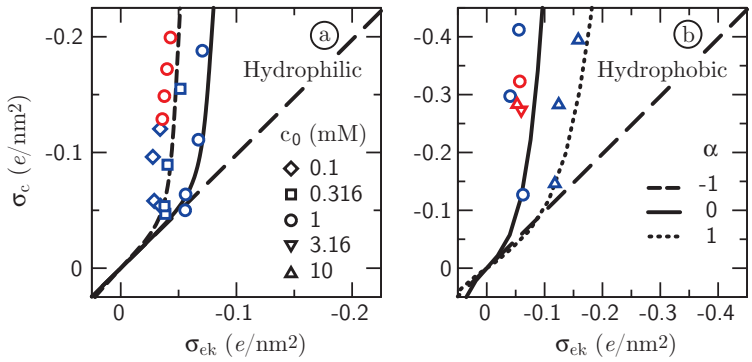

Figure 5.8: *Conductive surface charge density σ_c versus electrokinetic surface charge density σ_{ek} for different systems in contact with a* KCl *solution of bulk concentration c_0.* (a) *Data from rectangular silica channels (dark blue, Ref. [130]) and monodisperse porous silica particles (red, Ref. [195]).* (b) *Data from monodisperse spherical polystyrene particles (dark blue, Ref. [181] and red, Ref. [196]). Curves are shown for interaction parameters $\alpha = 0$ and $\alpha = -1$ (hydrophilic) and $\alpha = 0$ and $\alpha = 1$ (hydrophobic), using a bulk concentration of* 1 *mM.*

5.6 Summary & Conclusions

Using a dielectric profile with a low-dielectric layer at the interface, as extracted from molecular dynamics simulations, in a modified Poisson-Boltzmann equation, we are able to explain three well-established experimental puzzles that have not been understood within the context of a single model before. First, we capture the saturation of the electro-osmotic surface charge density σ_{ek} as a function of the bare surface charge density σ_0. Second, we explain the excess surface conductivity commonly measured in electrokinetic experiments, making the assumption of anomalous electrical conductance behind the shear plane superfluous. Third, we reproduce the opposite trends of the electro-osmotic mobility as a function of salt concentration at hydrophilic and hydrophobic surfaces. The physical mechanism leading to the observed behavior is the enhanced condensation of ions close to the surface, which is due to the low effective dielectric constant. This causes saturation of the electrokinetic surface charge density, but not of the conductive surface charge density, explaining the notion of anomalous excess surface conductivity.

Chapter 6

Final Observations & Outlook

The aim of the work described in the preceding chapters is to incorporate information about the molecular structure of interfacial water into the description of the static and dynamic properties of aqueous solutes, using molecular dynamics (MD) simulations to complement continuum theory. We show that the use of continuum theory enables us to reach length and time scales that are unattainable using only MD simulations. At the same time, it provides us with the flexibility to easily vary system parameters such as geometry, salt concentration and surface charge density. One of the most significant advantages of this combination of molecular detail, flexibility of model parameters and sufficiently large scale is that it allows direct comparison with experimental data. Our multiscale modeling approach thus provides us with the means for experimental verification of our theoretical models, and simultaneously offers new insight into the molecular origin of experimental observations.

Summarizing the results of our work, we first establish the framework to extract the full tensorial dielectric interface profiles from MD data (Chapter 2). Especially the perpendicular dielectric profiles $\varepsilon_{\perp}^{-1}(z)$ exhibit rich structure and distinct differences between hydrophobic and hydrophilic surfaces. In the context of coarse-grained Poisson-Boltzmann modeling, experimental capacitance data are well reproduced, indicating the validity of our theoretical approach. We show that a low-dielectric interfacial layer – a concept known as the Stern layer – arises naturally from dielectric interfacial effects of pure water, at least at low salt concentration. In this way, we establish the molecular origin of the Stern layer, which has been used in models of the electric double layer for almost a century. The dielectric dividing surface position is suggested as a straightforward definition of the width of a Stern layer with $\varepsilon = 1$.

Second, we quantify how the hydrodynamic boundary condition influences electrokinetic flow (Chapter 3). In particular, we show that the electrokinetic energy conversion efficiency in hydrophilic nanofluidic channels agrees well with the hydrodynamic model of a single interfacial water layer with strongly enhanced viscosity. In addition, using estimates from *ab initio* simulations, we show that charge transfer between water molecules – which is one of the molecular effects disregarded in classical MD simulations – does not contribute significantly to the electrophoretic mobility of gas bubbles.

Third, we incorporate molecular spinning of water into the Navier Stokes equation, showing that electrokinetic pumping of water in absence of mobile charges is possible with

rotating electric fields, which opens the way for efficient power conversion in nanoscopic devices (Chapter 4). Similarly, an electric field in the shape of a running wave, generated by an array of externally attached electrodes, may be used to drive the flow of pure water through a carbon nanotube. Static electric fields in an electro-neutral dipolar fluid do not give rise to flow, however, even in the presence of dipolar surface ordering. That means that, although the polar molecular ordering has a decisive influence on the interfacial electrostatics as well as on the distribution of ions at charged interfaces, it does not have a direct effect on the mobility of solutes in static electric fields. This result marks the end of a surge of debate and speculation about molecular ordering as the possible origin of the observed electrophoretic mobility of nominally uncharged oil droplets and gas bubbles in pure water, proving that its source must be found elsewhere.

Finally, we incorporate the combined effects of the varying dielectric permittivity and the viscosity profile into a modified continuum theory, and numerically calculate the electro-osmotic flow and the electric surface conductivity of charged surfaces (Chapter 5). Our model captures the experimental trends of the electro-osmotic flow as a function of the bare surface charge density, as well as its dependence on the bulk salt concentration with high accuracy. Moreover, the experimentally well-established excess surface conductivity, generally referred to as *anomalous surface conductivity* follows directly from our model. The latter result makes the assumption of electrical conductance through otherwise static water layers – which has been the common explanation of the experimental observations – superfluous. Our model provides direct insight into the molecular origin of the dynamic properties of interfacial water layers, which have been elusive and subject to speculation for a long time.

In conclusion, we show that classical molecular dynamics simulations can be used to provide the molecular information missing from standard continuum theory, and that taking the profiles from MD simulations into account yields very good agreement with experimental data on a wide range of static and dynamic properties of aqueous interfaces. Therefore, at the current stage, our modeling scheme seems to contain sufficient complexity to explain a number of at-first-sight disconnected and hitherto puzzling experimental findings and trends. Needless to say, however, it only constitutes a first step toward a complete description of the intricate electrostatic and electrokinetic properties of charged surfaces in a unified framework.

Future work could be aimed at extending our modeling to include a number of important effects that have been left out up to now; examples include charge regulation at the surface as a function of varying salt concentration, surface roughness and curvature and electrofriction effects [197], as well as electrostatic correlation effects beyond the mean-field level [198]. We have also made some rigorous simplifying approximations, *e.g.* in studying planar surfaces in contact with pure water and modeling the viscosity and dielectric profiles by simple square-well functions (Chapter 5). In the remainder of this chapter, we list possible directions for future research.

Ions at interfaces. All profiles calculated in this thesis are extracted from MD simulations of pure water at uncharged surfaces. The influence that ions and surface charges have on the hydrodynamic interfacial properties and on the dielectric profile comprises both the effect of atomic polarizability and the effect of highly charged objects on the local water structure. Modifications to the dielectric profile and non-linear effects are expected at high salt concentrations. In addition, surface charges cause electrofriction, which affects the

hydrodynamic properties of the interface. It is unclear whether such contributions can be calculated from classical MD simulations, or whether *e.g.* quantum-chemical simulations are needed.

Another simplification used in our current work is to treat the non-electrostatic surface-ion interaction using a simple exponentially decaying function. Ion adsorption potentials may be much more complex, and deserve attention in future investigations.

Polar ions. Propensity of the water ions hydronium (H_3O^+) and hydroxide (OH^-) for adsorption on different surface types remains controversial. Different experimental results have contradictory interpretations, and conclusions from MD simulations are questionable because of the lack of reliable force fields. In Ref. [i], we report on the optimization of a classical MD force field for hydronium and hydroxide with respect to the solvation free energy and the activity coefficient. In future work, these force fields can be used to gain insight in the molecular properties that determine the behavior of the water ions at aqueous interfaces.

Non-local dielectric effects. High surface charge density reduces the typical decay length of the displacement field. When the characteristic length scale of the displacement field variation reaches the typical length scale on which the dielectric profile varies, the full non-local dielectric tensor is needed to properly calculate the electrostatics. The limits of applicability of our current approach, as well as a suitable theoretical framework to treat non-local dielectric effects on a molecular level have not been established and need attention in future studies.

Effects beyond mean-field theory. In this thesis, all electrostatics have been treated on the mean-field level, which provides an excellent description of some of the most commonly encountered systems, namely monovalent ions at moderate salt concentrations. The approximation breaks down, however, for high surface charge density, as well as for high counterion valency, in which case correlated effects such as image-charge interactions and ion-ion correlations gain importance.

Non-ideal surfaces and complex geometries. Finally, the viscosity profile, density and dielectric profile at inhomogeneously charged, corrugated and curved surfaces deviate from the predictions for smooth planar surfaces, but to which extent is unclear. Therefore, more research is needed to establish whether our current theoretical models of the interfacial properties can be used as building blocks to extend our current theoretical framework to more complicated geometries and surface types.

Appendix A

Literature Values of the Double-Layer Capacitance

This appendix contains an overview of published experimental values of the double-layer capacitance on various carbon-based surfaces in aqueous electrolytes. The capacitance of the electrical double layer is measured using cyclic voltammetry, galvanostatic charge-discharge or AC impedance spectroscopy. The accessible surface area is determined using N_2 adsorption.

In the tables below, we have grouped the different measurements based on the contact angle in aqueous solution; when below 90°, the substrate is classified as hydrophilic (listed in Tab. A.1), otherwise as hydrophobic (listed in Tab. A.2). The scattering in the data between substrates and electrolytes is larger than the structural difference between hydrophilic and hydrophobic substrates. Nevertheless, when a specific substrate is modified to become more hydrophilic, for example using functional groups or doping, the double-layer capacitance increases [30, 199]. Materials of which the contact angle is unknown or unclear are displayed in Tab. A.3. Many of the materials used for double-layer capacitors belong to the class of so-called activated carbons, which are treated with a gas plasma or a strong acid or base solution to make the surface more porous. The specific capacitance of the activated carbons is shown in Tab. A.4. While increasing the total capacitance of the sample, activation of a carbon surface often decreases the capacitance per unit surface area dramatically [200, 201]. Although the mechanism leading to this decrease is unclear, we can safely assume that a part of the additional surface area created by the activation process is inaccessible to the electrolyte, and therefore does not contribute to the double-layer capacitance. Because of these poorly defined surface characteristics, Fig. 2.12 of Sec. 2.4.3 only contains the data from Tabs. A.1, A.2 and A.3.

Table A.1: *Double-layer capacitance of hydrophilic carbon-based materials.*

Surface material	Contact angle (°)	Electrolyte	Concentration (M)	Capacitance (μF/cm^2)	Ref.
Carbon fibers	24 - 37 [202]	H_2SO_4	0.5	6.0 7.5 9.2 12.9	[203][a]
Carbon-coated Al_2O_3 Nitrogen-doped Boron-doped	57 41 60	H_2SO_4	1	7.0 11.4 12.9	[199]
Oxidated polyvinyl-pyridine Blend with coal-tar pitch	45 - 67 [205, 206]	H_2SO_4	1	13.2 14.3	[204][b]

[a]Different values correspond to different commercial samples (untreated).
[b]Values estimated by voltammetry at 1 mV s^{-1}. The blend with coal tar pitch is 1 : 1.

Table A.2: *Double-layer capacitance of hydrophobic carbon-based materials.*

Surface material	Contact angle (°)	Electrolyte	Concentration (M)	Capacitance (μF/cm^2)	Ref.
Boron-doped diamond	> 90 [207]	H_2SO_4	0.1	3.7 7.1	[208][a]
		KCl	0.1	3.4 4.5	
		$NaNO_3$	0.1	3.8 6.3	
		NaOH	0.1	3.9 4.8	
Carbide-derived carbon TiC, SiC & SiC/TiC	> 90 [209]	H_2SO_4	2	11.4 13.8 11.8	[210]
Graphite	98 [211]	KOH	6	17.5 16.7 19.2 25.9 33.9 41.6 51.4 64.0	[212][b]
Graphene nanosheets	127 [211]	KOH	7.6	29 26 52	[213][c]
Carbon black Graphite powder		H_2SO_4 NaCl	1 5.6	8 35	[214]

[a]The different values correspond to AC impedance and cyclic voltametry measurements, respectively.
[b]The surface area of natural graphite was increased using ball-milling; different values correspond to different milling times.
[c]Different values correspond to different concentrations of oxidant used to prepare the graphene sheets.

Table A.3: *Double-layer capacitance of materials with unknown contact angle.*

Surface material	Electrolyte	Concentration (M)	Capacitance (μF/cm^2)	Ref.
Porous carbon	H_2SO_4	1	5.3	[215]
Porous carbon with polyaniline			9.0	
Silica-templated mesoporous carbon	H_2SO_4	1	12.8	[204]
			10.1	
			7.4	
			9.3	
			11.4	
			9.4	
Silica-templated mesoporous carbon	H_2SO_4	1	7.3	[216]
		2	14	[217]
		2	13	[218]
Silica-templated mesoporous carbon	H_2SO_4	1	10.2	[219][a]
			10.6	
			10.7	
			10.9	
	KOH	6	9.8	
			10.9	
			8.9	
			10.6	
Mesoporous carbon with NiO	KOH	2	18.2	[220]
Carbon aerogel	KOH	4	23	[214]
	KOH	6	28.5	[221]
Porous carbon	KOH	6	33	[201]
Self-ordered mesoporous carbon	$LiPF_6$	1	10	[222]
Nitrogen-containing mesoporous carbon	KOH	6	39.2	[200][b]
Ordered mesoporous carbon			10.0	
Porous carbon from carbonization	KOH	6	20.8	[223][c]
of poly(vinylidene chloride)			22.0	
			20.8	
			18.2	
			15.2	
			12.9	
Diamond film	NaCl	0.5	3.7	[224][d]
Polyacrylonitrile	H_2SO_4	1	24.9	[204]
Blend with coal tar pitch			20.3	
			17.5	
TiC/TiO_2	H_2SO_4	2	14.8	[210]
Carbon composite from waste paper	KOH	6	43.2	[221]

[a] Data taken at two different samples, using galvanostatic discharge at 100 mA g^{-1} and using cyclic voltammetry at 1 mV s^{-1}.

[b] Data taken at the lowest scan rate (2 mV s^{-1}).

[c] Different values correspond to different carbonization temperatures (400°C – 900°C).

[d] After equilibration in electrolyte, assuming complete wetting at the maximum of the capacitance.

Table A.4: *Double-layer capacitance of different kinds of activated carbons.*

Surface material	Electrolyte	Concentration (M)	Capacitance (μF/cm^2)	Ref.
CO_2 activated porous carbon	KOH	6	13	[201]
			9.6	
KOH activated porous carbon			10	
			8.8	
Nitrogen-containing mesoporous carbon, activated with KOH	KOH	6	26.2	[200]
			13.7	
			11.3	
Ordered mesoporous carbon, activated with KOH	KOH	6	11.2	[200]
			12.7	
			12.4	
KOH-activated carbon	H_2SO_4	1	20.4	[225][a]
			25.1	
			26.9	
NaOH-activated carbon			24.7	
			25.0	
			28.9	
Wood-origin HNO_3-activated carbon	H_2SO_4	1	11.6	[226][b]
			10.3	
			19.1	
			25.5	
			23.0	
			32.6	
Activated carbon	NaCl	5.6	19	[214]
O_2-activated carbon fibers			6.6	[203]
			7.0	
			9.1	
			13.2	

[a] Different values correspond to different carbonization temperatures (600°C – 700°C).

[b] Data taken using galvanostatic charge-discharge at $50 - 100$ mA g^{-1}; Different values correspond to samples with different surface functional groups.

Appendix B

Electrokinetics Within the Gouy-Chapman Model

We derive the electro-osmotic mobility, the electrokinetic surface charge density and the conductive surface charge density from the Gouy-Chapman model.

Gouy-Chapman model. The standard Poisson equation is given by

$$\varepsilon_0 \varepsilon_{bulk} \nabla^2 \psi(z) = -\rho(z). \tag{B.1}$$

According to the standard Boltzmann equation, the charge density $\rho(z)$ equals

$$\rho(z) = -2ec_0 \sinh[\beta e \psi(z)]. \tag{B.2}$$

The solution to the Poisson-Boltzmann equation (Eqs. B.1–B.2) for a monovalent electrolyte at a charged plane is

$$\psi(z) = -\frac{2}{\beta e} \ln \frac{1+\gamma \exp[-\kappa z]}{1-\gamma \exp[-\kappa z]}, \tag{B.3}$$

with

$$\gamma = -\kappa\lambda + \sqrt{\kappa^2\lambda^2 + 1}. \tag{B.4}$$

The inverse Debye screening length κ and the Gouy-Chapman length λ are given by

$$\kappa = \sqrt{\frac{2e^2 c_0 \beta}{\varepsilon_0 \varepsilon_{bulk}}} \quad \text{and} \quad \lambda = \frac{2\varepsilon_0 \varepsilon_{bulk}}{\beta e |\sigma|}. \tag{B.5}$$

The electro-osmotic mobility is related to the charge density by the Stokes equation, which reads

$$\eta_{bulk} \nabla^2 u_{\parallel}(z) = -\rho(z) E_{\parallel}, \tag{B.6}$$

for spatially constant viscosity η_{bulk}.

Electro-osmotic mobility. Eliminating the charge density $\rho(z)$ from Eqs. B.1 and B.6 yields

$$\varepsilon_0 \varepsilon_{bulk} \nabla^2 \psi(z) = \frac{\eta_{bulk}}{E_{\parallel}} \nabla^2 u_{\parallel}(z). \tag{B.7}$$

Integrating twice with boundary conditions $\nabla\psi(z) = \nabla u_{\parallel}(z) = 0$ for $z \to \infty$ and the no-slip boundary condition $u_{\parallel}(0) = 0$ gives the electro-osmotic mobility,

$$\frac{u_{\parallel}(z)}{E_{\parallel}} = \frac{\varepsilon_0 \varepsilon_{bulk}}{\eta_{bulk}} \left[\psi(z) - \psi(0)\right]. \tag{B.8}$$

Defining $\psi(0) = \zeta$ and using $\psi(z \to \infty) = 0$ leads to the Helmholtz-Smoluchowski equation as shown in Eq. 4.1.

Electrokinetic surface charge density. To solve the Poisson-Boltzmann equation (given by Eqs. B.1 and B.2) for a fixed surface charge density σ, we multiply both sides of Eqs. B.1 and B.2 by $2\nabla\psi(z)$, giving

$$\varepsilon_0 \varepsilon_{bulk} \nabla \left[\nabla\psi(z)\right]^2 = 4ec_0 \sinh\left[\beta e\psi(z)\right] \nabla\psi(z). \tag{B.9}$$

Integrating both sides, we arrive at

$$\varepsilon_0 \varepsilon_{bulk} \left[\nabla\psi(z)\right]^2 = \frac{4c_0}{\beta} \left(\cosh\left[\beta e\psi(z)\right] - 1\right), \tag{B.10}$$

where we used $\cosh\left[\beta e\psi(z)\right] = 1$ for $\psi(z) = 0$. Rewriting with the help of $\sqrt{\cosh x - 1} = \sqrt{2}\sinh\left[x/2\right]$, we arrive at

$$\nabla\psi(z) = -\sqrt{\frac{8c_0}{\beta\varepsilon_0\varepsilon_{bulk}}} \sinh\left[\frac{\beta e\psi(z)}{2}\right], \tag{B.11}$$

where the minus sign applies because $\nabla\psi(z)$ must be negative for positive values of $\psi(z)$. From the electroneutrality condition and $\nabla\psi(z) = 0$ for $z \to \infty$ we find that the surface charge density equals

$$\sigma = -\int_0^{\infty} \rho(z)\,\mathrm{d}z = -\varepsilon_0\varepsilon_{bulk}\nabla\psi(0). \tag{B.12}$$

Combining Eq. B.11 with Eq. B.12 gives the Grahame equation

$$\sigma = \sqrt{\frac{8c_0\varepsilon_0\varepsilon_{bulk}}{\beta}} \sinh\left[\frac{\beta e\,\zeta}{2}\right]. \tag{B.13}$$

Eq. B.13 defines the electrokinetic surface charge density σ_{ek} when the ζ-potential is calculated using Eq. 4.1.

Conductive surface charge density. The surface conductivity is given by Eq. 5.5. Similar to the Grahame equation, the surface conductivity can be expressed as an equivalent surface charge density using the Gouy-Chapman theory. For convenience, we split Eq. 5.5 in three parts: the convective part (first line),

$$\frac{I^{(1)}}{E_{\parallel}} = \int_0^{\infty} e\left[c_+(z) - c_-(z)\right]\left[u_{\parallel}(z)/E_{\parallel}\right]\mathrm{d}z, \tag{B.14}$$

and two conductive parts (second line),

$$\begin{aligned} \frac{I^{(2)}}{E_{\parallel}} &= \int_0^{\infty} e\nu_+\left(c_+(z) - c_0\right)\,\mathrm{d}z \\ \frac{I^{(3)}}{E_{\parallel}} &= \int_0^{\infty} e\nu_-\left(c_-(z) - c_0\right)\,\mathrm{d}z. \end{aligned} \tag{B.15}$$

Inserting the electro-osmotic mobility of Eq. B.8 and the charge density of Eq. B.1 in Eq. B.14 gives

$$\frac{I^{(1)}}{E_{\|}} = -\frac{\varepsilon_0^2 \varepsilon_{bulk}^2}{\eta_{bulk}} \int_0^\infty \nabla^2 \psi(z) \left[\psi(z) - \psi(0)\right] \mathrm{d}z, \tag{B.16}$$

which can be integrated by parts to give

$$\frac{I^{(1)}}{E_{\|}} = \frac{\varepsilon_0^2 \varepsilon_{bulk}^2}{\eta_{bulk}} \int_0^\infty \left[\nabla \psi(z)\right]^2 \mathrm{d}z, \tag{B.17}$$

using $\nabla\psi(z) = 0$ for $z \to \infty$. Inserting the derivative of Eq. B.3 in Eq. B.17 yields

$$\begin{aligned} \frac{I^{(1)}}{E_{\|}} &= \frac{\varepsilon_0^2 \varepsilon_{bulk}^2}{\eta_{bulk}} \int_0^\infty \left[\frac{4\kappa\gamma \exp\left[-\kappa z\right]}{\beta e \left(1 - \gamma^2 \exp\left[-2\kappa z\right]\right)}\right]^2 \mathrm{d}z \\ &= \frac{\varepsilon_0^2 \varepsilon_{bulk}^2}{\eta_{bulk}} \left[-\frac{8\kappa\gamma^2 \exp\left[-2\kappa z\right]}{\beta^2 e^2 \left(1 - \gamma^2 \exp\left[-2\kappa z\right]\right)}\right]_0^\infty \\ &= \frac{\varepsilon_0^2 \varepsilon_{bulk}^2}{\eta_{bulk}} \frac{8\kappa\gamma^2}{\beta^2 e^2 \left(1 - \gamma^2\right)}. \end{aligned} \tag{B.18}$$

The second part of the conductivity equals

$$\begin{aligned} \frac{I^{(2)}}{E_{\|}} &= \int_0^\infty e\nu_+ c_0 \left[\left(\frac{1 + \gamma \exp\left[-\kappa z\right]}{1 - \gamma \exp\left[-\kappa z\right]}\right)^2 - 1\right] \mathrm{d}z \\ &= \int_0^\infty e\nu_+ c_0 \left[\frac{4\gamma \exp\left[-\kappa z\right]}{\left(1 - \gamma \exp\left[-\kappa z\right]\right)^2}\right] \mathrm{d}z \\ &= e\nu_+ c_0 \left[-\frac{4\gamma \exp\left[-\kappa z\right]}{\kappa \left(1 - \gamma \exp\left[-\kappa z\right]\right)}\right]_0^\infty \\ &= e\nu_+ c_0 \frac{4\gamma}{\kappa \left(1 - \gamma\right)}. \end{aligned} \tag{B.19}$$

Similarly,

$$\frac{I^{(3)}}{E_{\|}} = -e\nu_- c_0 \frac{4\gamma}{\kappa \left(1 + \gamma\right)}. \tag{B.20}$$

Summing up $I = \sum_i I^{(i)}$ and rewriting in terms of κ gives the total excess conductivity

$$\frac{I}{E_{\|}} = \frac{32\gamma^2 e^2 c_0^2}{\kappa^3 \left(1 - \gamma^2\right) \eta_{bulk}} + \frac{4\gamma e c_0 \nu_+}{\kappa \left(1 + \gamma\right)} - \frac{4\gamma e c_0 \nu_-}{\kappa \left(1 - \gamma\right)}. \tag{B.21}$$

For simplicity, we assume $\nu_+ = \nu_- = \nu$, so Eq. B.21 becomes

$$\frac{I}{E_{\|}} = \frac{\gamma^2}{1 - \gamma^2} \left[\frac{32 e^2 c_0^2}{\kappa^3 \eta_{bulk}} + \frac{8 e c_0 \nu}{\kappa}\right], \tag{B.22}$$

which is inverted to give the following surface charge density, using Eqs. B.4 and B.5

$$\sigma = \frac{\kappa^2 \eta_{bulk}}{4 e c_0 + \nu \kappa^2 \eta_{bulk}} \sqrt{\frac{I}{E_{\|}}} \sqrt{\frac{I}{E_{\|}} + \frac{32 e^2 c_0^2}{\kappa^3 \eta_{bulk}} + \frac{8 e c_0 \nu}{\kappa}}. \tag{B.23}$$

Eq. B.23 defines the conductive surface charge density σ_c when the conductivity is calculated using Eq. 5.5.

List of Figures

List of Tables

List of Publications

This thesis is based on the following papers, which have been published in, or have been submitted to, or are being prepared to be submitted to peer-reviewed journals:

[i] **Douwe Jan Bonthuis** and Roland R. Netz, *Optimization of a classical molecular dynamics force field for hydronium and hydroxide*: *In preparation*

[ii] **Douwe Jan Bonthuis** and Roland R. Netz, *Unraveling the combined effects of dielectric and viscosity profiles on surface capacitance, electro-osmotic mobility and electric surface conductivity*: *Submitted*

[iii] **Douwe Jan Bonthuis**, Stephan Gekle and Roland R. Netz, *Profile of the static permittivity tensor of water at interfaces: Consequences for capacitance, hydration interaction and ion adsorption*, Langmuir **28**, 7679 (2012): *Cover article*

[iv] Klaus F. Rinne, Stephan Gekle, **Douwe Jan Bonthuis** and Roland R. Netz, *Nanoscale pumping of water by* AC *electric fields*, Nano Letters **12**, 1780 (2012)

[v] Robert Vácha, Ondrej Marsalek, Adam P. Willard, **Douwe Jan Bonthuis**, Roland R. Netz and Pavel Jungwirth, *Charge transfer between water molecules as the possible origin of the observed charging at the surface of pure water*, The Journal of Physical Chemistry Letters **3**, 107 (2012)

[vi] **Douwe Jan Bonthuis**, Stephan Gekle and Roland R. Netz, *Dielectric profile of interfacial water and its effect on double layer capacitance*, Physical Review Letters **107**, 166102 (2011)

[vii] **Douwe Jan Bonthuis**, Klaus F. Rinne, Kerstin Falk, C. Nadir Kaplan, Dominik Horinek, A. Nihat Berker, Lydéric Bocquet and Roland R. Netz, *Theory and simulations of water flow through carbon nanotubes: Prospects and pitfalls*, Journal of Physics: Condensed Matter **23**, 184110 (2011)

[viii] **Douwe Jan Bonthuis**, Kerstin Falk, C. Nadir Kaplan, Dominik Horinek, A. Nihat Berker, Lydéric Bocquet and Roland R. Netz, *Comment on "Pumping of confined water in carbon nanotubes by rotation-translation coupling"*, Physical Review Letters **105**, 209401 (2010)

[ix] **Douwe Jan Bonthuis**, Dominik Horinek, Lydéric Bocquet and Roland R. Netz, *Electrokinetics at aqueous interfaces without mobile charges*, Langmuir **26**, 12614 (2010): *Cover article*

[x] **Douwe Jan Bonthuis**, Dominik Horinek, Lydéric Bocquet and Roland R. Netz, *Electrohydraulic power conversion in planar nanochannels*, Physical Review Letters **103**, 144503 (2009): *With Synopsis in the* APS *magazine "Physics"*

[xi] Dominik Horinek, Andreas Serr, **Douwe Jan Bonthuis**, Mathias Boström, Werner Kunz and Roland R. Netz, *Molecular hydrophobic attraction and ion-specific effects studied by molecular dynamics*, Langmuir **24**, 1271 (2008)

Publications not discussed in the present thesis:

[xii] **Douwe Jan Bonthuis**, Christine Meyer, Derek Stein and Cees Dekker, *Conformation and dynamics of* DNA *confined in slitlike nanofluidic channels*, Physical Review Letters **101**, 108303 (2008)

[xiii] Frank H. J. van der Heyden, **Douwe Jan Bonthuis**, Derek Stein, Christine Meyer and Cees Dekker, *Power generation by pressure-driven transport of ions in nanofluidic channels*, Nano Letters **7**, 1022 (2007)

[xiv] Frank H. J. van der Heyden, **Douwe Jan Bonthuis**, Derek Stein, Christine Meyer and Cees Dekker, *Electrokinetic energy conversion efficiency in nanofluidic channels*, Nano Letters **6**, 2232 (2006)

[xv] **Douwe Jan Bonthuis**, Jingshan Zhang, Breton Hornblower, Jérôme Mathé, Boris I. Shklovskii and Amit Meller, *Self-energy-limited ion transport in sub-nanometer channels*, Physical Review Letters **97**, 128104 (2006)

Bibliography

[1] Ball, P. *Water as an active constituent in cell biology.* Chem. Rev. **108**, 74 (2008).

[2] Stone, H. A., Stroock, A. D., and Ajdari, A. *Engineering flows in small devices: Microfluidics toward a lab-on-a-chip.* Annu. Rev. Fluid Mech. **36**, 381 (2004).

[3] Squires, T. M. and Quake, S. R. *Microfluidics: Fluid physics at the nanoliter scale.* Rev. Mod. Phys. **77**, 977 (2005).

[4] Lyklema, J. *Electrokinetics after Smoluchowski.* Colloids and Surfaces A **222**, 5 (2003).

[5] Catterall, W. A. *Structure and function of voltage-gated ion channels.* Annu. Rev. Biochem **64**, 193 (1995).

[6] Terry, L. J., Shows, E. B., and Wente, S. R. *Crossing the nuclear envelope: Hierarchical regulation of nucleocytoplasmic transport.* Science **318**, 1412 (2007).

[7] Yao, S., Herzog, D. E., Zeng, S., Mikkelsen, J. C., and Santiago, J. G. *Porous glass electroosmotic pumps: design and experiments.* J. Colloid Int. Sci. **268**, 143 (2003).

[8] Yang, J., Lu, F., Kostiuk, L. W., and Kwok, D. Y. *Electrokinetic microchannel battery by means of electrokinetic and microfluidic phenomena.* J. Micromech. Microeng. **13**, 963 (2003).

[9] Daiguji, H., Yang, P., Szeri, A. J., and Majumder, A. *Electrochemomechanical energy conversion in nanofluidic channels.* Nanoletters **4**, 2315 (2004).

[10] Olthuis, W., Schippers, B., Eijkel, J. C. T., and Van den Berg, A. *Energy from streaming current and potential.* Sens. Actuators B **111**, 385 (2005).

[11] Service, R. F. *Desalination freshens up.* Science **313**, 1088 (2006).

[12] Sparreboom, W., Van den Berg, A., and Eijkel, J. C. T. *Principles and applications of nanofluidic transport.* Nature Nanotech. **4**, 713 (2009).

[13] MacKinnon, R. *Potassium channels and the atomic basis of selective ion conduction.* Angew. Chem. Int. Ed. **43**, 4265 (2004).

[14] Agre, P. *Aquaporin water channels.* Angew. Chem. Int. Ed. **43**, 4278 (2004).

[15] Kuyucak, S., Andersen, O. S., and Chung, S.-H. *Models of permeation in ion channels.* Rep. Prog. Phys. **64**, 1427 (2001).

[16] Helmholtz, H. *Studien über elektrische Grenzschichten.* Wied. Ann. **7**, 337 (1879).

[17] Von Smoluchowski, M. *Zur Theorie der electrischen Kataphorese und der Oberflächenleitung.* Phys. Z. **6**, 529 (1905).

[18] Hückel, E. *Die Kataphorese der Kugel.* Physik. Z. **25**, 204 (1924).

[19] Israelachvili, J. and Wennerström, H. *Role of hydration and water structure in biological and colloidal interactions.* Nature **379**, 219 (1996).

[20] Bopp, P. A., Kornyshev, A. A., and Sutmann, G. *Frequency and wave-vector dependent dielectric function of water: Collective modes and relaxation spectra.* J. Chem. Phys. **109**, 1939 (1998).

[21] Faraudo, J. and Bresme, F. *Anomalous dielectric behavior of water in ionic newton black films.* Phys. Rev. Lett. **92**, 236102 (2004).

[22] Stern, O. *Zur Theorie der elektrolytischen Doppelschicht.* Z. Elektrochem. **30**, 508 (1924).

[23] Tielrooij, K. J. *et al. Dielectric relaxation dynamics of water in model membranes probed by terahertz spectroscopy.* Biophysical J. **97**, 2484 (2009).

[24] Kornyshev, A. A., Schmickler, W., and Vorotyntsev, M. A. *Nonlocal electrostatic approach to the problem of a double layer at a metal-electrolyte interface.* Phys. Rev. B **25**, 5244 (1982).

[25] Kornyshev, A. A. and Vorotyntsev, M. A. *Nonlocal dielectric response of the electrode-solvent interface in the double-layer problem.* Can. J. Chem. **59**, 2031 (1981).

[26] Blum, L. and Henderson, D. *Mixtures of hard ions and dipoles against a charged wall - the Ornstein-Zernike equation, some exact results, and the mean spherical approximation.* J. Chem. Phys. **74**, 1902 (1981).

[27] Levin, Y. *Polarizable ions at interfaces.* Phys. Rev. Lett. **102**, 147803 (2009).

[28] Kornyshev, A. A. *On the nonlocal electrostatic theory of hydration force.* J. Electroanal. Chem. **204**, 79 (1986).

[29] Dzubiella, J., Swanson, J. M. J., and McCammon, J. A. *Coupling hydrophobicity, dispersion, and electrostatics in continuum solvent models.* Phys. Rev. Lett. **96**, 087802 (2006).

[30] Kim, Y.-T. *et al. Drastic change of electric double layer capacitance by surface functionalization of carbon nanotubes.* Applied Phys. Lett. **87**, 234106 (2005).

[31] Marčelja, S. *et al. Role of solvent structure in solution theory.* J. Chem. Soc. Faraday Trans. II **73**, 630 (1977).

[32] Abrashkin, A., Andelman, D., and Orland, H. *Dipolar Poisson-Boltzmann equation: Ions and dipoles close to charge interfaces.* Phys. Rev. Lett. **99**, 077801 (2007).

[33] Paillusson, F. and Blossey, R. *Slits, plates, and Poisson-Boltzmann theory in a local formulation of nonlocal electrostatics.* Phys. Rev. E **82**, 052501 (2010).

[34] Stillinger, F. H. and Ben-Naim, A. *Liquid-vapor interface potential for water.* J. Chem. Phys. **47**, 4431 (1967).

[35] Barrat, J. and Bocquet, L. *Large slip effect at a nonwetting fluid-solid interface.* Phys. Rev. Lett. **82**, 4671 (1999).

[36] Joly, L., Ybert, C., Trizac, E., and Bocquet, L. *Hydrodynamics within the electric double layer on slipping surfaces.* Phys. Rev. Lett. **93**, 257805 (2004).

[37] Chandler, D. *Physical chemistry - oil on troubled waters.* Nature **445**, 831 (2007).

[38] Vinogradova, O. I. *Drainage of a thin liquid-film confined between hydrophobic surfaces.* Langmuir **11**, 2213 (1995).

[39] Mamatkulov, S. I., Khabibullaev, P. K., and Netz, R. R. *Water at hydrophobic substrates: Curvature, pressure, and temperature effects.* Langmuir **20**, 4756 (2004).

[40] De Gennes, P.-G. *On fluid/wall slippage.* Langmuir **18**, 3413 (2002).

[41] Huang, D. M. *et al. Water slippage versus contact angle: A quasiuniversal relationship.* Phys. Rev. Lett. **101**, 226101 (2008).

[42] Majumder, M. *et al. Enhanced flow in carbon nanotubes.* Nature **438**, 44 (2005).

[43] Hummer, G., Rasaiah, J. C., and Noworyta, J. P. *Water conduction through the hydrophobic channel of a carbon nanotube.* Nature **414**, 188 (2001).

[44] Hinds, B. *A blueprint for a nanoscale pump.* Nature Nanotech. **2**, 673 (2007).

[45] Beattie, J. K., Djerdjev, A. M., and Warr, G. G. *The surface of neat water is basic.* Faraday Discuss. **141**, 31 (2009).

[46] Schweiss, R. *et al. Dissociation of surface functional groups and preferential adsorption of ions on self-assembled monolayers assessed by streaming potential and streaming current measurements.* Langmuir **17**, 4304 (2001).

[47] Ciunel, K. *et al. Evidence of surface charge at the air/water interface from thin-film studies on polyelectrolyte-coated substrates.* Langmuir **21**, 4790 (2005).

[48] Petersen, P. and Saykally, R. *Is the liquid water surface basic or acidic? Macroscopic vs. molecular-scale investigations.* Chem. Phys. Lett. **458**, 255 (2008).

[49] Buch, V. *et al. Water surface is acidic.* Proc. Nat. Acad. Sci. USA **104**, 7342 (2007).

[50] Vácha, R. *et al. Autoionization at the surface of neat water: Is the top layer pH neutral, basic, or acidic?* Phys. Chem. Chem. Phys. **9**, 4736 (2007).

[51] Knecht, V. *et al. Electrophoretic mobility does not always reflect the charge on an oil droplet.* J. Coll. Int. Sci. **318**, 477 (2008).

[52] Berezhkovskii, A. and Hummer, G. *Single-file transport of water molecules through a carbon nanotube.* Phys. Rev. Lett. **89**, 064503 (2002).

[53] Parsegian, A. *Energy of an ion crossing a low dielectric membrane - solutions to 4 relevant electrostatic problems.* Nature **221**, 844 (1969).

[54] Bonthuis, D. J. *et al. Self-energy-limited ion transport in subnanometer channels.* Phys. Rev. Lett. **97**, 128104 (2006).

[55] Zhang, J., Kamenev, A., and Shklovskii, B. I. *Conductance of ion channels and nanopores with charged walls: A toy model.* Phys. Rev. Lett. **95**, 148101 (2005).

[56] Doyle, D. A. *et al. The structure of the potassium channel: Molecular basis of* K^+ *conduction and selectivity.* Science **280**, 69 (1998).

[57] Kienker, P. K., Degrado, W. F., and Lear, J. D. *A helical-dipole model describes the single-channel current rectification of an uncharged peptide ion-channel.* Proc. Nat. Acad. Sci. USA **91**, 4859 (1994).

[58] Kamenev, A., Zhang, J., Larkin, A. I., and Shklovskii, B. I. *Transport in one-dimensional Coulomb gases: From ion channels to nanopores.* Physica A **359**, 129 (2006).

[59] Li, J. *et al. Electrostatic gating of a nanometer water channel.* Proc. Nat. Acad. Sci. USA **104**, 3687 (2007).

[60] Joseph, S. and Aluru, N. R. *Pumping of confined water in carbon nanotubes by rotation-translation coupling.* Phys. Rev. Lett. **101**, 064502 (2008).

[61] Gong, X. *et al. A charge-driven molecular water pump.* Nature Nanotech. **2**, 709 (2007).

[62] Joseph, S. and Aluru, N. R. *Why are carbon nanotubes fast transporters of water?* Nanolett. **8**, 452 (2008).

[63] Kim, D. and Darve, E. *High-ionic-strength electroosmotic flows in uncharged hydrophobic nanochannels.* J. Coll. Int. Sci. **330**, 194 (2009).

[64] Joseph, S. and Aluru, N. R. *Hierarchical multiscale simulation of electrokinetic transport in silica nanochannels at the point of zero charge.* Langmuir **22**, 9041 (2006).

[65] Lee, C., McCammon, J., and Rossky, P. *The structure of liquid water at an extended hydrophobic surface.* J. Chem. Phys **80**, 4448 (1984).

[66] Huang, D. M. and Chandler, D. *The hydrophobic effect and the influence of solute–solvent attractions.* J. Phys. Chem. B **106**, 2047 (2002).

[67] Huang, D. M., Cottin-Bizonne, C., Ybert, C., and Bocquet, L. *Aqueous electrolytes near hydrophobic surfaces: Dynamic effects of ion specificity and hydrodynamic slip.* Langmuir **24**, 1442 (2008).

[68] Frenkel, D. and Smit, B. *Understanding molecular simulation: From algorithms to applications.* Academic Press, New York, second edition, (2002).

[69] Gabriel, C. *et al. Dielectric parameters relevant to microwave dielectric heating.* Chem. Soc. Rev. **27**, 213 (1998).

[70] Buchner, R., Barthel, J., and Stauber, J. *The dielectric relaxation of water between 0 °C and 35 °C.* Chem. Phys. Lett. **306**, 57 (1999).

[71] Rezus, Y. L. A. and Bakker, H. J. *On the orientational relaxation of* HDO *in liquid water.* J. Chem. Phys. **123**, 114502 (2005).

[72] Berendsen, H. J. C., Grigera, J. R., and Straatsma, T. P. *The missing term in effective pair potentials.* J. Phys. Chem. **91**, 6269 (1987).

[73] Abascal, J. L. F. and Vega, C. *A general purpose model for the condensed phases of water:* TIP4P/2005. J. Chem. Phys. **123**, 234505 (2005).

[74] Sendner, C., Horinek, D., Bocquet, L., and Netz, R. R. *Interfacial water at hydrophobic and hydrophilic surfaces: Slip, viscosity, and diffusion.* Langmuir **25**, 10768 (2009).

[75] Benjamin, I. *Chemical reactions and solvation at liquid interfaces: A microscopic perspective.* Chem. Rev. **96**, 1449 (1996).

[76] Marčelja, S. and Radić, N. *Repulsion of interfaces due to boundary water.* Chem. Phys. Lett. **42**, 129 (1976).

[77] Ball, P. *Chemical physics: How to keep dry in water.* Nature **423**, 25 (2003).

[78] Chandler, D. *Interfaces and the driving force of hydrophobic assembly.* Nature **437**, 640 (2005).

[79] Kornyshev, A. A., Spohr, E., and Vorotyntsev, M. A. *Electrochemical interfaces: At the border line*, In *Encyclopedia of electrochemistry*, chapter 2.1, 33. Wiley, New York (2002).

[80] Lyklema, J. *Fundamentals of interface and colloid science*, volume II. Academic Press, London, (1995).

[81] Hunter, R. J. *Foundations of colloid science.* Oxford University Press, Oxford, second edition, (2001).

[82] Hasted, J. B., Ritson, D. M., and Collie, C. H. *Dielectric properties of aqueous ionic solutions.* J. Chem. Phys. **16**, 1 (1948).

[83] Grahame, D. C. *Effects of dielectric saturation upon the diffuse double layer and the free energy of hydration of ions.* J. Chem. Phys. **18**, 903 (1950).

[84] Heugen, U. *et al. Solute-induced retardation of water dynamics probed directly by terahertz spectroscopy.* Proc. Nat. Acad. Sci. USA **103**, 12301 (2006).

[85] Frenkel, J. *Kinetic theory of liquids.* Dover Publications, New York, (1955).

[86] Shen, Y. R. and Ostroverkhof, V. *Sum-frequency vibrational spectroscopy on water interfaces: Polar orientation of water molecules at interfaces.* Chem. Rev. **106**, 1140 (2006).

[87] Ballenegger, V. and Hansen, J. *Local dielectric permittivity near an interface.* Europhys. Lett. **63**, 381 (2003).

[88] Bonthuis, D. J., Gekle, S., and Netz, R. R. *Dielectric profile of interfacial water and its effect on double-layer capacitance.* Phys. Rev. Lett. **107**, 166102 (2011).

[89] Kharkats, Y. I., Kornyshev, A. A., and Vorotyntsev, M. A. *Electrostatic models in theory of solutions.* J. Chem. Soc. Faraday Trans. II **72**, 361 (1976).

[90] Noyes, R. M. *Thermodynamics of ion hydration as a measure of effective dielectric properties of water.* J. Am. Chem. Soc. **84**, 513 (1962).

[91] Fedorov, M. V. and Kornyshev, A. A. *Unravelling the solvent response to neutral and charged solutes.* Mol. Phys. **105**, 1 (2007).

[92] Leikin, S., Parsegian, V. A., Rau, D. C., and Rand, R. P. *Hydration forces.* Annu. Rev. Phys. Chem. **44**, 369 (1993).

[93] Jackson, J. D. *Classical electrodynamics.* John Wiley & Sons, USA, third edition, (1998).

[94] Russakoff, G. *Derivation of macroscopic Maxwell equations.* Am. J. Physics **38**, 1188 (1970).

[95] Kirkwood, J. G. *The dielectric polarization of polar liquids.* J. Chem. Phys. **7**, 911 (1939).

[96] Fröhlich, H. *Theory of dielectrics.* Clarendon Press, Oxford, (1949).

[97] Ballenegger, V. and Hansen, J. *Dielectric permittivity profiles of confined polar fluids.* J. Chem. Phys. **122**, 114711 (2005).

[98] Lindahl, E., Hess, B., and Van der Spoel, D. GROMACS *3.0: a package for molecular simulation and trajectory analysis.* J. Mol. Mod. **7**, 306 (2001).

[99] Sedlmeier, F., Horinek, D., and Netz, R. R. *Spatial correlations of density and structural fluctuations in liquid water: A comparative simulation study.* J. Am. Chem. Soc. **133**, 1391 (2011).

[100] Reddy, M. R. and Berkowitz, M. *The dielectric constant of* SPC/E *water.* Chem. Phys. Lett. **155**, 173 (1989).

[101] Fedorov, M. V. and Kornyshev, A. A. *Towards understanding the structure and capacitance of electrical double layer in ionic liquids.* Electrochim. Acta. **53**, 6835 (2008).

[102] Bazant, M. Z., Storey, B. D., and Kornyshev, A. A. *Double layer in ionic liquids: Overscreening versus crowding.* Phys. Rev. Lett. **106**, 046102 (2011).

[103] Kolb, J. F., Joshi, R. P., Xiao, S., and Schoenbach, K. H. *Streamers in water and other dielectric liquids.* J. Phys. D: Appl. Phys. **41**, 234007 (2008).

[104] Paluch, M. *Electrical properties of free surface of water and aqueous solutions.* Adv. Colloid Interface Sci. **84**, 27 (2000).

[105] Du, Q., Superfine, R., Freysz, E., and Shen, Y. R. *Vibrational spectroscopy of water at the vapor water interface.* Phys. Rev. Lett. **70**, 2313 (1993).

[106] Du, Q., Freysz, E., and Shen, Y. R. *Vibrational spectra of water molecules at quartz/water interfaces.* Phys. Rev. Lett. **72**, 238 (1994).

[107] Du, Q., Freysz, E., and Shen, Y. R. *Surface vibrational spectroscopic studies of hydrogen bonding and hydrophobicity.* Science **264**, 826 (1994).

[108] Wilson, M. A., Pohorille, A., and Pratt, L. R. *Study on the liquid vapor interface of water. 1: Simulation results of thermodynamic properties and orientational structure.* J. Chem. Phys. **90**, 5211 (1989).

[109] Sokhan, V. P. and Tildesley, D. J. *The free surface of water: molecular orientation, surface potential and nonlinear susceptibility.* Mol. Phys. **92**, 625 (1997).

[110] Lyklema, J. *Fundamentals of interface and colloid science*, volume I. Academic Press, London, (1991).

[111] Andelman, D. *Introduction to electrostatics in soft and biological matter*, In *Soft condensed matter physics in molecular and cell biology*, chapter 6, 97. Taylor & Francis, New York (2006).

[112] Edwards, S. A. and Williams, D. R. M. *Double layers and interparticle forces in colloid science and biology: Analytic results for the effect of ionic dispersion forces.* Phys. Rev. Lett. **92**, 248303 (2004).

[113] Schneck, E. and Netz, R. R. *From simple surface models to lipid membranes: Universal aspects of the hydration interaction from solvent-explicit simulations.* Curr. Opin. Colloid Interface Sci. **16**, 607 (2011).

[114] Faraudo, J. and Bresme, F. *Origin of the short-range, strong repulsive force between ionic surfactant layers.* Phys. Rev. Lett. **94**, 077802 (2005).

[115] Kharkats, Y. I. and Ulstrup, J. *The electrostatic Gibbs energy of finite-size ions near a planar boundary between 2 dielectric media.* J. Electroanal. Chem. **308**, 17 (1991).

[116] Markin, V. S. and Volkov, A. G. *Quantitative theory of surface tension and surface potential of aqueous solutions of electrolytes.* J. Phys. Chem. B **106**, 11810 (2002).

[117] Jayaram, B., Fine, R., Sharp, K., and Honig, B. *Free-energy calculations of ion hydration - an analysis of the Born model in terms of microscopic simulations.* J. Phys. Chem. **93**, 4320 (1989).

[118] Marcus, Y. *Ionic radii in aqueous solutions.* Chem. Rev. **88**, 1475 (1988).

[119] Horinek, D. *et al. Specific ion adsorption at the air/water interface: The role of hydrophobic solvation.* Chem. Phys. Lett. **479**, 173 (2009).

[120] Huang, D. M., Geissler, P. L., and Chandler, D. *Scaling of hydrophobic solvation free energies.* J. Phys. Chem. B **105**, 6704 (2001).

[121] Hummer, G., Garde, S., García, A. E., Paulaiti, M. E., and Pratt, L. R. *Hydrophobic effects on a molecular scale.* J. Phys. Chem. B **102**, 10469 (1998).

[122] Schwierz, N., Horinek, D., and Netz, R. R. *Reversed anionic Hofmeister series: The interplay of surface charge and surface polarity.* Langmuir **26**, 7370 (2010).

[123] Lauga, E., Brenner, M. P., and Stone, H. A. *Microfluidics: The no-slip boundary condition*, In *Handbook of experimental fluid dynamics*, chapter 19, 1219. Springer, New York (2007).

[124] Joly, L. *et al. Liquid friction on charged surfaces: From hydrodynamic slippage to electrokinetics.* J. Chem. Phys. **125**, 204716 (2006).

[125] Wu, P. and Qiao, R. *Physical origins of apparently enhanced viscosity of interfacial fluids in electrokinetic transport.* Phys. Fluids **23**, 072005 (2011).

[126] Vácha, R. *et al. Charge transfer between water molecules as the possible origin of the observed charging at the surface of pure water.* J. Phys. Chem. Lett. **3**, 107 (2012).

[127] De Groot, S. R. and Mazur, P. *Non-equilibrium thermodynamics.* North-Holland Publishing Company, Amsterdam, (1969).

[128] Janeček, J. and Netz, R. R. *Interfacial water at hydrophobic and hydrophilic surfaces: Depletion versus adsorption.* Langmuir **23**, 8417 (2007).

[129] Van der Heyden, F. H. J., Bonthuis, D. J., Stein, D., Meyer, C., and Dekker, C. *Electrokinetic energy conversion efficiency in nanofluidic channels.* Nano Lett. **7**, 1022 (2006).

[130] Van der Heyden, F. H. J., Bonthuis, D. J., Stein, D., Meyer, C., and Dekker, C. *Power generation by pressure-driven transport of ions in nanofluidic channels.* Nanolett. **7**, 1022 (2007).

[131] Ren, Y. and Stein, D. *Slip-enhanced electrokinetic energy conversion in nanofluidic channels.* Nanotechnology **19**, 195707 (2008).

[132] Stein, D., Kruithof, M., and Dekker, C. *Surface-charge-governed ion transport in nanofluidic channels.* Phys. Rev. Lett. **93**, 035901 (2004).

[133] Onsager, L. *Reciprocal relations in irreversible processes I.* Phys. Rev. **37**, 405 (1931).

[134] Onsager, L. *Reciprocal relations in irreversible processes II.* Phys. Rev. **38**, 2265 (1931).

[135] Saxén, U. *Über die Reciprocität der electrischen Endosmose und der Strömungsströme.* Wied. Ann. **47**, 46 (1892).

[136] Stiopkin, I. V. *et al. Hydrogen bonding at the water surface revealed by isotopic dilution spectroscopy.* Nature **474**, 192 (2011).

[137] Willard, A. P. and Chandler, D. *Instantaneous liquid interfaces.* J. Phys. Chem. B **114**, 1954 (2010).

[138] Takahashi, M. *ζ potential of microbubbles in aqueous solutions: Electrical properties of the gas-water interface.* J. Phys. Chem. B **109**, 21858 (2005).

[139] Taylor, R. S., Dang, L. X., and Garrett, B. C. *Molecular dynamics simulations of the liquid/vapor interface of* SPC/E *water.* J. Phys. Chem. **100**, 11720 (1996).

[140] Townsend, R. M. and Rice, S. A. *Molecular dynamics studies of the liquid-vapor interface of water.* J. Chem. Phys **94**, 2207 (1991).

[141] Huang, D. M. *et al. Ion-specific anomalous electrokinetic effects in hydrophobic nanochannels.* Phys. Rev. Lett. **98**, 177801 (2007).

[142] Insepov, Z., Wolf, D., and Hassanein, A. *Nanopumping using carbon nanotubes.* Nanolett. **6**, 1893 (2006).

[143] Longhurst, M. J. and Quirke, N. *Temperature-driven pumping of fluid through single-walled carbon nanotubes.* Nanolett. **7**, 3324 (2007).

[144] Král, P. and Tománek, D. *Laser-driven atomic pump.* Phys. Rev Lett. **82**, 5373 (1999).

[145] Van der Spoel, D. *et al.* GROMACS*: Fast, flexible, and free.* J. Comp. Chem. **26**, 1701 (2005).

[146] Sedlmeier, F. *et al. Water at polar and nonpolar solid walls.* Biointerphases **3**, FC23 (2008).

[147] Condiff, D. W. and Dahler, J. S. *Fluid mechanical aspects of antisymmetric stress.* Physics of Fluids **7**, 842 (1964).

[148] Yang, F. *et al. Couple stress based strain gradient theory for elasticity.* Int. J. Solids Struct. **39**, 2731 (2002).

[149] Hynes, J., Kapral, R., and Weinberg, M. *Particle rotation and translation in a fluid with spin.* Physica A **87**, 427 (1977).

[150] Bertolini, D. and Tani, A. *Stress tensor and viscosity of water: Molecular dynamics and generalized hydrodynamics results.* Phys. Rev. E **52**, 1699 (1995).

[151] Evans, D. J. and Hanley, H. J. M. *Fluctuation expressions for fast thermal transport processes - vortex viscosity.* Phys. Rev. A **25**, 1771 (1982).

[152] Hansen, J. S., Todd, B. D., and Daivis, P. J. *Dynamical properties of a confined diatomic fluid undergoing zero mean oscillatory flow: Effect of molecular rotation.* Phys. Rev. E **77**, 066707 (2008).

[153] Evans, D. J. and Streett, W. B. *Transport properties of homonuclear diatomics II: Dense fluids.* Mol. Phys. **36**, 161 (1978).

[154] Smith, D. E., Babcock, H. P., and Chu, S. *Single-polymer dynamics in steady shear flow.* Science **283**, 1724 (1999).

[155] Gerashchenko, S. and Steinberg, V. *Statistics of tumbling of a single polymer molecule in shear flow.* Phys. Rev. Lett. **96**, 038304 (2006).

[156] Plimpton, S. *Fast parallel algorithms for short-range molecular dynamics.* J. Comput. Phys. **117**, 1 (1995).

[157] Wong-ekkabut, J., Miettinen, M. S., Dias, C., and Karttunen, M. *Static charges cannot drive a continuous flow of water molecules through a carbon nanotube.* Nature Nanotech. **5**, 555 (2010).

[158] Hess, B., Kutzner, C., Van der Spoel, D., and Lindahl, E. GROMACS *4: Algorithms for highly efficient, load-balanced, and scalable molecular simulation.* J. Chem. Theory Comput. **4**, 435 (2008).

[159] Zuo, G., Shen, R., Ma, S., and Guo, W. *Transport properties of single-file water molecules inside a carbon nanotube biomimicking water channel.* ACS Nano **4**, 205 (2010).

[160] Rinne, K. F., Gekle, S., Bonthuis, D. J., and Netz, R. R. *Nanoscale pumping of water by* AC *electric fields.* Nanolett. **12**, 1780 (2012).

[161] Tadros, T. F. and Lyklema, J. *Adsorption of potential-determining ions at the silica-aqueous electrolyte interface and the role of some cations.* J. Electroanal. Chem. **17**, 267 (1968).

[162] Gonzenbach, U. T. *et al. Tailoring the microstructure of particle-stabilized wet foams.* Langmuir **23**, 1025 (2007).

[163] Hansen, J. and Löwen, H. *Effective interactions between electric double layers.* Annu. Rev. Phys. Chem. **51**, 209 (2000).

[164] Quemada, D. and Berli, C. *Energy of interaction in colloids and its implications in rheological modeling.* Adv. Colloid Interface Sci. **98**, 51 (2002).

[165] Tiselius, A. *A new apparatus for electrophoretic analysis of colloidal mixtures.* Trans. Faraday Soc. **33**, 524 (1937).

[166] Varotsos, P. A., Sarlis, N. V., and Skordas, E. S. *Electric fields that "arrive" before the time derivative of the magnetic field prior to major earthquakes.* Phys. Rev. Lett. **91**, 148501 (2003).

[167] Glover, P. W. J. and Jackson, M. D. *Borehole electrokinetics.* The Leading Edge **29**, 724 (2010).

[168] Hidalgo-Álvarez, R. *et al. Electrokinetic properties, colloidal stability and aggregation kinetics of polymer colloids.* Adv. Colloid Interface Sci. **67**, 1 (1996).

[169] Verwey, E. J. W. *The electrical double layer and the stability of lyophobic colloids.* Chem. Rev. **16**, 363 (1935).

[170] Bikerman, J. J. *Ionic theory of electroosmosis, the current flow and the surface conductivity.* Z. Phys. Chem. A **163**, 378 (1933).

[171] Bikerman, J. J. *Die Oberflächenleitfähigkeit und ihre Bedeutung.* Kolloid Zeitschrift **72**, 100 (1935).

[172] Lyklema, J. *Surface conduction.* J. Phys.: Condens. Matter **13**, 5027 (2001).

[173] Van der Heyden, F. H. J., Stein, D., and Dekker, C. *Streaming currents in a single nanofluidic channel.* Phys. Rev. Lett. **95**, 116104 (2005).

[174] Iler, R. K. and Aler, R. K. *The chemistry of silica*. Wiley, New York, (1978).

[175] Lyklema, J. *On the slip process in electrokinetics*. Colloids Surf. A **92**, 41 (1994).

[176] Lyklema, J. and Overbeek, J. T. G. *On the interpretation of electrokinetic potentials*. J. Colloid Sci. **16**, 501 (1961).

[177] Van der Put, A. G. and Bijsterbosch, B. H. *Electrokinetic measurements on concentrated polystyrene dispersions and their theoretical interpretation*. J. Colloid Interface Sci. **92**, 499 (1982).

[178] O'Brien, R. W. and Perrins, W. T. *The electrical conductivity of a porous plug*. J. Colloid Interface Sci. **99**, 20 (1984).

[179] Zukoski, C. F. and Saville, D. A. *The interpretation of electrokinetic measurements using a dynamic model of the Stern layer: I. The dynamic model*. J. Colloid Interface Sci. **114**, 32 (1986).

[180] Zukoski, C. F. and Saville, D. A. *The interpretation of electrokinetic measurements using a dynamic model of the Stern layer: II. Comparisons between theory and experiment*. J. Colloid Interface Sci. **114**, 45 (1986).

[181] Van der Put, A. G. and Bijsterbosch, B. H. *Electrokinetic measurements on concentrated polystyrene dispersions and their theoretical interpretation*. J. Colloid Interface Sci. **92**, 499 (1983).

[182] Dukhin, S. S. *Nonequilibrium electric surface phenomena*. Adv. Colloid Interface Sci. **44**, 1 (1993).

[183] Lyklema, J. and Minor, M. *On surface conduction and its role in electrokinetics*. Colloids Surf. A **140**, 33 (1998).

[184] Hunter, R. J. *The significance of stagnant layer conduction in electrokinetics*. Adv. Colloid Interface Sci. **100**, 153 (2003).

[185] Hunter, R. J. *Foundations of colloid science*. Oxford University Press, Oxford, (2001).

[186] Guo, X., Kirton, G. F., and Dubin, P. L. *Carboxylated ficolls: Preparation, characterization, and electrophoretic behavior of model charged nanospheres*. J. Phys. Chem. B **110**, 20815 (2006).

[187] Bonthuis, D. J. *et al*. *Electrokinetics at aqueous interfaces without mobile charges*. Langmuir **26**, 12614 (2010).

[188] Jouyban, A. and Kenndler, E. *Theoretical and empirical approaches to express the mobility of small ions in capillary electrophoresis*. Electrophoresis **27**, 992 (2006).

[189] Eigen, M. and Wicke, E. *The thermodynamics of electrolytes at higher concentration*. J. Phys. Chem. **58**, 702 (1954).

[190] Kralj-Iglič, V. and Iglič, A. *Influence of finite size of ions on elecrostatic properties of electric double layer*. Electrotechnical Review (Ljubljana, Slovenija) **61**, 127 (1994).

[191] Borukhov, I., Andelman, D., and Orland, H. *Steric effects in electrolytes: A modified Poisson-Boltzmann equation.* Phys. Rev. Lett. **79**, 00319007 (1997).

[192] Borukhov, I., Andelman, D., and Orland, H. *Adsorption of large ions from an electrolyte solution: A modified Poisson-Boltzmann equation.* Electrochim. Acta **46**, 221 (2000).

[193] Churaev, N., Ralston, J., Sergeeva, I., and Sobolev, V. *Electrokinetic properties of methylated quartz capillaries.* Adv. Colloid Interface Sci. **96**, 265 (2002).

[194] Van der Put, A. G. and Bijsterbosch, B. H. *Electrical conductivity of dilute and concentrated aqueous dispersions of monodisperse polystyrene particles. Influence of surface conductance and double-layer polarization.* J. Colloid Interface Sci. **75**, 512 (1980).

[195] Löbbus, M., Sonnfeld, J., Van Leeuwen, H. P., Volgelsberger, W., and Lyklema, J. *An improved method for calculating zeta-potentials from measurements of the electrokinetic sonic amplitude.* J. Colloid Interface Sci. **229**, 174 (2000).

[196] Minor, M., Van der Linde, A. J., and Lyklema, J. *Streaming potentials and conductivities of latex plugs in indifferent electrolytes.* J. Colloid Interface Sci. **203**, 177 (1998).

[197] Kim, Y.-W. and Netz, R. R. *Electro-osmosis at inhomogeneous charged surfaces: Hydrodynamic versus electric friction.* J. Chem. Phys. **124**, 114709 (2006).

[198] Boroudjerdi, H., Kim, Y.-W., Naji, A., Netz, R. R., Schlagberger, X., and Serr, A. *Statics and dynamics of strongly charged soft matter.* Phys. Rep. **416**, 129 (2005).

[199] Kwon, T. *et al. Enhancement mechanism of electrochemical capacitance in nitrogen-/boron-doped carbons with uniform straight nanochannels.* Langmuir **25**, 11961 (2009).

[200] Jiang, J. *et al. Enhanced electrical capacitance of porous carbons by nitrogen enrichment and control of the pore structure.* Microporous Mesoporous Mater. **118**, 28 (2009).

[201] Wang, H., Gao, Q., and Hu, J. *Preparation of porous doped carbons and the high performance in electrochemical capacitors.* Microporous Mesoporous Mater. **131**, 89 (2010).

[202] Artemenko, S. E., Glukhova, L. G., and Zagoruiko, N. I. *Effect of oxidative treatment of carbon fibre on the properties of a carbon-fibre-filled plastic fabricated by polycondensation filling.* Fibre Chemistry **33**, 502 (2001).

[203] Okajima, K., Ohta, K., and Sudoh, M. *Capacitance behavior of activated carbon fibers with oxygen-plasma treatment.* Electrochim. Acta **50**, 2227 (2005).

[204] Frackowiak, E. *et al. Optimisation of supercapacitors using carbons with controlled nanotexture and nitrogen content.* Electrochim. Acta **51**, 2209 (2006).

[205] Sidorenko, A. *et al. Switching of polymer brushes.* Langmuir **15**, 8349 (1999).

[206] Harnish, B. *et al.* UV-*cross-linked poly(vinylpyridine) thin films as reversibly responsive surfaces.* Chem. Mater. **17**, 4092 (2005).

[207] Goeting, C. H. *et al. Sonoelectrochemistry at tungsten-supported boron-doped* CVD *diamond electrodes.* Diamond Relat. Mater. **8**, 824 (1999).

[208] Swain, G. M. and Ramesham, R. *The electrochemical activity of boron-doped polycrystalline diamond thin-film electrodes.* Anal. Chem. **65**, 345 (1993).

[209] Kocrick, E. *et al. Ordered mesoporous carbide derived carbons for high pressure gas storage.* Carbon **48**, 1707 (2010).

[210] Fernández, J. A. *et al.* EDLC *performance of carbide-derived carbons in aprotic and acidic electrolytes.* Electrochim. Acta **53**, 7111 (2008).

[211] Wang, S. *et al. Wettability and surface free energy of graphene films.* Langmuir **25**, 11078 (2009).

[212] Li, H.-Q. *et al. A competitive candidate material for aqueous supercapacitors: High surface-area graphite.* J. Power Sources **185**, 1557 (2008).

[213] Du, X. *et al. Graphene nanosheets as electrode material for electric double-layer capacitors.* Electrochim. Acta **55**, 4812 (2010).

[214] Pandolfo, A. G. and Hollenkamp, A. F. *Carbon properties and their role in supercapacitors.* J. Power Sources **157**, 11 (2006).

[215] Chen, W.-C. and Wen, T.-C. *Electrochemical and capacitive properties of polyaniline-implanted porous carbon electrode for supercapacitors.* J. Power Sources **117**, 273 (2003).

[216] Karandikar, P. *et al. Synthesis and characterization of mesoporous carbon through inexpensive mesoporous silica as template.* Microporous Mesoporous Mater. **98**, 189 (2007).

[217] Sevilla, M. *et al. Performance of templated mesoporous carbons in supercapacitors.* Electrochim. Acta **52**, 3207 (2007).

[218] Fuertes, A. B., Pica, F., and Rojo, J. M. *Influence of pore structure on electric double-layer capacitance of template mesoporous carbons.* J. Power Sources **133**, 329 (2004).

[219] Fuertes, A. B. *et al. Templated mesoporous carbons for supercapacitor application.* Electrochim. Acta **50**, 2799 (2005).

[220] Cao, Y. *et al. Synthesis, characterization, and electrochemical properties of ordered mesoporous carbons containing nickel oxide nanoparticles using sucrose and nickel acetate in a silica template.* J. Solid State Chem. **180**, 792 (2007).

[221] Kalpana, D. *et al. Recycled waste paper - a new source of raw material for electric double-layer capacitors.* J. Power Sources **190**, 587 (2009).

[222] Zhou, H. *et al. Electrochemical capacitance of self-ordered mesoporous carbon.* J. Power Sources **122**, 219 (2003).

[223] Xu, B. *et al. High-capacitance carbon electrode prepared by* PVDC *carbonization for aqueous* EDLC*s.* Electrochim. Acta **54**, 2185 (2009).

[224] Ramesham, R. and Rose, M. F. *Electrochemical characterization of doped and undoped* CVD *diamond deposited by microwave plasma.* Diamond Relat. Mater. **6**, 17 (1997).

[225] Roldán, S. *et al. Comparison between electrochemical capacitors based on* NaOH- *and* KOH-*activated carbons.* Energy Fuels **24**, 3422 (2010).

[226] Seredych, M. *et al. Surface functional groups of carbons and the effects of their chemical character, density and accessibility to ions on electrochemical performance.* Carbon **46**, 1475 (2008).

Acknowledgments

First and foremost I would like to thank my advisor Roland R. Netz for giving me the opportunity to work with him and for his dedicated supervision. Thank you for our efficient and productive teamwork; I have learned a lot and it has been a great pleasure to work with you. Furthermore I would like to thank my collaborators, in particular Dominik Horinek, Lydéric Bocquet, Stephan Gekle and Klaus Rinne for their help and advice. For the fruitful discussions and work on our joint projects I would like to express my gratitude to Nihat Berker, Nadir Kaplan, Kerstin Falk and Pavel Jungwirth. Many thanks also to my friends and colleagues from the soft matter group: Christian Sendner, Sebastian Fischer, Andreas Serr, Manu Schneck, Felix Sedlmeier, Matej Kanduç, Maria Fyta, Joe Dzubiella, Yann von Hansen, Julius Schulz, David Hofmann, Alex Herz, Shavkat Mamatkulov, Vladimir Lobaskin, Hirofumi Wada and Michael Hinczewski. In particular, I would like to thank my friends Aykut Erbaş, Immanuel Kalcher, Tom Einert and Ioannis Daotidis for our many no-so-work-related projects. Ich bedanke mich ganz herzlich bei Sonja Ortner, insbesondere für die Organisation der Winterschulen und für die Hilfe beim Ausfüllen von Formularen.

I acknowledge the Deutsche Forschungsgemeinschaft for funding via the Nanosystems Initiative Munich and the Leibniz Rechenzentrum for providing the necessary computational resources.

I would like to thank all my friends from abroad for visiting München every now and then. Finally, I thank my family, and especially Angelique, for their continuous help and support.